2021

Characterization of Hydrogenated Boron Carbide and Boron Carbon Nitride Thin Films and Applications

Shraddha Dhanraj Nehate
University of Central Florida

CHARACTERIZATION OF HYDROGENATED BORON CARBIDE AND BORON CARBON NITRIDE THIN FILMS AND APPLICATIONS

by

SHRADDHA DHANRAJ NEHATE
B.E.E.E., Mumbai University, 2013
M.S.E.E., University of Central Florida, 2016

A dissertation submitted in partial fulfillment of the requirements
for the degree of Doctor of Philosophy
in the Department of Electrical and Computer Engineering
in the College of Engineering and Computer Science
at the University of Central Florida
Orlando, Florida

Summer Term
2021

Major Professor: Kalpathy B. Sundaram

ABSTRACT

Dimension scaling has been the driving force for improved performance of semiconductor integrated circuits (ICs) for the past few decades. While the semiconductor industry continues to achieve returns on Moore's law, the resistance-capacitance (RC) delay remains a critical bottleneck towards further performance improvement. To support advanced computing performance, the development and integration of new low dielectric (low-k) materials to reduce the capacitance of interconnects are crucial. Apart from the low dielectric constant value, one of the other vital parameters to replace the current dielectric material is mechanical stability. Materials in the boron, carbon, and nitrogen ternary triangle have emerged promising low dielectric materials. The combination of boron, carbon, and nitrogen leads to unique materials exhibiting distinct properties from graphite to boron carbide (B_4C), boron nitride (BN), boron carbon nitride (BCN) compounds going from metallic to semiconducting to insulating. BCN compounds combine properties of diamond to display excellent mechanical properties and reproduce BN semiconducting properties with adjustable bandgaps. The dielectric constant (k) value of B_4C and BCN is between 4-6. This dissertation attempted to reduce the k value of B_4C and BCN by introducing non-polar bonds in the materials through hydrogenation using the RF magnetron sputtering technique. Thin films were deposited by single or dual-target sputtering from B_4C and BN targets by varying hydrogen to nitrogen reactive gas and substrate temperature. All the films demonstrated distinct composition at different growth parameters and displayed evidence of tunable properties with film composition. It was shown that tuning film composition

achieves low-k values while ensuring no deterioration in the mechanical properties of thin films. Moreover, the influence of hydrogenation and variation in substrate temperature was investigated on B_4C and BCN properties for applications in electrical, mechanical, and optical devices. Additionally, graphene analogous BCN nanocoating synthesized in this study exhibited outstanding inhibition against bacterial growth and biofilm formation, making them promising for biomedical devices.

I dedicate my PhD dissertation to my grandparents Sundarlal Chaudhari and Sindhu Chaudhari.

Their hard work, humble life and spiritual outlook is a constant inspiration to me.

ACKNOWLEDGMENTS

This journey towards the Ph.D. degree has taken multiple turns with emerging ideas on certain days and unexpected results on some, accompanied by a lot of failures. What did not change is the unconditional and unwavering support, guidance, and inspiration from many people. I want to take this opportunity to thank these people without whom I would never have come this far professionally and personally.

I would like to express my deepest gratitude to my advisor Prof. Kalpathy B. Sundaram. This dissertation would not have been possible without his guidance and encouragement. I sincerely appreciate the freedom and flexibility that Prof. Sundaram provided, allowing me to make mistakes and learning along the way, pointing me in the right directions, teaching me to make better data-driven decisions, and moulding me into a good researcher. Apart from being a good researcher, I am forever grateful to him for instilling great values.

I want to thank my committee members Prof. Reza Abdolvand, Prof. Jiann Yuan, Prof. Vikram Kapoor, and Prof. Jayan Thomas for their support through all these years. They have all helped me on multiple occasions with access to measurement equipment, technical discussions, feedback on research and presentations, as well as joyful conversations.

Special thanks to the staff at AMF and MCF. I am grateful to Edward Dein for lessons in the cleanroom. Ed has always been helpful with a smile on his face and assured me when the sputtering system was down. I would like to acknowledge the help from Avra Kundu and Giji Skaria on cleanroom-related activities. I would like to thank Kirk Scammon for training me on XPS,

REELS, SEM, and EDS. I would also like to acknowledge our collaborators Prof Andres Campiglia and Prof Robert Peale from UCF, and Prof Alex Volinsky from the University of South Florida. Prof Peale was very kind and patient while I learned the FTIR technique for the first time in his lab. I am thankful for his guidance in teaching me the technique and mentoring me with the analysis.

To my fellow lab mates, Ashwin Kumar Saikumar and Sreeram Sundaresh, nothing would be accomplished without their help and suggestions. I will always remember the fast-paced projects we worked on, the tight deadlines we met while keeping the lab environment fun and friendly. None of the projects would have been half as fun or productive without you. I will keep fond memories of working with you both, specifically the late evenings and weekends in the HEC lab and cleanroom.

Through my MS and Ph.D. journey at the UCF, I am incredibly grateful to have worked with Diana Poulalion. Working together on the department duties for the past six years brought us very close. I cherish my friendship with her. I want to thank Diana for being a wonderful friend and showing me support when I needed it.

A heartfelt thank you to my dearest friend Namita for being one of my pillars of strength. Our friendship has eased some of the toughest times I had in graduate school, and it will last forever. Thank you to kindest Shamika who has supported me tremendously. To my friends in the Orlando, Vibhav, Divyashree, Pankaj, Sameer, Ritesh and Nikunj, your presence, support, and energy kept me encouraged through this journey. Knowing and spending time with you made things so much easier. I want to thank Swati O., Swati D., Rimpi and Niladri for being my constant

source of encouragement and celebrating my small wins even thousands of miles away. I am grateful to Yogesh Patil, Disha Patil, Dhiraj Bhangale and Madhuri Bhangale for being my family away from home in Orlando.

I want to express my deepest gratitude to my beloved husband, Tushar Deshpande, for his support and companionship. Your unfaltering love and patience granted me strength and hope during the most challenging times of the Ph.D. We managed a long-distance relationship with grace. Thank you for bringing out the best in me, this Ph.D. is as much yours as it is mine.

I would like to thank my parents Dhanraj Nehate and Bharati Nehate, who were instrumental in shaping me to become the person I am today. Their endless sacrifices allowed me to pursue my dreams. Thank you to my brother Chinmay Nehate for inspiring me to do better every day and trusting in my abiities. I am also blessed to have amazing and affectionate in-laws, Ramesh Deshpande and Manjula Deshpande for supporting my goals and dreams. A special thanks to Tanvi Katti and Hrishi Katti for their encouragement, and to little ray of sunshine Ayan Katti.

Finally, thank you to the Lord for everything.

TABLE OF CONTENTS

LIST OF FIGURES

LIST OF TABLES

CHAPTER ONE: INTRODUCTION

Advances in the semiconductor technology due to dimensional scaling over the past few decades has manifested packing more transistors onto a single chip. Dimension scaling has been the most significant characteristic of the development and evolution of the solid-state electronics industry following The International Technology Roadmap for Semiconductors [1]. The continuous miniaturization to abide by Moore's law is stimulated by the improved performance due to increased speed and more functions per unit area. The solid-state electronics thus evolved through the microelectronics stage has reached the nanoelectronics technology node. The semiconductor industry crossed the 10 nm silicon logic threshold in 2018, and accomplished 2 nm technology node in 2021, which can pack over 50 billion transistors onto a chip the size of a fingernail.

Materials have played a crucial role in this evolution of the semiconductor industry. Device performance and reliability depend greatly on the materials chosen and the compatibility of the materials with the fabrication processes employed. The transistor device consists of metallic segments connected horizontally and vertically, serving as gate contacts, diffusion barrier layer and dielectric layers. State-of-the-art devices consists of multiple layers of metallization, as shown in figure 1.1 [2].

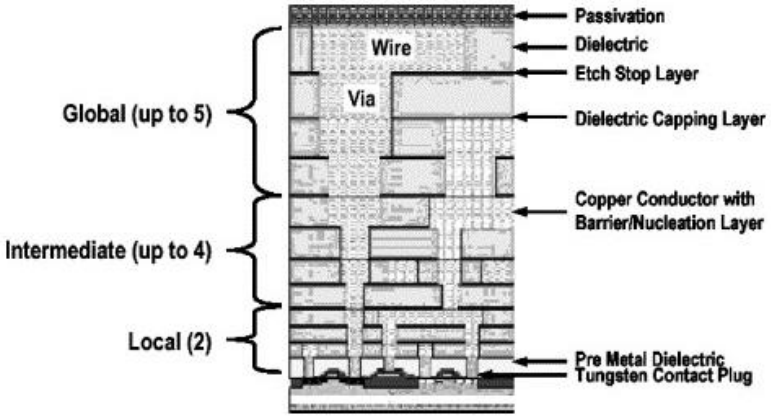

Figure 1.1: Cross-section of multi-layer integrated circuit.

Interlayer Dielectrics (ILD) can be divided into three categories based on their functions namely the active dielectric layer, the layers required for device processing, and the insulating layers. The active dielectric layer fundamentally plays an important role in device operation specific for the storage of charges. These are gate oxide and capacitor dielectric in memory devices. The layers required for device processing consists of etch stop layers such as silicon nitride needed during etching and chemical mechanical polishing processes, anti-reflective coatings for lithography, diffusion layers to enable selective area diffusion or ion implantation. ILD administers isolation between the metal lines for single or multi-layer metal interconnects.

To continue the development of the IC industry, it is essential to introduce new materials to accommodate further miniaturization. As dimensions shrink, the switching speed of transistors increases since the carrier transit time across the channel length decreases. The effective device speed is controlled by the intrinsic gate delay as well as the time of signal propagation through the metal interconnects. Any interconnection can be represented as a chain of resistors and

capacitors, as shown in figure 1.2 [3]. A signal propagating through this interconnection experiences a resistance-capacitance (RC) delay. The continuous scaling of feature size of integrated circuits to achieve continued returns on Moore's law is hindered by the interconnection delay. RC time delay remains a critical bottleneck to improve the computing performance.

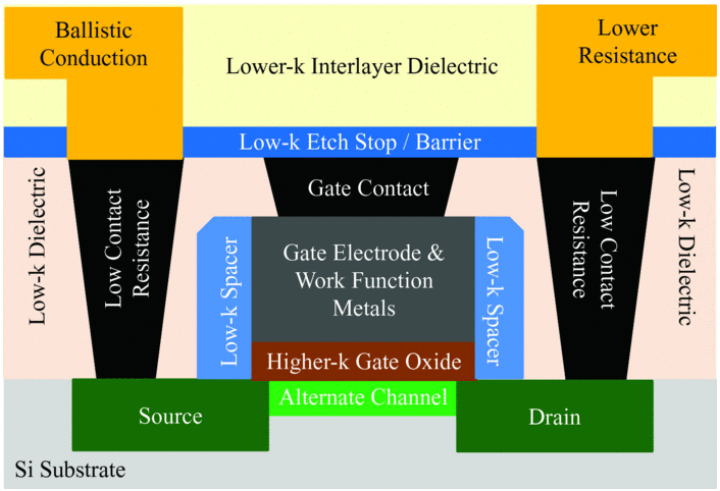

Figure 1.2: Schematic of Cu metal lines in the dielectric layer.

To understand RC delay, figure 1.3 shows a schematic model of interconnects circuit [4]. Referring to figure 1.3, P represents the line pitch, W is the line width, S is the line spacing, and T represents the line thickness. The RC delay [4, 5] is given by:

$$RC = 2\ \rho\ \kappa\ \epsilon 0\ [(4L^2/P^2) + (L^2/T^2)] \quad (1)$$

Where ρ is the metal resistivity, κ is the relative dielectric constant of the ILD, $\epsilon 0$ is the vacuum permittivity, and L is the line length. Dimensional scaling with a decrease in feature size provokes

a sharp increase in RC time delay. The RC time delay governs the overall on-chip cycle time for devices smaller than 0.25 μm [6].

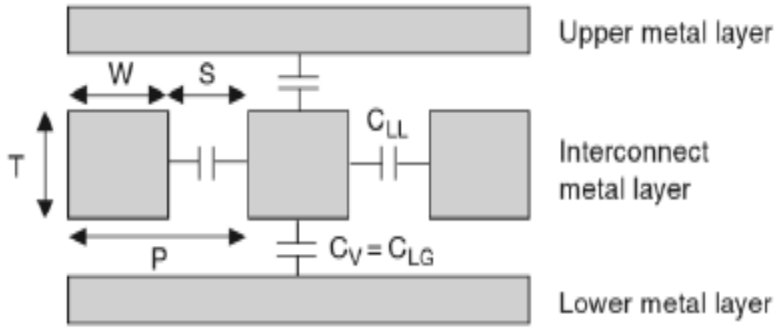

Figure 1.3: Schematic of a typical interconnect circuit. LG refers to line-to-ground, and LL refers to line-to-line contributions.

The propagation velocity of electromagnetic waves becomes critical due to unyielding constraints on the interconnect delay. To support a further increase in transistor density and improve the performance, either conductor resistance or dielectric capacitance must decrease. The introduction of Cu has improved the situation significantly compared to the conventional Al/SiO_2 technology by reducing the resistivity between the interconnects. However, the impact of delay is persistently more than ever as we enter the nanometer regime. As Cu has become the established choice of conductor material, the primary focus and challenge remain on exploring new low dielectric (low-k) materials to replace the traditional SiO_2 (k=4) to achieve lower signal delay. Reducing the dielectric capacitance is also significant for reducing power consumption. Ever-increasing frequencies and higher transistor densities on chips lead to a dramatic increase

in power consumption. The relation between power and the capacitance of dielectric material is given by [7]

$$P = \alpha C V^2 f, \quad (2)$$

Where P is the power consumption, α is the wire activity, C is the total on capacitance, V is the supply voltage, and f is the operational frequency. The total capacitance C can be expressed as:

$$C = C_{output} + C_{wire} + C_{input} \quad (3)$$

C_{output} and C_{input} are the output and input capacitance of the transistor itself, and C_{wire} is the capacitance introduced every time the wire is active. Thus, the dielectric constant of the material significantly influences the power dissipation. Reducing the k value by reducing C will curtail the power dissipation and make circuits faster.

1.1 Dielectric Properties

A dielectric material is an insulator that can be polarized on the application of an external electric field. ILD properties can be categorized into four domains: electrical, mechanical, chemical, and thermal. Table 1.1 lists the requirements for low dielectric constant ILD material [4]. The synthesizing technique may alter the properties of ILD material, and thus determining the required properties to ensure the reliability of ILD is of utmost importance.

Table 1.1: Requirements for ILD materials

Electrical	Mechanical	Chemical	Thermal
Low dissipation	Film thickness	High chemical resistance	High thermal stability
Low leakage	Adhesion	High etch selectivity	Low thermal expansion
High reliability	Low stress	Low moisture absorption	Low thermal shrinkage
Low charge trapping	High tensile modulus	Low solubility of H_2O	High thermal conductivity
High electric field strength	High hardness	Low gas permeability	
	Low shrinkage	High purity	
	Low weight loss	No metal corrosion	
	High fracture toughness	High storage life	
		Environmentally safe and health compatible	

The electrical stability of the dielectric materials is one of the most critical parameters irrespective if the dielectric is used as an ILD or as a passivation layer for device processing. Ideally, a good ILD material must display high electrical bulk and surface resistivity, low leakage current, and thus very high dielectric breakdown strength, low charge trapping, low dielectric constant, low dissipation, and high reliability.

Resistivity: The amount of voltage-induced current through the dielectric material is determined by the resistivity values. Dielectric layers in the integrated circuits are subjected to high electrical fields (~10^7 volt/cm) [4]. Thus materials with very high resistivity (> 10^{14} ohm-cm at RT) are preferred for the dielectric layer.

Current Leakage and Dielectric Strength: Ideally, dielectric materials are perfect insulators with very high resistivity. However, all dielectrics allow the passage of some current under the influence of applied voltage. Poole-Frenkel emission [8] and Fowler-Nordheim tunneling [9] are responsible for the passage of electric current through impurity-free dielectric materials. The maximum voltage a dielectric material can sustain without causing runaway currents is the leakage current capability. At high runaway currents, the dielectric breaks down and discharges. This maximum field is known as the dielectric strength and is represented as volt/cm. Dielectric strength depends on the thin film thickness and shows a reducing trend with thickness. The dielectric field strength reduces with higher thickness due to defects, low thermal conductivity of dielectrics, and the Joule heating, which raises the temperature more in thicker films than thinner films.

Mechanical properties also play a critical role in deciding the reliability of semiconductor materials and devices. Mechanical failures such as cracks, lack of adhesion, stress-related defects, and fractures during chemical-mechanical planarization are some of the factors that affect dielectric materials performance. Many of the properties are highly dependent on the process parameters of dielectric thin films.

Stress: The stress can be compressive or tensile if the material under stress will expand or contract respectively, under the impact of force causing the stress. General convention states that compressive stresses are negative and tensile stresses are positive. High tensile stress leads to cracks in the films, and compressive stress leads to curling. The intrinsic stress can be due to

multiple reasons such as lattice mismatch between the substrate and film, the film microstructure, defects in the film, volume changes associated with chemical or metallurgical interactions, anisotropic growth, and surface tension [4]. Thus, it is crucial that the dielectric thin films exhibit lower stress leading to more reliable connections.

Adhesion: In the IC, the adhesion of the film to the substrate is of utmost importance and should not be affected during the several IC fabrication steps. Fundamentally, the interatomic interactive forces across the film-substrate interface determine the adhesion. Atoms and molecules with large polarizabilities have higher adhesion strength. Interfacial bonding forces and adhesion are affected due to the presence of impurities, surface roughness, reactive environment, overlying coatings, and temperature. To ensure good adhesion between the film and substrate, there must be (i) strong interatomic bonding across the film-substrate interface, (ii) absence of fracture modes and reactive environment that can produce stress, (iii) a low level of film stress, and (iv) absence of long-term degradation modes [10].

Some of the other properties which affect the mechanical stability of ILD films are thin film thickness uniformity, high tensile modulus and hardness, high crack resistance, and low shrinkage. Since most ILD applications require chemical mechanical polishing (CMP) of ILD films, higher tensile modulus, and higher hardness are fundamental requirements for ILD films. Unoptimized deposition conditions introduce many undesirable behaviors in ILD. A non-uniform thickness creates non-uniform stress characteristics and causes difficulties in further processing of the film. Excessive shrinkage, which occurs with many organics dielectrics, leads to cracks in

the films. Pores and cracks create pathways for metal diffusions leading to leakage and eventually short between two levels of metal interconnects. Thus heightened attention must be paid to engineer dielectric for ILD applications.

1.2 How To Reduce The k-value

To sustain and enhance device performance through miniaturization of device size, it is essential to find new materials with dielectric constants lower than 4 or lower the dielectric value of known materials. A low-k material typically is an insulating material that exhibits weak polarization when subjected to an externally applied electric field. Dielectric constant (k), also known as relative permittivity is the ratio of permittivity of a substance to that of free space. Polarization induces dipoles in the dielectric material, and all dipoles become aligned with the applied field. Figure 1.4 shows a schematic illustration of a capacitor [11]. Thus, the charge distribution induced by the external field results from cumulative contributions from electronic, ionic, orientation, and space charge polarization. The electronic and ionic polarizations are attributed to applied field-induced displacement of electrons with respect to nucleus and negative and positive ions in ionic dielectric. On the other hand, the orientation and space charge polarization are associated with the field-induced alignment of existing dipoles in the material with existing mobile charges at defect sites. The relation between dielectric constant value and polarizability is given as follows [4]:

$$k = \frac{3}{1-(4\pi N \alpha /3)} - 2 \quad (4)$$

Where k is the dielectric constant value, N is the number of molecules per unit value, and α is the total polarizability of dielectric materials.

It can be observed that the higher the N and α, the higher is the k value. The larger molar volume would result in lower N and thus lower k. Therefore, to develop materials with lower k, materials with larger molar volumes (N) and lower polarizability (α) becomes necessary. ILD designed with smaller atoms (such as C, B, H) have comparatively lower α and lower k values. Lowering the dielectric constant can be achieved by reducing the electron density of conventional dielectric materials. One of the most obvious choices is choosing materials with chemical bonds of lower polarizability than Si-O, choosing a structure with lower mass density than SiO_2, or adding porosity to the film [12]. Unfortunately, most methods that lower the electron density also show a dramatic decline in the mechanical properties. The IC industry has already replaced Si-O bonds with materials that exhibit lower polarizable bonds such as Si-F or Si-C [13]. A more fundamental reduction can be achieved by using virtually all nonpolar bonds such as C-C or C-H.

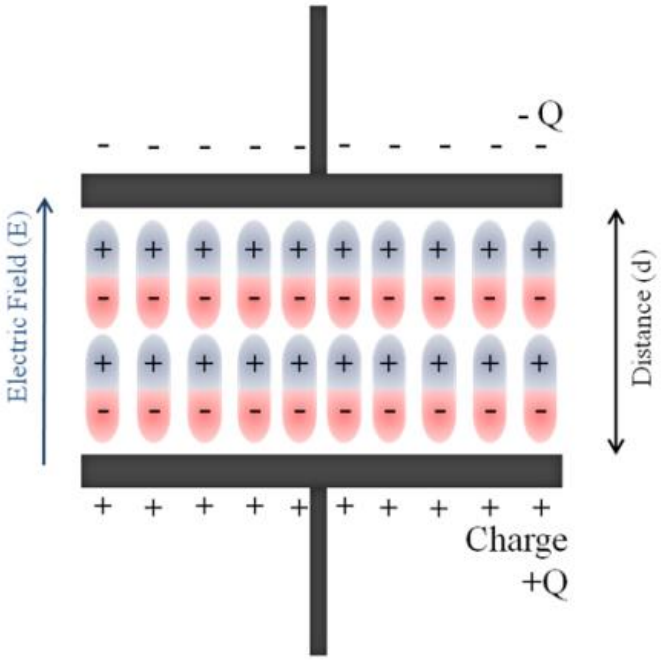

Figure 1.4: Schematic illustration of a capacitor with electrical dipoles.

Minimizing the moisture content in the dielectric material to minimize the highly polar O-H bonds (k=80) is yet another approach for reducing k values in dielectric materials. Ideal low-k dielectric materials must be hydrophobic to prevent deterioration of their k value.

1.3 Motivation

The search and implementation of new materials have been ongoing for use as the intermetal dielectric (IMD) or ILD. The first such IMD/ILD material implemented was silicon oxyfluoride (SiOF) with a k value between 3.6 to 3.8 [14]. This was followed by the replacement of aluminum (Al) with copper (Cu) metal as Cu interconnects showed a 40-45% drop in the resistance compared to Al wiring [15]. Replacement of metal interconnect with Cu also led to the

development of damascene processing modifying the subtractive metal approach with subtractive dielectric approach [16]. Around this time, inorganic-organic carbon-doped oxide (a-SiOC:H) materials with low dielectric constant values (k= 3.1 - 3.3) were also scrutinized to replace SiOF [17]. Since then, several types of materials such as SiC:H (k = 4.0-7.0), SiN:H, SiCN:H (k = 4.5-5.8) have been investigated to be used as ILD material. Various polymers such as poly methyl methacrylate (PMMA), polyhedral oligomeric silsesquioxane (POSS) and poly dimethyl-siloxane (PDMS) were also investigated for low-k materials. However, these materials exhibit challenges in maintaining the chemical, thermal, electrical, mechanical stability with low-k value [18]. The inevitable falloff in the mechanical properties with decreasing k value labeled as the low-k death curve is one of the primary obstacles in improving low-k ILD materials.

As discussed in the above sections, for successful integration of low-k dielectric materials in the IC manufacturing processes, it must abide by the following requirements: a) exhibit appropriate electrical characteristics along with good thermal and mechanical properties; b) be able to perform with other interconnect materials; c) be compatible with manufacturing processes in place; d) be available in high purity form and economical, and e) have high reliability over the product lifetime under specific device operation conditions. A candidate material that exhibits most of these requirements and has attracted much attention is boron carbon nitride (BCN). BCN materials belong to the family of diamond, boron carbide (B_4C), boron nitride (BN), and hypothetical carbon nitride (β-C_3N_4). Initially, BCN compounds gathered interest due to their dielectric properties, which was the primary pursuit of the semiconductor industry to reduce the time delay and increase the computing performance of ICs through dimension scaling.

BCN materials have been able to demonstrate low dielectric constant values. Additionally, since BCN materials belong to the diamond family, they exhibit excellent mechanical properties and maintain stringent requirements of the back end of line processing, unlike other polymers investigated in the past. BCN compounds are known to combine the excellent properties of B_4C, BN, and C_3N_4, with their properties adjustable depending on the composition and structure [19]. As graphite is semi-metallic and h-BN is insulating, hybrid BCN between graphite and h-BN exhibits semiconducting properties.

Since hydrogen is the lowest atomic number element (Z=1), hydrogenation of dielectric materials to obtain low dielectric constant values through the formation of non-polar bonds has gained much interest. Materials such as a-Si:H, a-C:H, a-SiC:H, and SiCN:H have reported lower dielectric values after hydrogenation [18, 20]. Although BCN is a potential low-k dielectric material, focused research on the influence of hydrogenation has not been evaluated. It is essential to analyze the impact of hydrogenation and other deposition parameters on B_4C and BCN electrical properties such as dielectric constant and resistivity. While it is essential to obtain low-k values with hydrogenation, it is also extremely crucial that the films mechanical properties do not deteriorate. As BCN is a wide bandgap material, there is an imminent requirement to evaluate the influence of hydrogenation on optical properties. This can further open new opportunities in optoelectronic applications in extreme conditions.

1.4 Objective and Outline

The primary focus of this dissertation is aimed at investigating the influence of hydrogenation on B_4C and BCN thin films using the reactive RF magnetron sputtering technique. The influence of hydrogenation and other deposition parameters on electrical, optical, mechanical, and photoluminescence properties were assessed. These assessments help determine the feasibility of BCN materials as potential candidates for low-k in the CMOS technology. As low-k dielectric materials also need to satisfy the stringent requirements for mechanical properties, investigations on mechanical properties of BCN thin films were also examined. With the latest developments of BCN nanomaterials showcasing desirable and controllable properties in the nano-biotechnology and nanomedicine field, the efficacy of BCN nano-coatings on bacterial inhibition was evaluated. This thesis is organized as follows. In chapter 1, a brief introduction of the impact of dimensional scaling in the CMOS devices is discussed. The essential equations describing the relationship between dimension scaling and challenges in improving the computing performance in the IC industry is discussed. It also discusses the opportunities and challenges for low-k materials.

Chapter 2 provides the readers with a comprehensive background on the compounds in the B-C-N ternary triangle. This chapter attempts to contemplate the BCN materials with the greatest attention to detail on synthesis techniques, properties, and corresponding applications. It also provides a comparison of BCN thin films with other prominently studied low dielectric materials. After graphene, graphene analogous BCN nanomaterials are researched intensively due to their unique chemical and physical properties. This chapter highlights BCN nanomaterials, their

synthesis techniques in different dimensions, along with properties and corresponding applications.

Chapter 3 includes the experimental process, equipment, and techniques used to study BCN thin films and nano-coatings. The deposition techniques and process parameters used to synthesize thin films and nanocoatings of boron carbide and boron carbon nitride are explained. This section focuses on techniques used for surface characterization, electrical and optical properties. Detailed discussions about the methods and techniques used to investigate the mechanical properties of BCN thin films are presented. The equipment, settings, data collection and analysis for photoluminescence studies on hydrogenated BCN thin films are covered in detail. Methods used to evaluate the efficacy of BCN nano-coating on bacterial inhibition properties are explained.

Chapter 4 covers the results and discussion. This chapter focuses on the results obtained by depositing BC, BCN thin films with different process parameters using RF magnetron sputtering. The influence of process parameters on electrical, optical, and mechanical properties are displayed and discussed. This chapter also covers the distinct and tunable photoluminescence properties observed and potential applications. Further, the chapter also discusses the unique properties of BCN nanocoatings to inhibit bacterial growth and biofilm formation on central venous catheters.

Chapter 5 provides details on the conclusion of the studies performed and paves a path for further exploration.

CHAPTER TWO: LITERATURE REVIEW

Research in carbon-based materials has aroused great interest for many decades for the latest technological advancements. New forms of carbon are also investigated extensively to address environmental concerns. When carbon is combined with other materials, it enhances the structural diversity, which promotes these materials to exhibit an extensive range of properties and applications. Combining carbon with boron and nitrogen results in interesting phases due to covalent bonding between the elements. The compounds in the boron-carbon-nitrogen ternary triangle such as diamond (C), cubic boron nitride (c-BN), boron carbide (B_4C), and hypothetical carbon nitride (β-C_3N_4) are popular due to their covalent bonding, short bond lengths, and low atomic mass which allows the materials to have low dielectric constant along with excellent thermal and mechanical strength [21-25]. Diamond is the hardest material known, c-BN is next to diamond in hardness, and B_4C is the third hardest material [26].

2.1 Boron Carbon Nitride (BCN)

Boron carbon nitride (BCN) compounds are known to combine the unique properties of B_4C and BN, and their properties can be tuned depending on composition and structure. As graphite is semi-metallic and h-BN is insulating, hybrid BCN situated between graphite and h-BN exhibits excellent semiconducting properties [27, 28]. B-C-N based system commonly exhibits the following bonding structures: (i) cubic diamond or c-BN with sp^3 based tetrahedral coordination, (ii) hexagonal graphite or h-BN with sp^2 based tetrahedral trigonal atom coordination, and (iii)

rhombohedral crystals of boron carbide with B_{12} icosahedral coordination [25]. Cubic boron carbon nitride (c-BCN) structure combines the properties of diamond and c-BN and exhibits superior hardness. Furthermore, hexagonal-BCN structures replicate the h-BN semiconducting property and exhibit tunable bandgap. Figure 2.1 shows the phases observed in the ternary B-C-N triangle.

What makes BCN materials interesting is that it is not only possible to tune the composition and structure using different deposition techniques, but distinct composition demonstrates unique properties. This exceptional behavior of BCN materials gathered overwhelming attention in research and industry. BCN materials are reported to demonstrate low dielectric constant value as low as 1.9 [29], excellent hardness and elastic modulus of 33.7 GPa and 256 GPa, respectively [30], a high breakdown voltage of 3.4 MV/cm [31], low friction of coefficient (0.1-0.2) [32], high adhesion [33] and exceptional thermal stability up to 1000°C [34]. Owing to these properties, BCN thin films find electrical applications in the form of supercapacitors, field-effect transistors (FET), high voltage photodetectors. Due to their optical transparency and tunable bandgap, BCN thin films find applications in optoelectronic devices as well as UV detectors [35]. The exceptional mechanical properties such as good wear resistance, high hardness, low friction of coefficient make BCN thin films an ideal candidate material for cutting tools and anti-wear protective coatings [32, 36-39]. Table 2.1 [25] shows the distinguished properties of BCN thin films compared with other commonly used low dielectric materials.

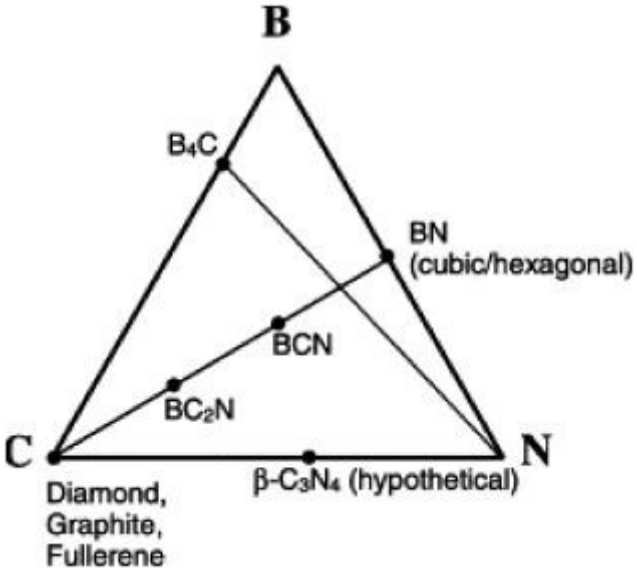

Figure 2.1: Ternary boron-carbon-nitrogen triangle displaying different phases.

Various techniques have been used to synthesize thin and robust films of BCN such as chemical vapor deposition (CVD) [40-42], RF magnetron sputtering [43-45], DC sputtering [39, 46], dual ion beam sputtering [47], high power impulse magnetron sputtering [48], pulsed laser deposition [49-51] and ion-beam assisted deposition (IBAD) [52, 53]. Distinct synthesis conditions assign unique properties to BCN thin films, and growth parameters greatly influence the properties.

Table 2.1: Comparison of BCN thin film properties with other low dielectric materials.

Semiconductor Material	h-BN	SiO_2	SiOC:H	BC:H	BCN
Density (g cm^{-3})	2.2	1.4–2.1	0.9–1.3	1.5 ± 0.08	2.4–2.5
Young's modulus (GPa)	36.5	75.2	3–15	126 ± 5	∼285
Hardness (GPa)	1.5–1.3	7.9	0.2–2.3	1–35	30–40
Stress (MPa)	1–16	21.01	Highly variable	−400 ± 100	150
Energy bandgap (eV)	5.86	8.9	7.9	2.4–3.6	1.9–3.7
Breakdown voltage (MV cm^{-1})	1.5–2.5	>4.3	>6	>5	3.4
Dielectric constant	2–4	3.9	2.2–3.2	3.3 ± 0.15	1.9
Leakage current (Acm^{-2})	(@ 1 MV/cm^{-1}) 10^{-6}	(@ 4 MV/cm^{-1}) 10^{-7} - 10^{-9}	(@ 2 MV/cm^{-1}) 10^{-8} - 10^{-9}	(@ 2 MV/cm^{-1}) 9×10^{-9}	(@1 MV/cm^{-1}) 10^{-5}-10^{-8}
Resistivity (Ω cm)	10^{14}–10^{16}	10^{17}	10^{17}	10^{10}–10^{15}	10^{9}–10^{12}

2.2 Deposition Techniques for BCN Thin Films

2.2.1 Chemical Vapor Deposition

Chemical Vapor Deposition (CVD) is one of the most common techniques to synthesize films in the B-C-N ternary triangle. CVD provides the advantage of producing high-quality films with relative ease of controlling material microstructure and composition. A typical CVD process utilizes volatile precursors that react and form the required material on the substrate surface.

Synthesis of BCN with CVD technique was first reported by Kosalapova et al. in the early 1970s using reactions between carbon and boron in the presence of NH_3 or N_2 [42]. These reactions were attempted at high temperatures of 1800-2000 °C. Several precursors containing mixtures of boron halogenides, hydrides mixed with hydrocarbons, ammonia, nitrogen were used for CVD of BCN thin films. However, further development of BCN synthesis with these precursors was not viable due to their high toxicity and hazardous nature. Since then, significant advancement has been made towards the development of single source organoboron precursor containing boron, carbon, and nitrogen, which are essential to form BCN [54-58]. The first attempt at synthesizing BCN by CVD process using boron trichloride (BCl_3) precursor was reported by Badzian et al. All the films grown were reported to be polycrystalline with composition of $(BN)_xC_{1-x}$ [59]. Apart from BCl_3, BCN has also been reported to be synthesized using the CVD process from diborane precursor (B_2H_6) [60]. Two different mixtures of precursors were used, namely – mixture 1 (B_2H_6 + NH_3 + C_2H_4) and mixture 2 (B_2H_6 + Dimethylamine $(CH_3)_2NH$). The concentrations of B, C, and N in the films produced were reported to be 51.4–63.0 at.%, 6.2–20.5 at.%, and 16.8–38.2 at.%, respectively, for mixture 1 and 77.8–92 at.%, 5.3–16.5 at.%, and 1.8–7.4 at.%, respectively, for mixture 2. The films deposited using mixture 1 were close to the BN region in the BCN composition triangle, whereas the films deposited using mixture 2 were close to the BC region in the composition triangle. Thus, BCN films with different compositions can be obtained by varying the reactive atmosphere in the CVD process.

Microwave PECVD (MW-PECVD) was also used to synthesize BCN thin films using triethylamine borane (TEAB) single-source precursor at microwave powers of 300 W, 400 W for 30 minutes

[40]. The B, C, and N concentration of films deposited using 300 W and 400 W microwave power was recorded to be $B_{50}C_{12}N_{38}$ and $B_{47}C_{16}N_{37}$, respectively. A hybrid B-C-N atomic configuration was identified using XPS. The particle size was 100 nm and 150 nm for the films deposited at 300 W and 400 W microwave power, respectively. The microhardness also displayed an increasing trend with microwave power. This indicates that the grain size and microhardness of BCN thin films can be altered by tuning the microwave power.

2.2.2 Magnetron Sputtering

Magnetron sputtering is a popular technique to deposit superhard BCN thin films as it produces conformal deposition with low cost and low operating temperatures. Ulrich and coworkers used the h-BN target in argon plasma and acetylene (C_2H_2) to RF sputter BCN thin films. The flow rate of C_2H_2 / Ar was observed to significantly affect BCN thin films deposition rate. Stoichiometries of $B_2C_{0.2}N$, $B_2C_{0.5}N$, B_2C_1N, and $B_2C_{1.5}N$ were identified for C_2H_2/Ar gas flow ratios of 0.05%, 0.13%, 0.5%, and 0.8%, respectively [45]. Due to their excellent mechanical and tribological properties, BCN materials with potential for wood cutting tools were investigated by Wu et al. by RF sputtering of B_4C target [33]. The N_2 gas flow was varied at 5, 10, 15, and 20 sccm to achieve different film compositions. They reported a decrease in the B content, increase in critical loads indicating enhanced adhesion and crack propagation resistance with N_2 flow in the deposited BCN coatings. Apart from the reactive gas flow, other process parameters also affect the properties of RF sputtered BCN thin films. Zhuang et al. reported that the bond content in the B-C-N films could be tuned based on the substrate temperature and bias voltage [43].

The correlation between deposition parameters on composition, structure, and mechanical properties of BCN films deposited by DC magnetron sputtering was reported [46]. The N content was varied from 0 to 100% to characterize the bonding structure and the mechanical properties of the film deposited on Si substrates. For 50% N_2, substrate potential between −150 V and −450 V was applied to targets. This deposition technique provides flexibility for tuning the mechanical properties of film for desired applications by proper control of gas mixture.

2.2.3 Pulsed Laser Deposition

The pulsed laser deposition (PLD) technique has developed significantly over the years and is currently used extensively in research as well as industrial thin films production. One of the earliest PLD studies reported the synthesis of BCN thin films from BN-graphite target [49]. The sequential PLD technique facilitates the formation of BCN thin films with different stoichiometries based on substrate temperature variation. BCN films deposited at room temperature (RT) were polycrystalline, whereas films deposited at higher substrate temperatures were amorphous.

Wang et al. reported that laser fluence affects the microstructure, bonding structure, and mechanical properties of BCN thin films [30]. The contents of N–C and B–C bonds in B–C–N films increase with increasing laser fluence, affecting mechanical properties. Increasing the laser fluence from 1.0 J/cm^2 to 3.0J/cm^2 dramatically changes the hardness and elastic modulus of the films. Films synthesized using varying laser fluences were amorphous in nature. At a higher fluence of 3.0J/cm^2, a greater number of hard B–C and sp^3 N–C bonds are observed with a lesser

number of soft sp^2 B–N and N=C bonds. These characteristics designated the films with maximum hardness of 33.7 G Pa and Young's modulus of 256 GPa. Comparing the hardness values achieved for BCN thin films deposited using other techniques such as dual ion beam sputtering [47], the PLD technique to deposit BCN films exhibits a maximum hardness of 33.7 GPa.

Along with favorable mechanical properties, the PLD technique assisted with electron cyclotron resonance (ECR) plasma produces BCN films with excellent adhesion to substrates and high transparency in the near IR region [61]. The nitrogen plasma was generated from the ECR microwave discharge in nitrogen gas. The BCN films exhibit a B/C/N atomic ratio of 3: 1: 3.8. Ying et al. have reported amorphous and nanocrystalline B-C-N hybridization films using nitrogen ion beam assisted laser ablation of B_4C target [26]. B, C, N, O composition for nitrogen ion beam–assisted films were 43%, 15%, 33%, and 9%, respectively.

2.2.4 Ion Beam Assisted Deposition

The ion beam assisted deposition (IBAD) technique combines ion implantation with another PVD technique to deposit thin films. The evaporated material produced by PVD is simultaneously bombarded with the independently generated flux of ions. IBAD is a powerful technique to deposit BCN thin films with preferred composition and bonding structure. BCN films produced by IBAD deposited boron and carbon using electron beam heating, and nitrogen was incorporated using ion implantation [53]. Target materials used were graphite blocks, a mixture of pure boron and C grains, and B_4C blocks. Films produced by electron beam evaporation of (B + C) along with simultaneous N ion implantation acquired B: C: N atomic ratio of 4: 91: 5 at the surface. Whereas

in the case of BCN film produced by electron beam evaporation of B_4C blocks along with N ion implantation acquired B: C: N atomic ratio of 28: 63: 9 at the film surface. It is evident that the target materials affect the atomic elemental composition of the deposited film.

Table 2.2: A summary of BCN thin film synthesis techniques used to achieve some of the best-reported properties in the literature.

Desired Property	Synthesis Technique	Reference
Low dielectric constant (1.9)	PACVD	[29]
High hardness (33.7GPa) and Elastic modulus (256 GPa)	PLD	[30]
UV detection capability	Dual target RF magnetron sputtering	[35]
High breakdown voltage (3.4 MV/cm)	RF magnetron sputtering	[31]
Photoluminescence	Electron-cyclotron-wave-resonance PLD, Dual target RF magnetron sputtering	[62]
High transparency in the near infrared region (80%)	Plasma-assisted PLD	[61]
High adhesion	RF magnetron sputtering	[33]
Low friction coefficient (0.1-0.2)	High power impulse magnetron sputtering	[32]
Electromagnetic wave absorption capability	CVD	[63]
High thermal stability (1000°C)	Direct current unbalanced magnetron sputtering	[34]

BCN film structure evolves from amorphous to hexagonal phase by changing the momentum transfer using the evaporation of B_4C lumps and N_2 ion assistance [64]. E-beam evaporation of B_4C provides the B and C atoms. Ion energies between 100 and 1200 eV and ion current densities up to 0.4 mA/cm^2 were applied to N^2 for ion assistance, impacting the film structure. Table 2.2

[25] shows a summary of BCN film synthesis techniques adopted to achieve some of the best-reported properties in the literature based on all the deposition techniques discussed above.

2.3 Properties of BCN Thin Films

Understanding the fundamental film structure, chemical composition, and other properties regarding the deposition technique is crucial to tuning the BCN thin films for corresponding applications. To explore BCN thin film properties, it is necessary to perform a combination of techniques to investigate electrical, mechanical, morphological, and bonding properties. Additionally, the feasibility of wet and dry etching techniques for ILD thin films is essential for device fabrication process optimization.

2.3.1 Electrical Properties

The BCN hybrid materials in the B-C-N ternary triangle exhibit remarkable electrical properties. These electrical properties can be tuned based on the elemental film composition to satisfy specific requirements for electrical applications. Electrical properties are commonly studied by fabrication metal-insulator-metal (MIM) devices and characterizing the I-V and C-V curves. The electrical properties are strongly influenced by the deposition techniques and synthesizing parameters such as pressure, gas flow, substrate temperature. BCN films deposited using RF magnetron sputtering display decreased dielectric constant with increasing substrate temperature [31]. Figure 2.2 a-b shows the dielectric constant as a function of substrate temperature and gas flow ratio, respectively. The dielectric constant followed a decreasing trend

with substrate deposition temperature. At higher temperatures, BCN thin films possess the lowest C content and highest N content. As a result, the film exhibits more BN-like characteristics. As the k value of BN is lower than BCN, the films show reduced dielectric values. The dielectric constant displayed an increasing varying trend with the gas ratio. The k value reduced with gas ratio from 0.2 to 0.8; however, it suddenly increased for N_2/Ar= 1.0. This increase in the dielectric constant value was attributed to higher capacitance in the thicker films deposited at N_2/Ar= 1.0. It is important to note how tiny changes in the film composition drastically affect the electrical properties of RF magnetron sputtered BCN films.

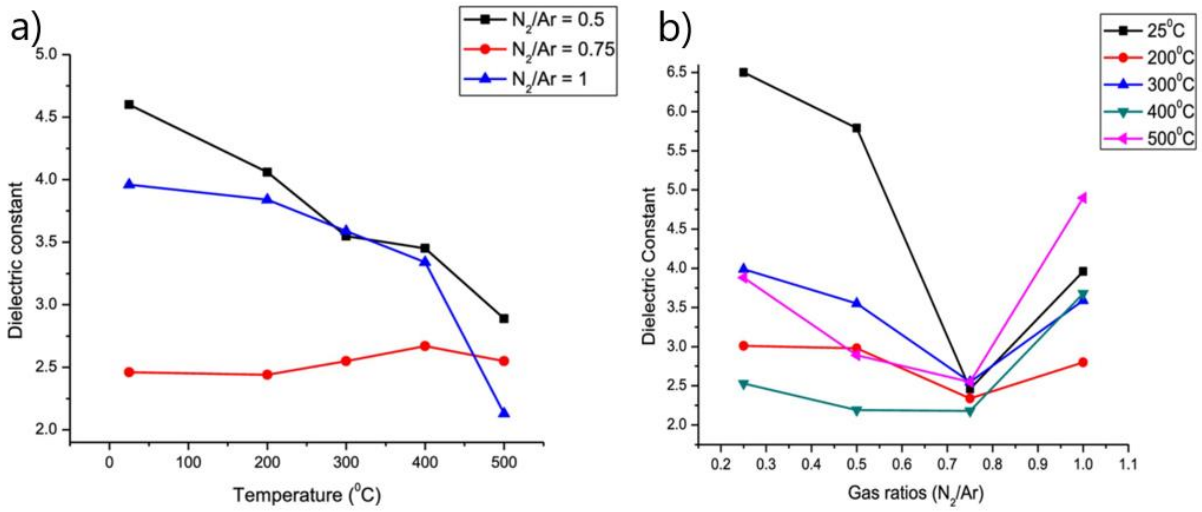

Figure 2.2: Dielectric constant trend of BCN thin films deposited by RF magnetron sputtering as a function of (a) substrate deposition temperature and (b) reactive gas flow ratio.

Multiple studies in the literature report the dependence of electrical properties on the thin film composition. BCN thin films synthesized using PACVD displayed reduced resistivity from 1×10^{12} Ω-cm to 3.4×10^{9} Ω-cm when C composition increased from 6% to 30% [65]. While the resistivity

values were reduced, the dielectric constant was 3.4, which is higher than the dielectric constant value achieved by depositing BCN films using the RF magnetron sputtering technique. BCN films synthesized from N-trimethylborazine precursor from PECVD exhibited a broad range of k values between 2.2 and 8.9 with a change in ammonia gas and deposition temperature (373-973 K) [66].

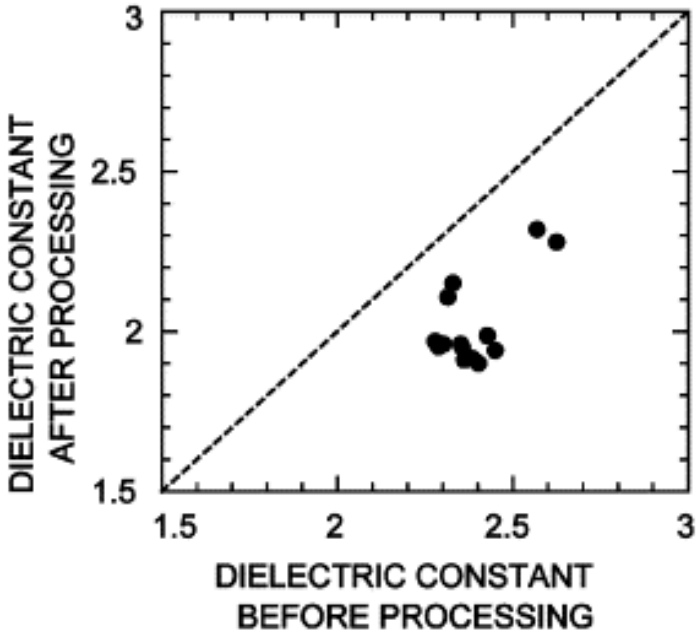

Figure 2.3: The dielectric constant of BCN thin films before and after annealing.

To lower the dielectric constant of BCN films, Umeda et al. attempted to incorporate hydrogen in the BCN thin films using the PACVD technique [29]. The lowest k value of 1.9 was achieved by annealing the films at 400°C. Figure 2.3 shows the reduction in k value observed on annealing the films. The reduction in k value was attributed to increasing C=C and C-H bonds in the BCNH films, reducing the polarization of films. Table 2.3 summarizes all the electrical properties reported in the literature for BCN films deposited using various techniques [25].

Table 2.3: Summary of electrical properties of BCN thin films.

Film Deposition Technique	Dielectric value k	Thickness (nm)	Resistivity ρ (Ω cm)	Breakdown strength E_{bd} (MV/cm)
PACVD	3.4	100 - 300	1×10^{12} - 3.4×10^{9}	nm
Dual target Sputtering	3.9 - 4.6	200 - 400	nm	nm
RF sputtering	2.13	90 - 200	3×10^{12}	3.4
PACVD	2.4	100 - 300	nm	nm
PACVD	2.1	100 - 300	nm	nm
PECVD	2.2 - 8.9	100 - 300	10^{9} -10^{11}	0.1 - 1

2.3.2 Mechanical Properties

2.3.2 (a) Effect of Nitrogen and Carbon Content

BCN thin films belong to the family of diamond materials and hence are frontrunner candidates for protective and hard coatings in cutting tools and other anti-wear applications. Numerous parameters which are known to influence the mechanical properties of BCN thin films are nitrogen content [46, 67], carbon content [68-70], deposition and annealing temperatures [71, 72], and deposition energy [30, 46, 73]. Martinez et al. performed early studies on mechanical properties of sputter-deposited BCN thin films [67]. The atomic nitrogen concentration in the films was varied from 0 to 40% by varying the nitrogen gas mixture during sputtering from 0 to 10%. Microhardness reduced from 26 to 13 GPa, and Young's modulus reduced from 280 to 180 GPa with increasing N_2 content in the sputtering gas mixture. The residual stress and friction coefficient were also observed to decrease with N_2 content. Figure 2.4 a shows the effect of N

content on residual stress and critical load. Figure 2.4 b shows the effect of N content on change in friction coefficient.

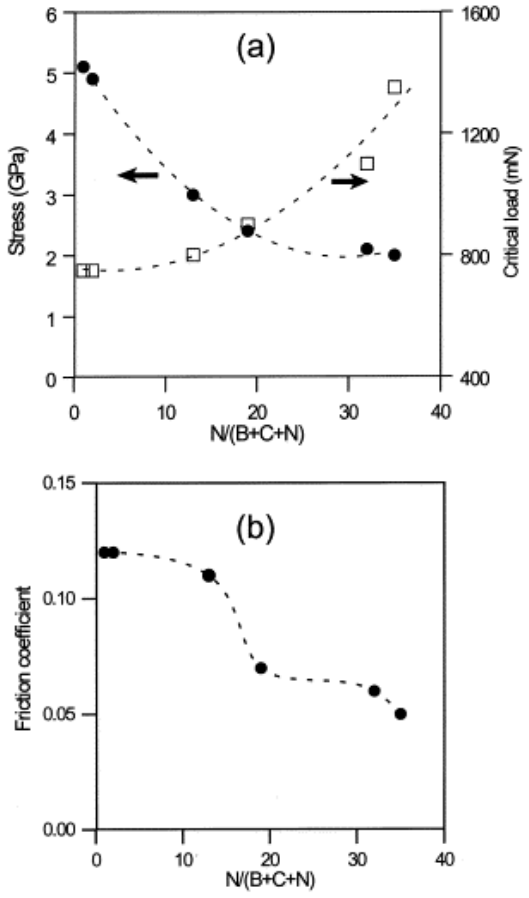

Figure 2.4: Effect of N content in the BCN films on (a) residual stress and critical load and (b) friction coefficient obtained by sliding against diamond.

Our research group had reported a similar trend in reduction in hardness and Young's modulus when nitrogen gas was added to the sputtering chamber, compared to films deposited in the presence of pure Ar [74]. BCN films deposited solely in the presence of Ar gas exhibited high hardness values in the range of 30-40 GPa and a high Young's modulus of ~285 GPa. With the

introduction of nitrogen gas in the sputtering chamber, the hardness and Young's modulus values were observed to significantly reduce to 6-13 GPa and 100-150 GPa, respectively. Similar to nitrogen composition [70], carbon content also plays a vital role in determining the mechanical properties of BCN films. Chen et al. reported a steady increase in the hardness of sputtered BCN films from 11.5 GPa to 18.2 GPa when the C content increased from 26.9 wt% to 61.3 wt%. This increase is attributed to the presence of higher sp^3 N-C bonds in the films [69].

2.3.2 (b) Effect of Deposition Temperature and Post-Deposition Annealing

Both deposition temperature and annealing temperature affect the mechanical properties of BCN thin films. An increase in deposition temperature from RT to 650 °C was found to increase the hardness from 24 GPa to 31 GPa [70]. This enhancement in the hardness values was associated with two reasons. First, the increase in deposition temperature leads to increased crystallinity, subsequently increasing the hardness. Second, with an increase in temperature, the carbon content increased, which helped to increase the hardness. Xu et al. studied the influence of post-deposition annealing on sputter-deposited BCN thin films [34]. Annealing at temperatures from 600°C to 1000°C resulted in a decreasing trend in hardness and Young's modulus values. The hardness and Young's modulus of the as-deposited films were noted to be 27 GPa and 321 GPa, respectively. The values reduce to 19 GPa and 223 GPa, respectively, for films annealed at 1000 °C. Higher annealing temperatures result in the formation of soft sp^2 B-N bonds, which deteriorates the mechanical properties of the films.

2.3.2 (c) Effect of Deposition Energy

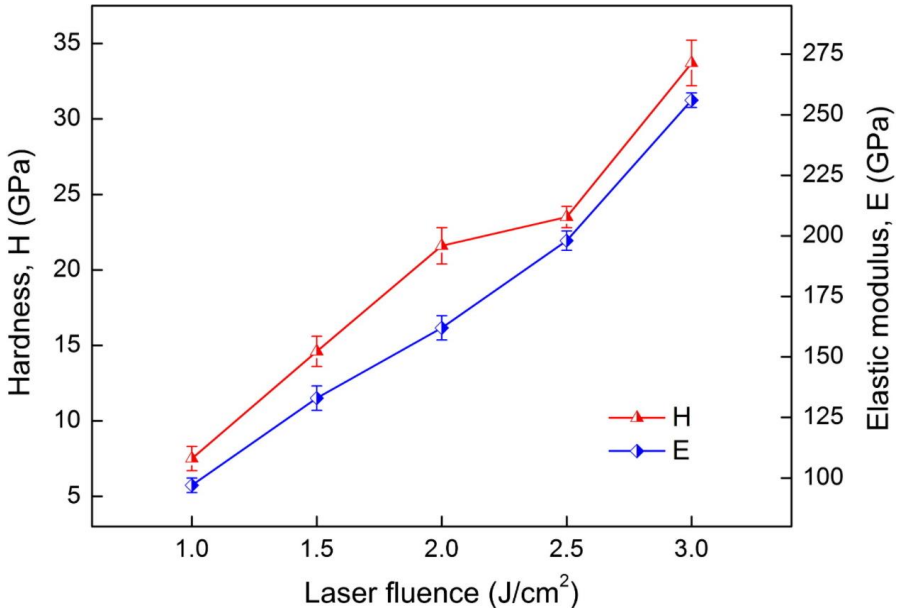

Figure 2.5: Hardness and elastic modulus of B-C-N thin films deposited at varying laser fluence.

The deposition energy used during PVD deposition of thin films plays a crucial role in determining the bonding structure of films, thereby influencing the mechanical properties. The influence of laser fluence on mechanical properties of BCN films deposited using PLD by an Nd:YAG laser was investigated [30]. The films were deposited using a B_4C target at laser fluence from 1 J/cm^2 to 3 J/cm^2. The elastic modulus and hardness values drastically increased with laser fluence, as shown in figure 2.5. Maximum hardness and elastic modulus of 33.7 GPa and 256 GPa were recorded for the film deposited at 3 J/cm^2 fluence. This increment in hardness and elastic modulus was associated with a steady decrease in soft sp^2 B-N bonds and a steady increase in hard B-C and N-C bonds with laser fluence.

Substrate biasing during sputtering of BCN films increased the hardness and Young's modulus along with better adhesion [46, 75]. These results were attributed to the increase in ion energy of incoming ions, which improves the film-forming capabilities and allows for the formation of dense microstructure in the films. The densely networked microstructures have better film strength as well as higher strength between the film-substrate interface. BCN films deposited using microwave-PECVD displayed enhanced mechanical properties with increasing microwave power [40]. This implies the possibility of varying mechanical properties of BCN thin films by varying deposition techniques and growth parameters to engineer the films for suitable applications.

2.3.2 (d) Thermal Stability and Oxidation Resistance

BCN materials are popular due to their extremely high thermal stability and excellent oxidation resistance compared to other similar hard materials. Gago et al. and group were the first to perform thermal stability studies on BCN films deposited using the IBAD technique [76]. The thermal stability of BCN films was compared with other hard materials such as a-C, a-CN_x, h-BCN, c-BCN,s, and B_xC as shown in figure 2.6.

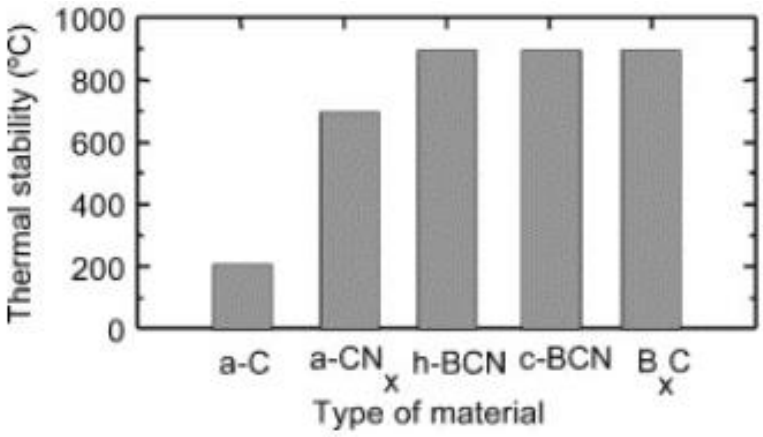

Figure 2.6: Thermal stability comparison of materials in the B-C-N triangle.

BCN films deposited using unbalanced magnetron sputtering of B_4C target and a graphite ring did not decompose to any of its binary phases even when annealed to a high temperature of 1000°C, thus proving its excellent thermal stability [34]. The films were analyzed using the XRD technique. XRD did not reveal diffraction peaks pertaining to B_4C, graphite phases, or any other binary phase. BCN thin films deposited using the IBAD technique from a C/B composite target in the presence of nitrogen gas also exhibit higher oxidation resistance as compared with other similar hard materials [38]. The deposited films were annealed up to 500°C in air. Mass change measurements were performed on BCN and CN_x films post-annealing. The mass change measurements revealed that BCN films were more thermally stable and displayed better resistance to oxidation than the CN_x films.

2.4 Applications of BCN Thin Films

BCN compounds exhibit excellent properties in cubic and hexagonal phases due to the structural similarity with allotropic forms of carbon and boron nitride. While c-BCN gathered attention for its exceptional hardness, h-BCN demonstrates a tunable bandgap with composition and structure to suit desired applications [77]. The flexibility of controlling bandgap by atomic composition and structure makes BCN films a popular candidate material for electronic and photonic devices [78, 79]. Weber et al. have reported that BCN can be used as mask substrates for x-ray lithography due to the optical transparency property of BCN films [80]. As BCN thin films exhibit better oxidation resistance and excellent thermal and chemical stability than graphite and other materials, many research groups have demonstrated BCN applications in electronic devices [81]. BCN materials were reported to be candidates for field emission with a threshold electrical field as low as 4 V/µm and an emission current as high as 0.31 mA [82]. BC_5N films serve as electrochemical sensors to detect dopamine and uric acid selectively in the presence of ascorbic acid [83]. BCN materials also find applications in high voltage photodetectors owing to their low-k values and very high dielectric breakdown strength (~ 3.4 MV/cm) [31].

BCN materials have stimulated research for their use as UV emitters and UV detectors [27, 84]. Our group has previously reported MIM-based BCN UV detectors demonstrated UV detection with maximum photoresponsivity of 6mA/W [35]. These measurements were performed under 365 nm illumination. Figure 2.7 (a) shows the cross-section of the MIM device, and figure 2.7 (b) shows the actual fabricated detector. Figure 2.7 (c) shows the Al-BCN-Au MIM photodetector current under dark and UV conditions. XPS studies revealed several phases such as h-BCN, sp^3 C-

N, B-C, h-BN, and sp^2 C-N. Deep UV photodetectors commonly find applications in military, space communications, NASA spacecraft, flame sending, quick missile plume detection, and environmental issues such as water purification [85].

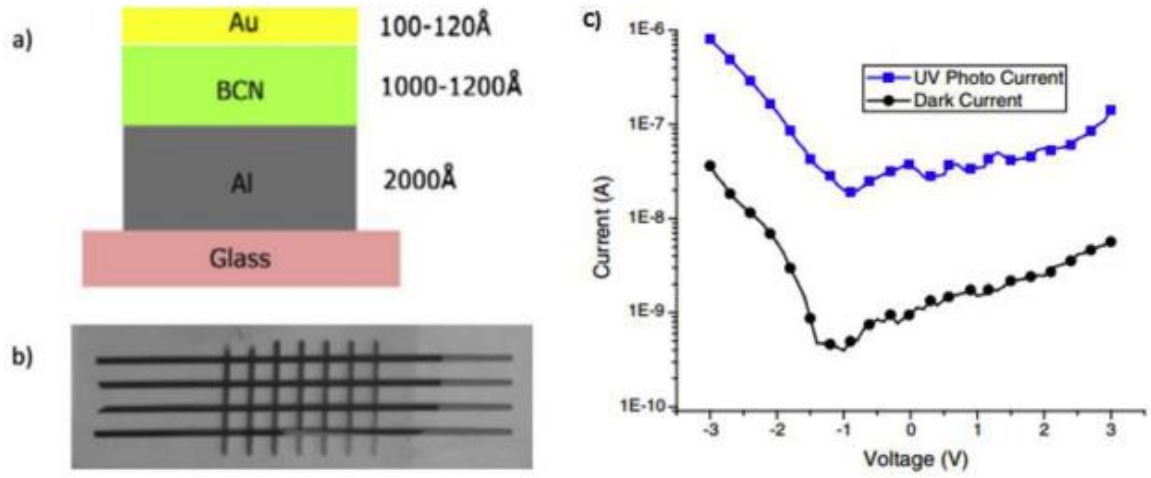

Figure 2.7: BCN device showing (a) schematic of the MIM cross-section, (b) actual fabricated device on the glass substrate, (c) I-V characteristics of MIM device under dark and UV light conditions.

Owing to the popularity of nitride-based phosphors, Wang et al., for the first time, reported a breakthrough development of color emitting metal-free BCNO phosphor [86]. The color of the BCNO phosphors synthesized from boric acid, urea, and water-soluble organic compound polyethylene glycol (PEG) can be tuned over the entire visible light spectrum. Figure 2.8 (a) shows the schematic process used to synthesize the BCNO phosphors and blue BCNO phosphors under 365 nm excitation. Figure 2.8 (b) shows the PL spectra of color-tunable phosphors achieved by

varying PEG/B ratios. The novel BCN-based phosphors are promising for general lighting, automobiles, DNA labeling, bioimaging, and medical applications.

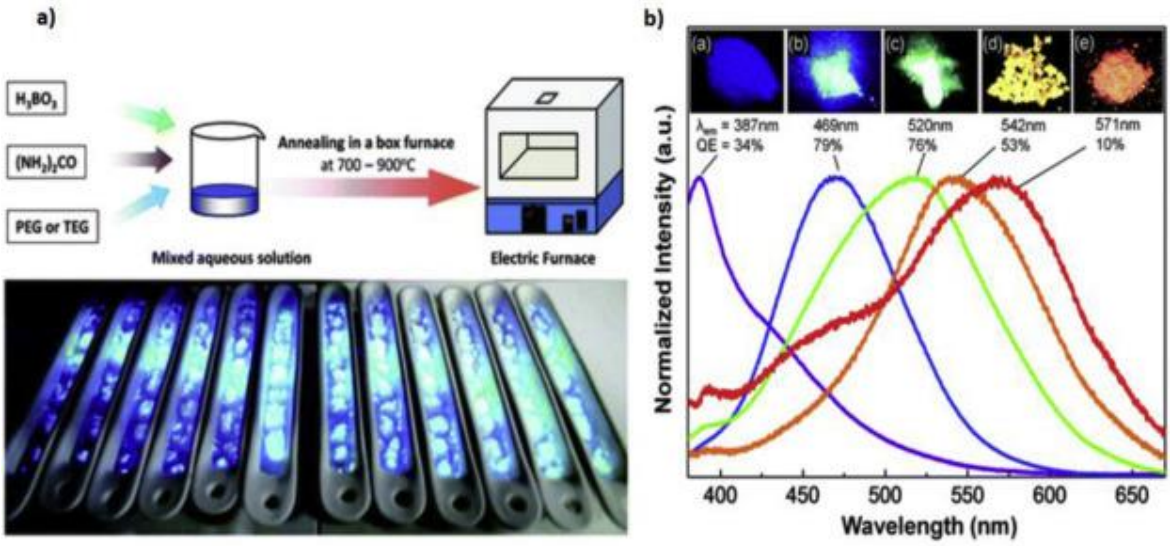

Figure 2.8: (a) Schematic of BCNO synthesis and blue BCNO phosphors under 365 nm illumination and (b) PL spectra of color-tunable BCNO phosphors.

BCN materials are used for hard coatings, low friction, and long-wear applications due to their exceptional mechanical and tribological properties. Multilayers of BCN co-deposited with CrN exhibited a hardness of 25 GPa, low friction coefficient of 0.4-0.5, and low wear rates [87]. BCN has also been identified as a promising material for electromagnetic wave (EMW) absorption material, thus displaying excellent potential for aircraft and industrial shielding material [63].

2.5 Boron Carbon Nitride Nanomaterials

Graphene is popular owing to its fascinating physical properties such as quantum Hall effect and zero bandgap semiconductor with potential applications in nanoelectronics [88]. Substitutional

doping of graphene with other elements such as boron and nitrogen has been proven to modify the structure of graphene, resulting in metal to semiconductor transitions. Substitutional doping of boron and nitrogen in graphene led to development and research on tunable BCN nanomaterials which exhibited wider range of applications. As developing nanomaterials with desirable and tunable properties has been a fundamental challenge for years, BCN nanomaterials which exhibit unique tunable properties with composition attracted great attention. Graphene analogous BCN nanomaterials are categorized as new multifunctional nanomaterials that obtain unique electrical and physical properties, distinct from graphene and h-BN. The elemental composition of C in BCN nanomaterials provides the ability to vary electronic properties such as conductivity, carrier mobility, and concentration [25, 89, 90]. Additionally, BCN nanomaterials possess the ability to control bandgap, making them compatible with photonic devices compared to bandgap-less graphene. BCN nanomaterials have been synthesized in various low-dimensional phases such as 0D nanoparticles [91], 1D nanotubes and nanorods [92], 2D nanosheets [89], and 3D foams [93] as shown in figure 2.9 [25].

BCN nanomaterials have been fundamental towards clean and economical energy storage generation and storage technologies. Due to their unique properties and flexibility of tuning the composition, BCN nanostructures find applications in supercapacitors [94, 95], lithium ion batteries [96], electrolytic and photocatalytic catalysts [97, 98]. Due to their fascinating adsorption properties, BCN nanomaterials are attractive for water purification [99], nano-biotechnology, and nano medicine [100].

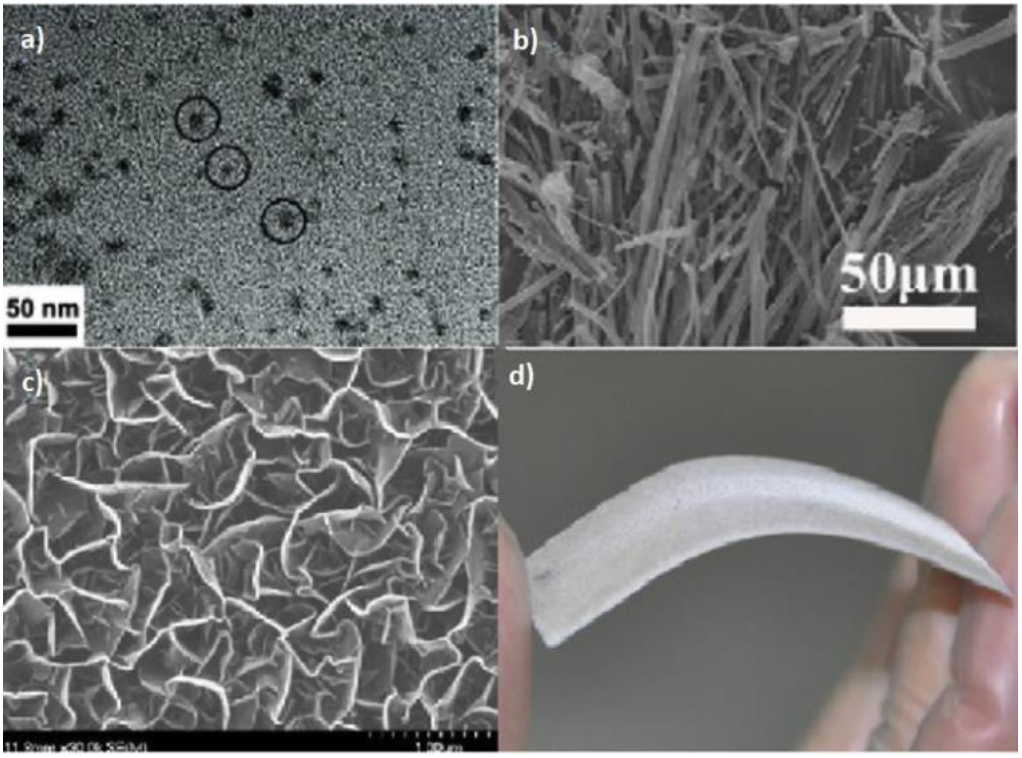

Figure 2.9 : (a) TEM image of 0D BCN nanoparticle, (b) SEM image of 1D BCN nanotube, (c) FESEM image of 2D BCNNs, and (d) Freestanding 3D BCN foam.

2.5.1 Synthesis

Many processes have been reported to synthesize BCN nanomaterials such as arc discharge [101, 102], laser ablation [103], CVD [104, 105], solid-state reactions [106], and thermal catalytic reactions [107]. Although many processes have been demonstrated to synthesize BCN nanostructures, chemical processes are most favored due to their simplicity and means to tune composition to establish desired morphology. Chemical processes from a eutectic salt melt of sodium borohydride and urea (CH_4N_2O) were used to develop BCNO nanoparticles of 5 nm in size

[91]. 1D BCN nanotubes (BCNNTs) are prominent due to their outstanding physical and chemical characteristics, antioxidant capacities up to 900 °C, along with excellent mechanical properties. Unlike the limitation of composition tuning in carbon nanotubes, BCNNTs allow tuning of electrical and optical properties based on the composition and structure of B, C, N atoms. CVD is the most promising approach to synthesize BCNNTs. Li et al. [108] synthesized composition tunable BCNNTs using acid-treated carbon nanotubes, boric acid and ammonia gas as precursors at 830 °C. The temperature of the furnace was maintained for 1 hour, and finally the carbon residue was eliminated to form pure BCNNTs. By controlling the flow of ammonia gas in the furnace, composition tuning with distinct doping levels of B and N atoms was achieved for desired applications.

Integration of graphene-based 2D-Si development to progress towards “more than Moore” era is researched extensively and finds commercial applications in gas, image, and biosensors [109]. 2D BCN, analogous to 2D graphene, has also gained significant attention due to its impressive properties. Karbhal and coworkers reported green, scalable, and facile synthesis techniques of 2D BCN nanosheets (BCNNSs) using boric acid, urea, and glucose. The mixture was heated to 65 °C to form needle like white BN adduct, which was then mixed with glucose in different ratios. The mixture was heated to 900 °C for 5 hours in the presence of argon to achieve BCNNs. These nanosheets showed typical XPS peaks of C-C, B-C, B-N and C-N bonds thus confirming the formation of B-C-N [110].

Unique properties of graphene finding enormous electrical applications fueled the curiosity to inspect the electrical performance of tunable 3D BCN nanostructures. 3D BCN foams were synthesized by doping graphene foams with N and B heteroatoms using the thermal CVD technique [111]. Nickel foam and melamine diborate precursor were loaded inside a furnace at 1000 °C in argon hydrogen gas flow (100: 100) sccm. Subsequently, the nickel foam was removed, and nitrogen gas was introduced inside the furnace to facilitate the growth of BN-graphene foams. The 3D foams thus synthesized exhibited good thermal stability and superior electrocatalytic activity towards oxygen reduction reaction (ORR) than undoped graphene foams.

2.5.2 BCN Nanomaterials Properties and Applications

Graphene analogous BCN nanomaterials have attracted great attention due to the structural similarity with graphene and enhancement in properties due to boron and nitrogen doping. Table 2.4 shows the comparison of graphene and graphene analogous BCN nanostructures [25].

Table 2.4: Comparison in properties of graphene and graphene analogous boron carbon nitride nanostructures

Property	Graphene	BCN nanostructure
Thermal conductivity at RT ($W\ m^{-1}\ K^{-1}$)	1800-5400	0.57
Thermal stability	450-650°C	1000°C
Bandgap	None	2.6 - 5.5 eV
Luminescence	No	Up to DUV region.
Specific capacitance ($mAhg^{-1}$)	372	710
Specific surface area ($m^2\ g^{-1}$)	1520	2911

Investigation of electronic structure and optical properties by Quin et al. demonstrated that $B_{0.38}C_{0.27}N_{0.35}$ nanosheets displayed intense emission at 3.27 eV, thus making BCNNSs a promising candidate for applications in nanoelectronics, catalyst supports, gas adsorption, etc. [89]. Additionally, BCN nanostructures have shown superior performance for supercapacitor applications [110]. BCNNSs achieved by varying the ratio of BN to glucose as BCN (1:3), BCN (1:1), and BCN (3:1) exhibited specific capacitance of 103, 188, and 244 F/g, respectively. They demonstrated high stability, as revealed from the current density of 5A/g and 96% retention of capacitance after 3000 cycles.

One of the most exciting features of BCN nanodomains is its ability to cross-link with itself or other 2D layered materials such as C_3N_4 and MoS_2. Covalently cross-linked BCN materials with other 2D materials is an advanced strategy for generating novel materials with enhanced properties. BCN-MoS_2 nanocomposite demonstrated specific capacitance between 176-243 F/g, and remarkable electrochemical hydrogen evolution reaction (HER) activity [112]. Studies performed on the electrochemical behavior of BCNNS for the first time displayed excellent lithium storage capabilities with a low current density of 30 mA/g and stabilized capacity of 390 mAh/g for 5000 cycles [113]. Following this, multiple reports confirmed BCN nanomaterials as promising candidates for lithium batteries [96, 114].

CHAPTER THREE: METHODOLOGY

Boron carbide thin films were deposited using the radio frequency (RF) magnetron sputtering technique. Magnetron sputtering is a type of physical vapor deposition (PVD) technique used to deposition metals, alloys and compounds, and other materials with thickness up to 5 microns. Figure 3.1 shows a schematic of the sputter deposition process. The substrate to be coated and the sputtering target are placed in a high vacuum chamber containing an inert gas, typically argon. Sputter deposition employs an electrically excited gas plasma in a high vacuum system. High voltage is applied between the cathode (target) and the anode (substrate) to initiate plasma. By applying a high electric field, the gas atoms lose electrons to become positively charged ions which are then accelerated towards the negatively charged target surface with high kinetic energy. Each of these collisions causes atoms at the surface of the target to be ejected into the vacuum environment. This sputtered material now constitutes a vapor stream that travels towards the substrate and sticks to it, forming a thin film.

A magnetron sputtering takes advantage of the above phenomenon by applying a magnetic field perpendicular to the electric field leading to electron confinement near the target surface. Confining the electrons leads to a higher density of the plasma and higher deposition rates and avoids the surface damage to the substrate by the direct impact of electrons.

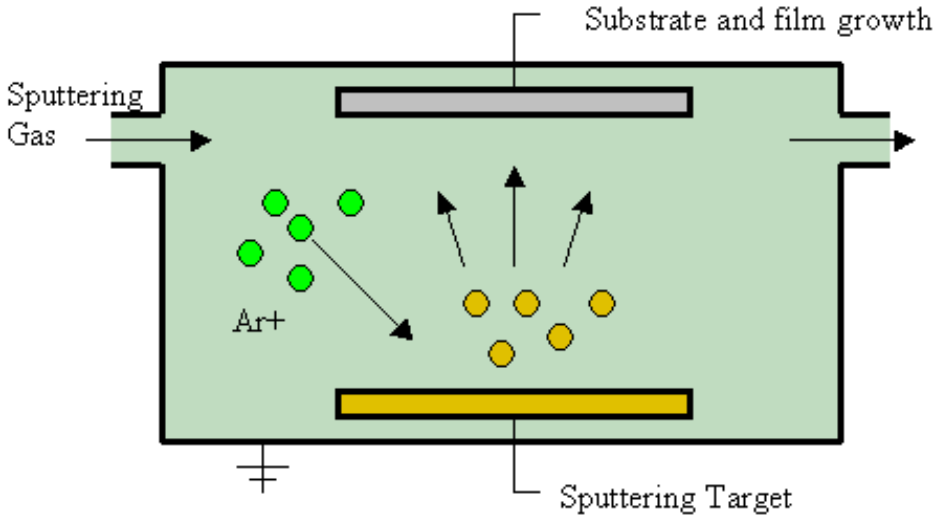

Figure 3.1: Schematic of sputtering deposition technique

All the thin films reported in this study were deposited using RF (13.56 MHz) magnetron sputtering technique in an ultra-high vacuum AJA International Inc. sputtering tool. Figure 3.2 shows the AJA International 3-gun sputtering tool. The sputtering system is connected to four gas lines – argon, nitrogen, hydrogen-argon, and oxygen. This tool can accommodate three targets with 3" diameter. BC and BCN thin films were deposited using individual B_4C, BN or a combination of both using dual-target sputtering. The targets are connected to individual RF power sources for magnetron sputtering.

Figure 3.2: An AJA International 3-gun sputtering system used to sputter thin films of hydrogenated boron carbide.

3.1 Experimental Details of Hydrogenated BC thin films

3.1.1 Thin Film Deposition

Hydrogenated boron carbide thin films (BC:H) were deposited using a 3" diameter powder-pressed B_4C target. The purity of the B_4C target is 99.5%. Corning glass slides and p-type silicon (100) with resistivity ~20 Ω cm were used as substrates to deposit thin films. The target is placed at the cathode, and the substrates are placed at the anode during the deposition. Substrates were cleaned following the traditional method of rinsing with acetone, methanol, DI water and dried with nitrogen gas. Cleaning the substrate surface prevents thin film contamination. The

system base pressure was ~1 x 10^{-7} Torr before the process initiation. Hydrogen gas (3% hydrogen, 97% argon) was introduced in the vacuum chamber using a mass flow controller. Since hydrogen gas is premixed with argon, it will hereafter be referred to as H_2Ar. Total gas flow was set to 20 sccm at a constant deposition pressure of 5 mTorr. The RF power to the B_4C target was maintained at 200 W. The thickness of the films was determined using Dektak 150 stylus profilometer by Veeco, shown in figure 3.3.

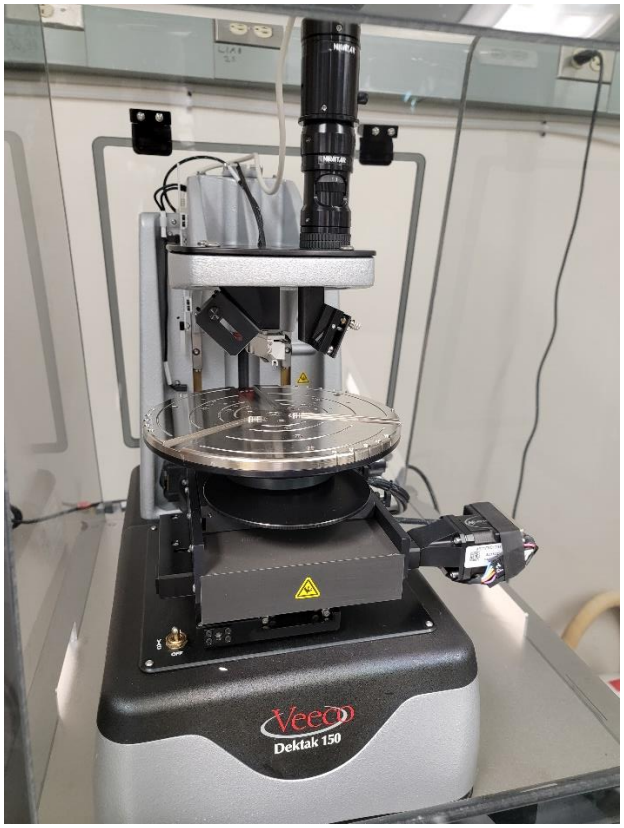

Figure 3.3: Dektak 150 stylus profilometer by Veeco used to measure the thickness of deposited thin films.

The thickness of BC:H films ranged between 1000 Å to 1200 Å. The depositions were performed at four different substrate temperatures of room temperature (RT), 100 °C, 200 °C, and 300 °C. A quartz lamp connected to an automated temperature controller was used to monitor the substrate temperatures.

3.1.2 Fabrication of Metal-Insulator-Metal Devices

Metal-insulator-metal (MIM) structures were fabricated to study the electrical properties of hydrogenated BC films. Glass slides were cleaned using the conventional acetone, methanol, and DI water rinse. Aluminum was used as the top and bottom metal electrode for the MIM structure. Bottom electrodes of 3 mm width Al metal stripes were thermally evaporated on a clean glass substrate using a mechanical mask. Hydrogenated boron carbide thin film is deposited using RF sputtering described in the previous section on top of bottom Al electrodes. Finally, top metal electrodes of Al running perpendicular to the bottom electrodes were thermally evaporated on hydrogenated boron carbide thin film. The thickness of the bottom and top thermally evaporated Al electrodes was ~1500 Å. Figure 3.4 shows the schematic and actual fabricated structure of Al-a-BC:H- Al structure on the glass substrate.

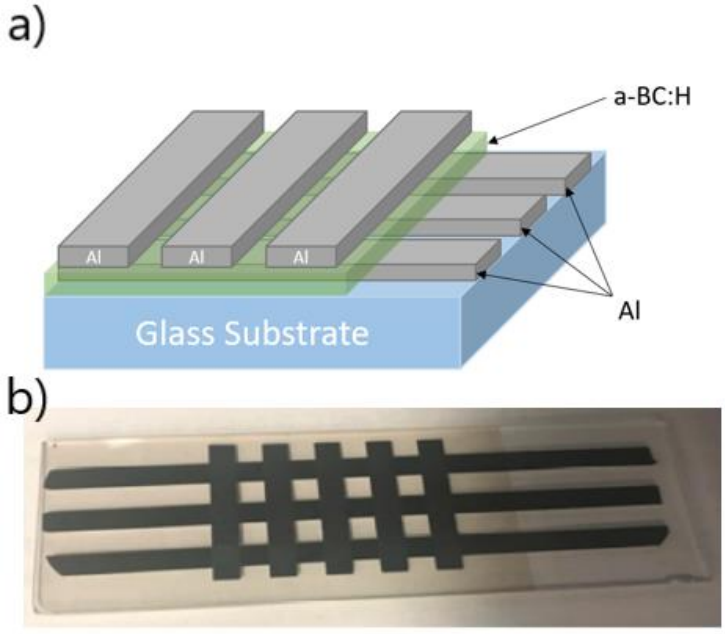

Figure 3.4: (a) Schematic of the cross-sectional view of Al-a-BC:H-Al MIM capacitors; (b) actual fabricated structure for the film deposited at 300 °C consisting of 15 capacitor devices.

3.1.3 Surface Characterization

3.1.3 (a) X-ray Photoelectron Spectroscopy

As the demand for high-performance materials in current and future technologies is skyrocketing, surface analysis of materials has become necessary. Understanding the physical and chemical interactions of elements that occur at the surface or interfaces of material layers helps to decode problems associated with modern materials and investigate their efficacy for several applications. X-ray photoelectron spectroscopy (XPS) is the most widely used surface analysis technique as it can be applied to a broad range of materials. It is a quantitative technique for measuring the elemental composition at the surface of a material and evaluating the

elements chemical bonding states. XPS typically probes to a depth of 10 nm. The sample surface is irradiated by x-ray beams that interact with the atoms electronic shells causing electron ejection. The kinetic energy of the ejected electron depends on the incident photon energy (hv) and the binding energy (BE) of the electron. An electron analyzer is used to measure the energy of emitted photoelectrons. Electrons contained in different subshells have different energies. From the binding energy and intensity of the photoelectron peak, it is possible to identify the composition of the material and its chemical states. XPS can detect all elements except hydrogen and helium.

XPS characterization was performed on films deposited on the silicon substrates using the ESCALAB 250 Xi XPS system (ThermoFisher Scientific, USA), shown in figure 3.5. The sample surface was etched using an Ar ion gun of 1kV for ~10 sec to eliminate surface oxidation. The base pressure during the analysis was 7×10^{-9} Torr. High-resolution scans of B 1s, C 1s, and O 1s spectra are recorded using a monochromatic Al-Kα radiation source (hν = 1486.6 eV) with a pass energy of 20 eV to achieve maximum spectral resolution. B, C, N, and O elements were selected to be identified in the sample from the multispectrum function. Finally, the x-ray gun and the flood gun were turned on to irradiate the samples. XPS scans were deconvoluted using the Avantage Peakfit software (Version 5.99) to identify the chemical functional groups present in the deposited thin films. Finally, XPS curve fitting was performed using the Gaussian/Lorentzian peak shape.

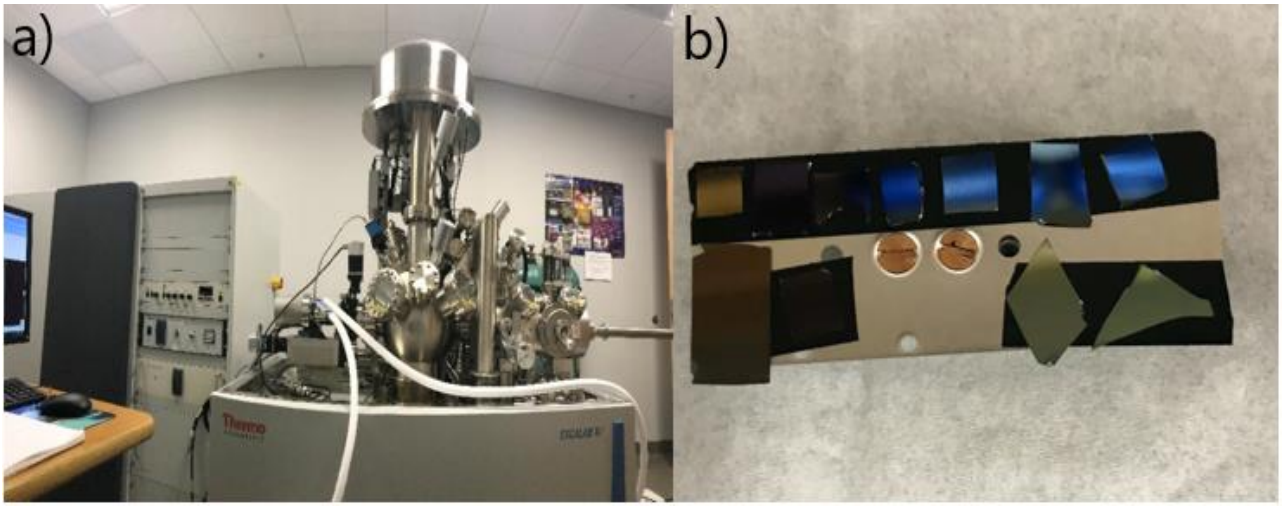

Figure 3.5: (a) Thermo Scientific ESCALAB XI^{+} XPS microprobe, (b) Thin-film samples loaded on XPS holder ready to be transferred to the sample entry lock chamber.

3.1.3 (b) Reflection Electron Energy Loss Spectroscopy

As XPS cannot detect hydrogen, Reflection Electron Energy Loss Spectroscopy (REELS) was used for hydrogen detection in boron carbide thin films. Electron energy loss spectroscopy (EELS) generally involves focusing a beam of monoenergetic electrons typically < 2keV on the surface of the sample. As electrons interact with the material, some undergo inelastic scattering due to loss of kinetic energy. In REELS, the electrons that are both elastically and inelastically scattered are collected using an electron energy analyzer. The REELS spectrum contains the elastic peak as well as the plasmon peaks. These peaks are characteristics of the elements present in the sample and their bonding environment, thus specifying the atomic and chemical bonding data. An interesting capability of REELS is to detect and quantify hydrogen in thin films. As a result, a combined XPS and REELS analysis provides a complete compositional analysis of hydrogenated thin films.

REELS analysis was performed on BC:H thin films deposited on silicon substrates using the Theta Probe of ESCALAB 250 Xi XPS system. The primary electron beam with energy between 1-2 keV for REELS measurement was supplied by an electron gun. The incident beam angle was 60° with respect to the surface, and the electron detection was set normal to the surface. REELS spectra were recorded in the range of 980 eV to 1010 eV kinetic energy. Origin was used to fit the REELS spectra by applying the Savitzky-Golay filter.

3.1.4 Electrical Characterization

The electrical properties such as dielectric constant and resistivity were measured from the MIM devices fabricated on the glass substrates. The insulating film whose electrical properties need to be investigated is sandwiched between the top and bottom metal electrodes, forming a MIM structure. Thermally evaporated Al metal formed the top and bottom electrodes of the MIM device. Al electrodes are 3 mm wide. Top electrodes are deposited perpendicular to the bottom electrodes, thus forming a device area of 3 mm x 3 mm. Each glass substrate consisted of 15 MIM devices. The electrical properties reported are average of these 15 devices.

LCR meter (Keysight E4980A) was used to measure the C-V characteristics at 1 V and 100 kHz frequency. Figure 3.6 (a) shows the Keysight LCR meter used to measure the capacitance values and figure 3.6 (b) shows the probed MIM device. The dielectric constant value (k) was extracted from the measured capacitance values using the following equation:

$$k = \frac{C\ d}{\varepsilon_0 \mathrm{A}}$$

Where C is the capacitance of devices, d is the thickness of the insulating film, ε_0 is the permittivity of free space, and A is the area of capacitor devices.

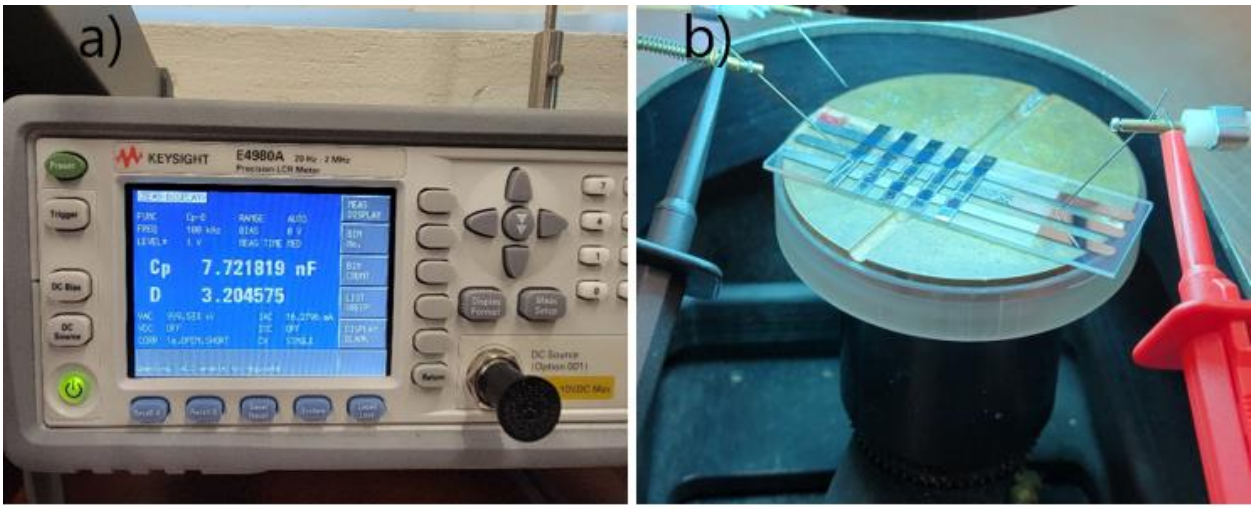

Figure 3.6: (a) Keysight E4980A LCR meter used to measure the capacitance values of MIM detector at 1V, 100 kHz, (b) probed MIM device.

I-V characteristics were measured on MIM devices using a 2450 Keithley source measurement unit, shown in figure 3.7. From the I-V measurements, the resistivity of the films was extracted using the following equation:

$$\rho = R\,\frac{A}{L}$$

Where ρ is the resistivity in Ωcm, R is the resistance extracted from I-V curves, A is the area of MIM devices, and L is the length or thickness of the BC:H film.

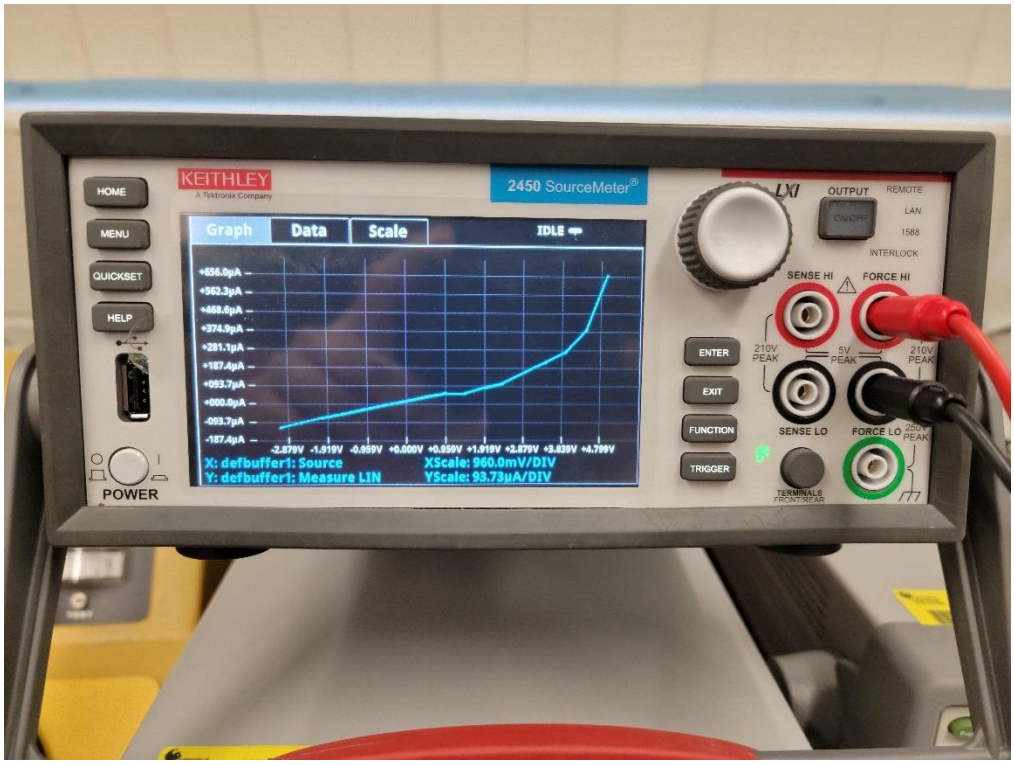

Figure 3.7: Keithley source measurement unit used to measure the I-V characteristics of MIM devices.

3.1.5 Optical Characterization

Materials in the B-C-N ternary triangle are popular due to their wide bandgap and finds various optoelectronic applications. As a result, it is essential to investigate the impact of hydrogenation and substrate temperature on the optical properties of BC:H thin films. Optical characterization of BC:H thin films were performed using a UV-Visible spectrophotometer (Cary 100, Varian), as shown in figure 3.8. The transmission values of BC:H thin films deposited at different substrate temperatures were recorded. Optical transmission values (% T) were used to calculate the optical density and absorption coefficient (α) for thin films as shown below:

$$\alpha = 2.303 * \mathrm{OD} = \left(\frac{-2.303}{t}\right) \log_{10}(\%\, T)$$

where OD is the optical density and t is the thickness of the deposited film. Optical bandgap (E_g) for films deposited at different substrate temperatures were extracted from the Tauc plot using the following equation:

$$(\alpha h\nu)^{\left(\frac{1}{n}\right)} = B\ (\ h\nu - Eg)$$

where $h\nu$ is the incident photon energy, B is a constant, and Eg is the optical band gap. Typically, the n value is defined as 2 for amorphous films. A Tauc plot displays $(\alpha h\nu)^{\left(\frac{1}{n}\right)}$ on y-axis plotted as a function of the photon energy $(h\nu)$ on the x-axis. Extrapolating the linear region of this curve yields the energy of the optical bandgap of the material.

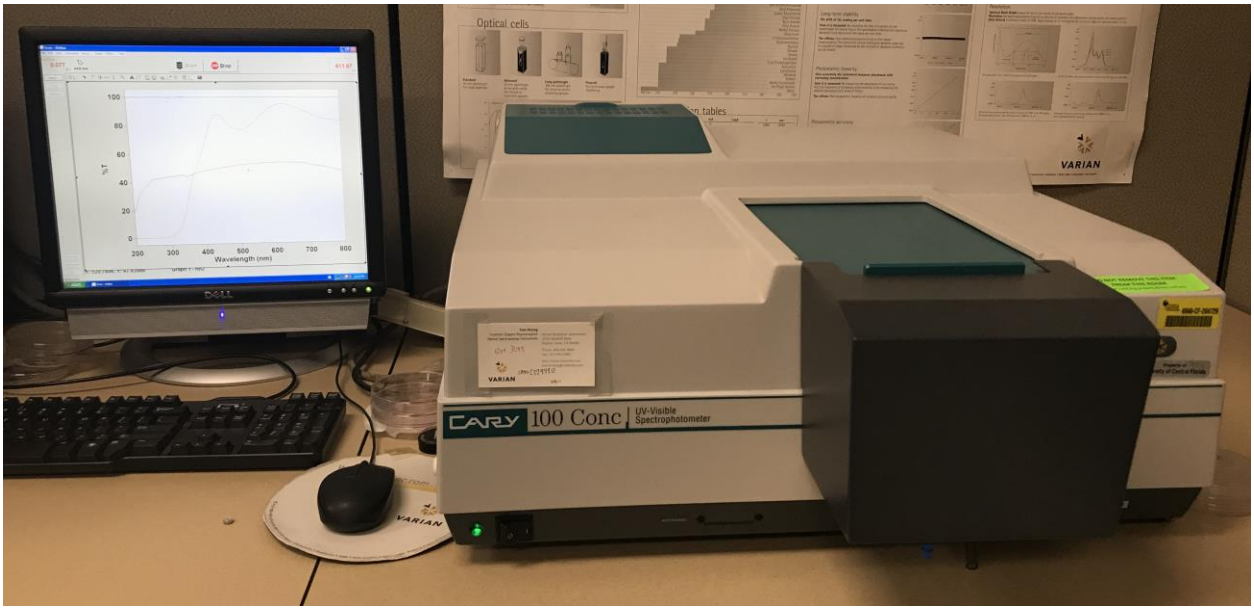

Figure 3.8: Cary 100 UV-Visible spectrophotometer used for optical characterization of thin films.

3.2 Experimental Details of 3% Hydrogenated BCN Thin Films for Mechanical and Photoluminescence Studies

3.2.1 Thin Film Deposition

Dual target RF magnetron sputtering from B_4C and BN targets was performed to deposit BCN thin films. Oxidized silicon wafers with an oxide thickness of ~4000 Å and glass slides were used as substrates. The substrates were cleaned by rinsing with acetone, methanol, DI water, and blow-dried with nitrogen. The substrates were placed on a rotating substrate holder with a rotation speed set to 20 rpm to achieve uniform film thickness. Both the B_4C and BN targets used were powder pressed and had 99.5 % purity. Both the targets face the substrate holder at an angle of 45°. The deposition chamber was evacuated to a base pressure of ~$1x10^{-7}$ Torr before deposition. Hydrogen-argon (3% hydrogen, 97% argon) and nitrogen were the two reactive gases used to deposit BCN:H thin films. This study aimed at investigating the influence of hydrogenation and substrate temperature on mechanical properties and photoluminescence of BCN thin films. As a result, the experimental structure can be divided into two sets, one designed to vary the hydrogen gas flow and the other designed to vary the substrate temperature. In the first set of experiments, the reactive gas flow was varied, and the substrate temperature was maintained constant at room temperature. The H_2Ar to ($H_2Ar + N_2$) gas ratio was varied from 0 to 1 in steps of 0.2, whereas the total gas flow to the deposition chamber was set to 20 sccm. In the second set of depositions, the reactive gas flow ratio was maintained constant at 1, and BCN films were deposited at varying substrate temperatures from RT to 400 °C. Identical sputtering power of 200 W was provided to both B_4C and BN targets at a deposition pressure of 5 mTorr. Glass substrates

were used to measure the thin film thickness. The thickness of BCN:H thin films was measured using Dektak 150 stylus profilometer, and it ranged between 2000 Å and 3000 Å. Table 3.1 shows the gas flow and substrate temperature computations used to deposit BCN films.

Table 3.1: Variations in hydrogen gas flow ratios and substrate temperature used to deposit BCN thin films.

Film	H_2Ar / (H_2Ar + N_2)	H_2Ar	N_2	Deposition Temperature (°C)
A	0	0	20	RT
B	0.2	4	16	RT
C	0.4	8	12	RT
D	0.6	12	8	RT
E	0.8	16	4	RT
F	1.0	20	0	RT
G	1.0	20	0	100
H	1.0	20	0	200
I	1.0	20	0	300
J	1.0	20	0	400

3.2.2 Surface Characterization

3.2.2 (a) Energy Dispersive X-Ray Spectroscopy

The energy-dispersive x-ray spectroscopy (EDS) is an analytical method that allows the elemental identification of materials. EDS systems are generally attached to electron microscopy instruments such as scanning electron microscopy (SEM) or transmission electron microscopy (TEM). EDS relies on the interaction of x-ray excitation on the sample surface. An energetic beam of electrons focused on the sample excites the inner electron causing it to eject from its shell. A higher energy outer electron proceeds to fill its place and the difference in energy levels is

released in the form of x-rays. The energy of x-rays emitted are characteristic of specific elements and are collected by the detector. EDS analysis generates a spectrum that displays peaks correlating to the elemental composition of the surface under investigation.

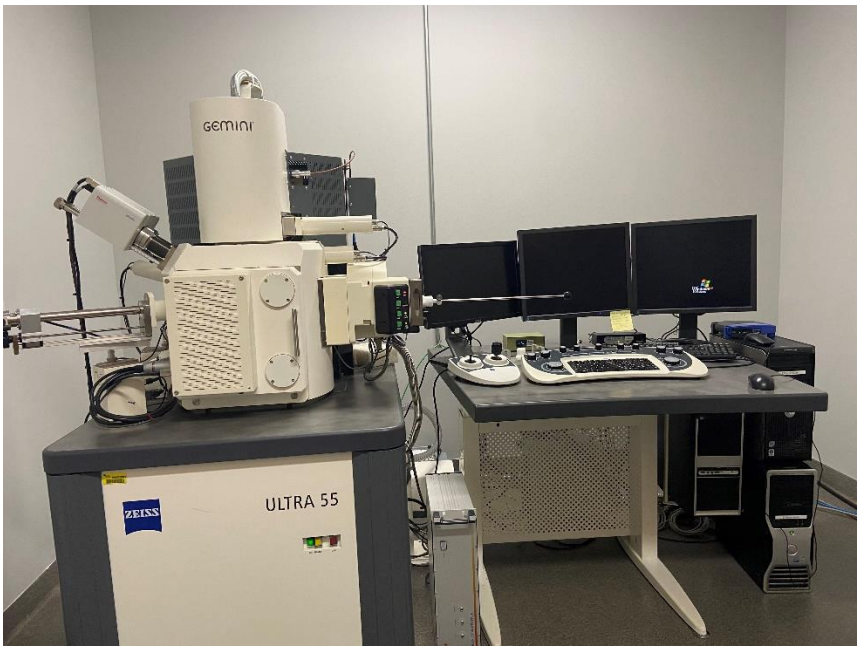

Figure 3.9: Zeiss ULTRA – 55 SEM equipped with Thermo Scientific™ NORAN™ system 7 used for EDS analysis of BCN thin films.

EDS was performed to identify the compositional analysis of hydrogenated BCN film deposited. As BCN thin films exhibit unique properties for distinct composition, it is essential to explore the composition of films for potential applications. BCN:H films deposited on oxidized silicon substrates were used for EDS. Figure 3.9 shows the SEM (Zeiss ULTRA-55) equipped with the Thermo Scientific™ NORAN™ system 7 used to identify the elemental composition of BCN thin

films. The EDS data was acquired at an operating voltage of 5 kV and a working distance of 13 mm.

3.2.2 (b) Fourier Transform Infrared Spectroscopy

Fourier transform infrared spectroscopy (FTIR) is a technique used to acquire an infrared spectrum of absorption or emission of a solid, liquid, or gas. When IR radiation is passed through a sample, the sample molecules selectively absorb specific wavelengths, which causes a change in dipole moment and transmits some wavelengths. Consequently, the vibrational energy levels of the sample molecules are modified. The intensity of absorption or transmission peaks is related to the change in dipole moment and possible transitions in the vibrational energy levels. The resulting signal at the detector is characteristic of the molecular composition of the sample. As a result, analysis of the infrared spectrum provides molecular interaction of the sample.

Figure 3.10: Jasco FT/IR 6600 spectrometer used to detect chemical bonding in the BCN thin films.

FTIR for BCN:H thin films were recorded using the Jasco FT/IR 6600 spectrometer equipped with a Ge/KBr beam splitter, as shown in figure 3.10. This equipment is located in the Department of Chemistry at the University of Central Florida (UCF). A DLaTGS (deuterated lanthanum α-alanine doped triglycine sulfate) detector was employed to detect the spectral fingerprints of the thin films. Transmission FTIR spectra were collected from 400 – 4000 cm^{-1} with a resolution of 4 cm^{-1}.

3.2.3 Mechanical Properties

Nanoindentation technique allows measurements of mechanical properties such as modulus, hardness, fracture toughness, or yield strength of materials existing in different shapes, sizes, and scales. This technique is remarkable as it can measure properties for various materials ranging

from extremely hard alloys to soft biomaterials. Hardness tests are performed by using an indenter probe displaced into the surface under a specific load. The size and depth of the indentation are essential parameters to determine the hardness of the surface. Uniaxial compression and tensile testing are performed to determine the elastic modulus of the surfaces.

Hysitron Triboindenter shown in figure 3.11 at the University of South Florida, was utilized to characterize mechanical properties such as hardness and Young's modulus of BCN:H thin films. This triboindenter is equipped with a Berkovich diamond tip. A three-plate capacitive transducer is used as an internal part of the indenter to execute measurements. The Triboscan software was used to set up all the parameters required for the characterization of mechanical properties. Indentation time was set to 4 s for both loading and unloading steps. A fixed distance of 30 μm was maintained between two neighboring indents during the measurements. Multiple indentations were made for each film at a load of 4mN. Hardness and Young's modulus values obtained through numerous indentations were averaged for each film.

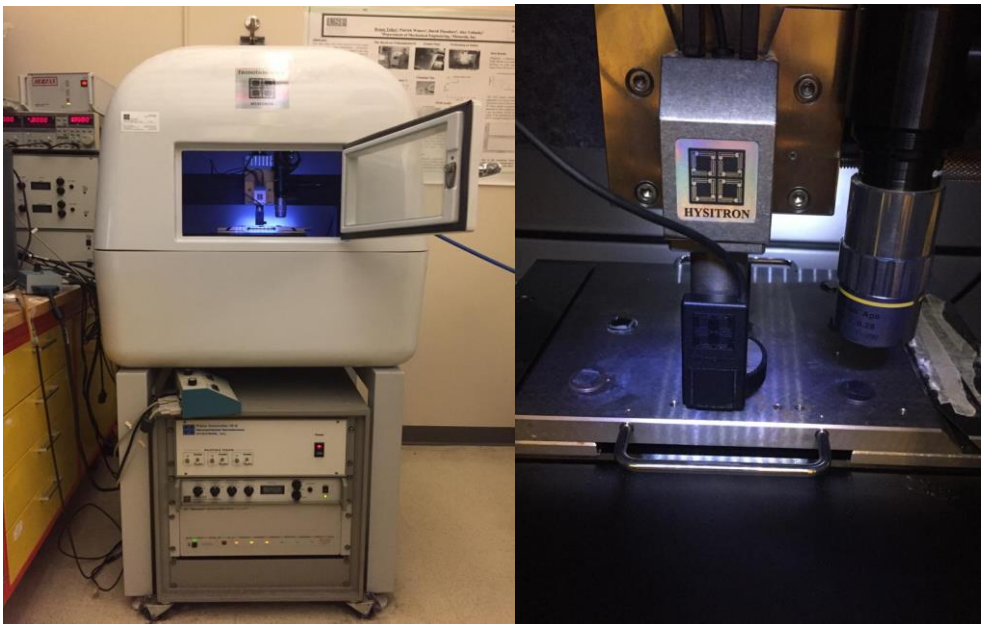

Figure 3.11: Hysitron Tribointeder used to characterize mechanical properties of thin films.

3.2.4 Photoluminescence Studies

Photoluminescence (PL) is an optical phenomenon displayed by semiconductors that gives light emissions after absorbing incident light with higher energy than the bandgap energy of the semiconductor. Photoexcitation causes the electrons to get excited to higher energy levels, and relaxing back to its lower energy state is accompanied by emitting photons. The emission of phonons or luminescence through this process is termed as PL. The PL measurements were performed on BCN:H thin films using a FluoroMax-3 (Horiba Jobin Yvon, NJ) shown in figure 3.12. This spectrometer is located in the Department of Chemistry at UCF. The measurement equipment consists of a 150 W Xenon arc lamp as the light source. The 1200 grooves mm^{-1} gratings are blazed at 330 nm (excitation) and 500 nm (emission). A photomultiplier tube

detector was operated in the photon-counting mode. The measurements were performed at RT and 77 K on a custom fiber optic probe (FOP) using two excitation and emission fibers (8 around 2 configurations). The copper tube used to hold the custom fibers provided mechanical support to immerse the samples in cryogens. Commercially available software (DataMax) was used for automated scanning and data acquisition.

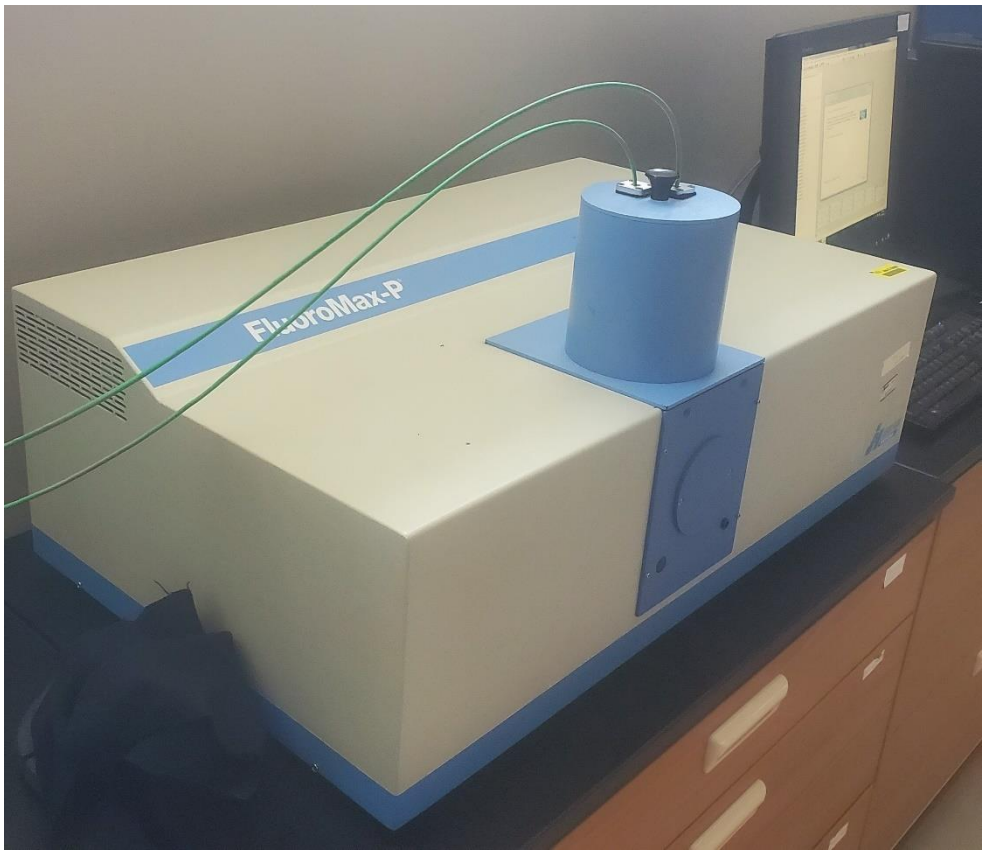

Figure 3.12: FluoroMax-3 spectrometer by Horiba used for PL studies at RT and 77K.

3.3 Experimental Details of 99.99% Hydrogenated BCN Thin Films

3.3.1 Thin Film Deposition

BCN and BCN:H thin films were deposited by dual-target sputtering using B_4C and BN targets. The base pressure of the deposition chamber was 1×10^{-7} Torr prior to the deposition. Thin films were deposited in the presence of reactive gas of N_2, H_2, and inert Ar. The H_2/N_2 gas flow was varied from 0/10 to 10/10 while maintaining Ar flow constant at 10 sccm for all depositions. Thus, the total gas flow in the deposition chamber was 20 sccm. The N_2 gas flow was reduced from 10 to 0 in steps of 2 with a corresponding increase in H_2 gas flow at constant Ar gas flow. Thus the total H_2 gas flow in the deposition chamber was varied from 0% (0/20) to 50% (10/20). Table 3.2 shows the gas flow combinations used for deposition of BCN and BCN:H thin films. Both the targets of B_4C and BN were sputtered at RF power of 200 W at 5 mTorr deposition pressure. The substrates were rotated on the substrate holder at 20 rpm speed to achieve uniform film thickness. Thin films were deposited on dual side polished Si wafers for surface analysis and glass substrates for electrical and optical characterization. The Si wafers and glass substrates were cleaned using the standard procedure of acetone, methanol, DI water rinse, and air-dried with nitrogen gas.

Table 3.2 : Variations in H_2/N_2 gas flow ratios performed during depositions

Film	% H_2	Ar	N_2	H_2
BCN	0	10	10	0
BCN:H10	10	10	8	2
BCN:H20	20	10	6	4
BCN:H30	30	10	4	6
BCN:H40	40	10	2	8
BCN:H50	50	10	0	10

3.3.2 Surface Characterization

3.3.2 (a) X-ray Photoelectron Spectroscopy

Thin films deposited on silicon wafers were examined using XPS for elemental composition and bonding structure following the procedure explained in section 3.1.3 (a).

3.3.2 (b) Fourier Transform Infrared Spectroscopy

As XPS cannot detect hydrogen, the chemical bonding between B, C, N, and H atoms in the BCN and BCN:H thin films were analyzed using FTIR. Vacuum bench BOMEM DA8 FTIR spectrometer with a resolution of 4 cm^{-1} shown in figure 3.13, was used to record the transmittance spectra of thin films. This equipment is located in the Department of Physics at UCF. Thin films deposited on dual side polished Si wafers were illuminated using a Globar light source with a KBr beam splitter. The IR signal was detected using a liquid nitrogen cooled mercury cadmium telluride (MCT) detector in the wavenumber range of 500 – 4000 cm^{-1}.

Figure 3.13: Vacuum bench BOMEM DA8 FTIR spectrometer equipped with MCT detector.

3.3.3 Electrical Characterizations

The electrical characteristics such as the dielectric constant and resistivity of BCN and BCN:H thin films were measured from the MIM devices following the procedure explained in section 3.1.4.

3.3.4 Optical Properties

The influence of hydrogenation on optical properties of BCN thin films was investigated using Cary 100 UV-Visible spectrophotometer. The details of measurements and analysis are explained in section 3.1.5.

3.4 Experimental Details of BCN Nano-Coatings for Bacterial Inhibition

3.4.1 Nano-Coating Deposition

BCN and TiO_2 nano-coatings were deposited using RF magnetron sputtering. Central Venous Catheters (CVCs) were cut into 7cm long segments for deposition of nano-coatings. Catheters are coated in a two-step process. Since the surface of CVCs is cylindrical, when it is placed on the substrate holder, the surface in contact with the holder does not get coated. Hence the cylindrical catheters are rotated after the first deposition, and the uncoated side is exposed for deposition on the second run. BCN nano-coatings were deposited in the ultra high-vacuum AJA International sputtering system. The base pressure of the deposition chamber was $1x10^{-7}$ Torr before process initiation. A three-inch diameter B_4C target with 99.9% purity is used along with reactive nitrogen gas to deposit BCN nano-coatings. N_2/Ar gas ratio was 0.25, while the total gas flow into the deposition chamber was 20 sccm. RF power to B_4C target was 200 W at a deposition pressure of 5 mTorr.

TiO_2 nano-coatings were deposited on CVCs using Ti target in an in-house sputtering system that can accommodate one 2" target. The deposition was performed in the presence of O_2/Ar = 0.25. The total gas flow in the deposition chamber was 20 sccm. Ti target was sputtered at RF power

of 50 W and deposition pressure of 10 mTorr. Both BCN and TiO_2 nano-coatings were deposited at room temperature. The film thickness of BCN and TiO_2 nano-coatings was measured using Dektak 150 stylus profilometer (Veeco). The thickness of both the nano-coatings ranged between 80-90 nm.

3.4.2 Surface Characterization of Nano-Coatings

3.4.2 (a) Scanning Electron Microscopy

The scanning electron microscope (SEM) focuses a beam of high-energy electrons on the sample surface to produce a variety of signals. These signals include secondary electrons, backscattered electrons, diffracted backscattered electrons that provide crucial information about the sample. The electron-sample interactions reveal information including morphology, chemical composition, structure, and homogeneity of the sample surface. Secondary electrons and backscattered electrons are used for sample imaging. Secondary electrons provide information about sample morphology, and backscattered electrons are valuable for illustrating contrasts in the compositional analysis of the sample. The FEI NOVA 430 SEM was used to observe morphological features on U-C, BCN-C, and TiO_2-C. This is a high-resolution scanning electron microscope that can image features down to the nanometer range using its backscatter and through a lens detector. It has capabilities of very low kV characterization as well as analytical capabilities. High-resolution imaging can be obtained even on non-conductive nanomaterials and surfaces.

3.4.2 (b) Atomic Force Microscopy

U-C and BCN-C surface properties were determined using the Dimension 3100 scanning probe microscope atomic force microscope SPM/AFM. It produces high-resolution three-dimensional images by scanning a sharp tip over the surface of the sample. The tip is mounted on a flexible cantilever which forms one end of a cylindrical piezoelectric tube. The piezoelectric tube deflects horizontally on the application of voltage to X and Y electrodes to produce a precise raster scan over the sample surface. The voltage applied to the Z electrode on the piezo tube controls the height of the tip. Thus, the tip moves across the surface following the contours of the topography and plots the surface image. CVCs coated with nano-coatings were measured using the SPM/AFM in non-contact tapping mode. In this mode, the tip oscillates in close proximity of the sample surface using interactive forces without contacting the surface, thus facilitating non-invasive and highly accurate topography imaging. Catheter surface area of 100 μm^2 was scanned for comparison. Additionally, distinct 10 μm^2 surface scans displaying the surface peaks and valleys were also recorded.

3.4.3 Bacterial Growth

To study the efficacy of RF magnetron sputtered nano-coatings on bacterial inhibition, E.coli K-12 and B.cereus bacterial cultures were used. A single bacterial colony of both E.coli and B.cereus was inoculated in Luria Broth (LB) and incubated overnight at 37°C in static conditions. LB is a commonly used medium for bacterial cultivation and growth. One liter of sterile medium comprises 10 grams of tryptone, 5 grams of yeast, and 10 grams of sodium chloride, with a pH

value of 7.0. A cell density of $5x10^4$ cells ml^{-1} was achieved through inoculation. Once the serial dilutions of bacterial cultures were available, U-C, BCN-C, and TiO_2-C segments of 1 cm length were immersed in 5 ml culture tubes with sufficient aeration. These culture tubes were incubated for 6 hours at 37°C for E.coli and 30°C for B.cereus.

After incubation, the catheter segments were removed from the culture tubes using sterile forceps and rinsed in tubes of sterile water. The catheter surfaces were rolled back and forth on the surface of the nutrient plate using the standard roll plate method [115, 116]. Nutrient agar plate was used for E.coli, whereas blood agar plate was used for B.cereus. Culture plates were covered and incubated for 24 hours at 37°C for E.coli and 30°C for B.cereus. The number of colonies in both the plates were counted manually and recorded after the incubation period. All the experimental values were obtained in triplicates for both E.coli and B.cereus bacterial colonies for this study.

3.4.4 Biofilm Formation and Analysis

For biofilm formation, serial dilutions of E.coli K-12 and B.cereus bacterial cultures were made with Luria broth to achieve a cell density of 5×10^6 cells ml^{-1}. 1 cm long U-C and BCN-C segments were immersed in 5 ml culture tubes with adequate aeration. Culture tubes were incubated at 37°C for 6 hours at static conditions. After incubation, the catheter segments are removed and rinsed in sterile water. Rinsed catheters were inserted into culture tubes containing 2 ml of Luria broth. The biofilm was allowed to develop on catheters by incubating at 37°C for E.coli and 30°C for B.cereus under static conditions.

Catheter segments were removed and rinsed in sterile water, and transferred to 96 well microtiter plate stained with 0.1% crystal violet (aqueous). 125 µl of 30% acetic acid was dripped onto each catheter surface. This allows the adhered biofilm to solubilize in their respective wells. The optical density of adherent biofilm stained with crystal violet was measured using SpectraMax iD3 and iD5 Multi-Mode Microplate Reader. This equipment measures absorbance, fluorescence, and luminescence of samples. Optical densities of E.coli and B.cereus biofilms were recorded by measuring absorbance at 550 nm. 30% acetic acid was used as a baseline to report optical density.

3.4.5 Statistical Analysis

All experiments and measurements were performed in triplicates on each catheter for statistical accountability. One-tailed student t-test analysis was performed, and the probability value (p-value) is reported to represent the statistical significance of the obtained data.

CHAPTER FOUR: RESULTS AND DISCUSSION

4.1 Hydrogenated Boron Carbide Thin Films

4.1.1 Surface Characterization

4.1.1 (a) X-ray Photoelectron Spectroscopy

The chemical composition and surface chemistry of BC:H thin films deposited by RF magnetron sputtering of B_4C target were investigated using XPS. The sample surface was etched using low energy Ar ion gun at 1 kV for ~10 sec prior to XPS to eliminate the surface oxidation. Figure 4.1 shows the high-resolution scans of B 1s, C 1s, and O 1s spectra for the film deposited at RT. Prominent peaks in the B 1s region located at 191 eV and 192.5 eV are assigned to B-C-O and B-O bonds, respectively [117, 118]. This implies that the primary interactions of boron in the film correspond to B-C-O and B-O, with B-C-O bonding being dominant. The presence of both B-C-O and B-O bonds also suggests higher oxidation of boron atoms in the deposited films. The C 1s spectra can be divided into three components centered at 284.8 eV, 286.4, and 288 eV. The peak at 284.8 eV with high intensity is attributed to sp^2 C-C and C-H bonding in the films [119]. The shoulder peak appearing at 286.4 eV is assigned to C-O-H and C-O-C bonding, whereas the peak at 288 eV is assigned to C=O [120]. This suggests C-C and C-H are dominating components in the C 1s spectra, along with evidence of C partially bonding with O in the films. The O 1s spectra are fitted with two peaks centered at 530.6 eV and 532.5 eV attributed to C-O-H and O-B bonding, respectively [120, 121]. These bonding configurations were also verified through the B 1s and C 1s spectra.

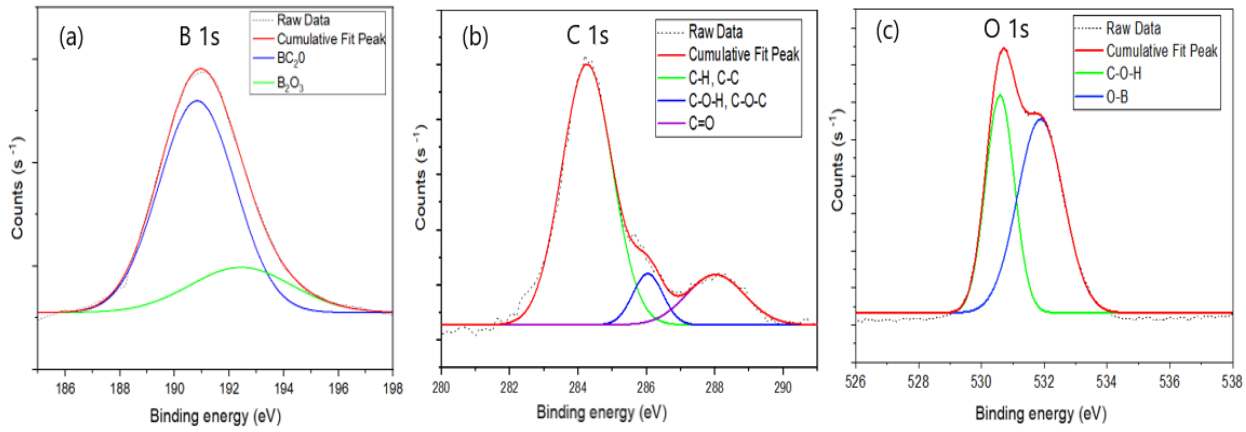

Figure 4.1: XPS spectra of BC:H thin film deposited at room temperature displaying (a) B 1s, (b) C 1s, and (c) O 1s peaks.

The elemental content of boron and carbon obtained from the XPS results is shown in Figure 4.2. The films evidently demonstrate carbon enriched a-B_xC_y:H composition. It can be observed that an increase in deposition temperature resulted in higher elemental C content in the films. This was accompanied by a decrease in B/C ratio. With the increase in substrate temperature, C-C bonds dramatically increase due to structural modifications and atomic ordering changes in the films. C elemental composition tends to increase due to the dissociation process of remained hydrocarbides [122, 123]. Such bond formations can be explained by means of the Frenklash and Spear model, which illustrates that the breaking of C-H bonds produces new C-C bonds [124]. According to the Frenklash and Spear model, the dissociation of C-H bonds to produce new C-C bonds can be expressed as follows [125]:

$C\text{-}H + C\text{-}H \rightarrow C\text{-}C + H_2$

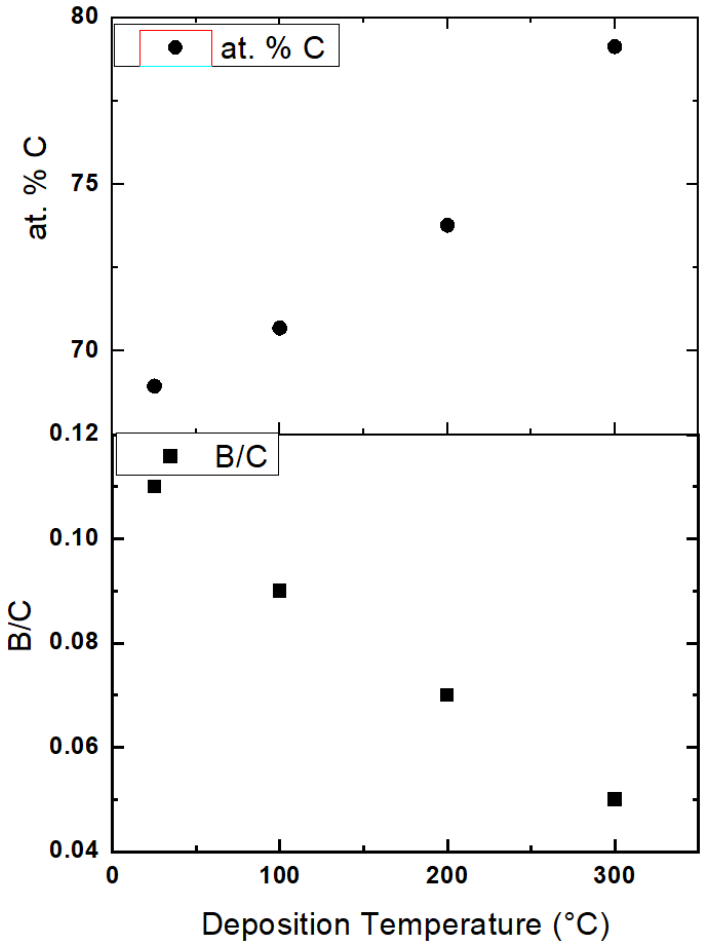

Figure 4.2: Atomic percentage of C and corresponding variation in B/C elemental ratio with deposition temperature.

A similar trend of increasing C content and a corresponding reduction in B/C ratio with deposition temperature is reported for boron carbide films deposited using various techniques [122, 126, 127]. The XPS results corroborate the high oxygen content in these films. It can be predicted that the relatively higher oxygen content could have originated due to the lower density of films and post-growth exposure to atmospheric conditions.

4.1.1 (b) Hydrogen Detection using REELS

REELS was used to examine the presence of hydrogen in boron carbide thin films as XPS cannot detect hydrogen. REELS spectra are shown in Figure 4.3.

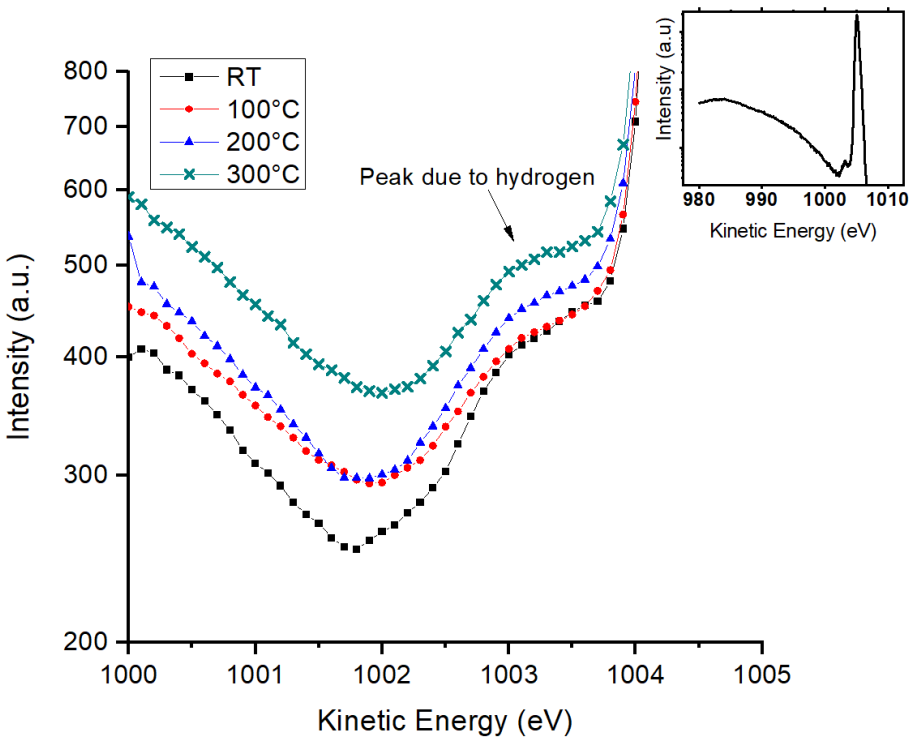

Figure 4.3: REELS spectra for a-BC:H films deposited at different substrate temperatures displaying the peak due to the presence of hydrogen atoms at 1003.5 eV. The inset figure is the complete REELS scan from 980-1010 eV for the film deposited at 300 °C.

The large peak observed at 1004 eV is due to the elastic scattering of electrons. The distinct shoulder peak observed at 1003.5 eV is attributed to elastic scattering collisions with hydrogen atoms. As hydrogen has the lowest atomic number, it facilitates reduction in total mass density and is also known to reduce the dielectric constant of the films [20]. The inset figure shows the

complete scan measured over 980-1010 eV kinetic energy for the film deposited at 300°C. H_2Ar gas used for these depositions consists of only 3% hydrogen in 97% argon. As the total hydrogen concentration in the films is estimated to be less than 10%, it was challenging to quantify the atomic hydrogen content in the films.

4.1.2 Electrical Characterization

Dielectric constant values of a-BC:H films were measured from the C-V characterization of MIM devices. Figure 4.4 shows the dielectric values as a function of substrate temperature. It is interesting to note that the dielectric values exhibited a decreasing trend with substrate temperature. The dielectric constant of pure boron carbide thin films lies between 4.8 and 8 [31]. The hydrogenated boron carbide films deposited in this study exhibited dielectric values between 6.5 and 3.5. The film deposited at 300°C, which incorporated maximum sp^2 carbon content and lowest B/C ratio as seen from XPS, and the highest amount of hydrogen concentration as revealed from REELS also displayed the lowest dielectric value of 3.5. Reduction in dielectric value is correlated with the highest C content in the films, which is favorable in reducing total film density. The lower the film density, the higher is the free volume within the films, which is an effective way of reducing dielectric constant values of materials. The presence of hydrogen also enhances the film porosity, which further reduces the dielectric constant of materials [128, 129]. In this study, higher C content and presence of hydrogen contributed collectively towards the decrease in the dielectric constant value of a-BC:H thin films. The range of dielectric values obtained for a-

BC:H in this study using RF magnetron sputtering is consistent with previously reported values for a-BC:H films synthesized using PECVD [20, 130].

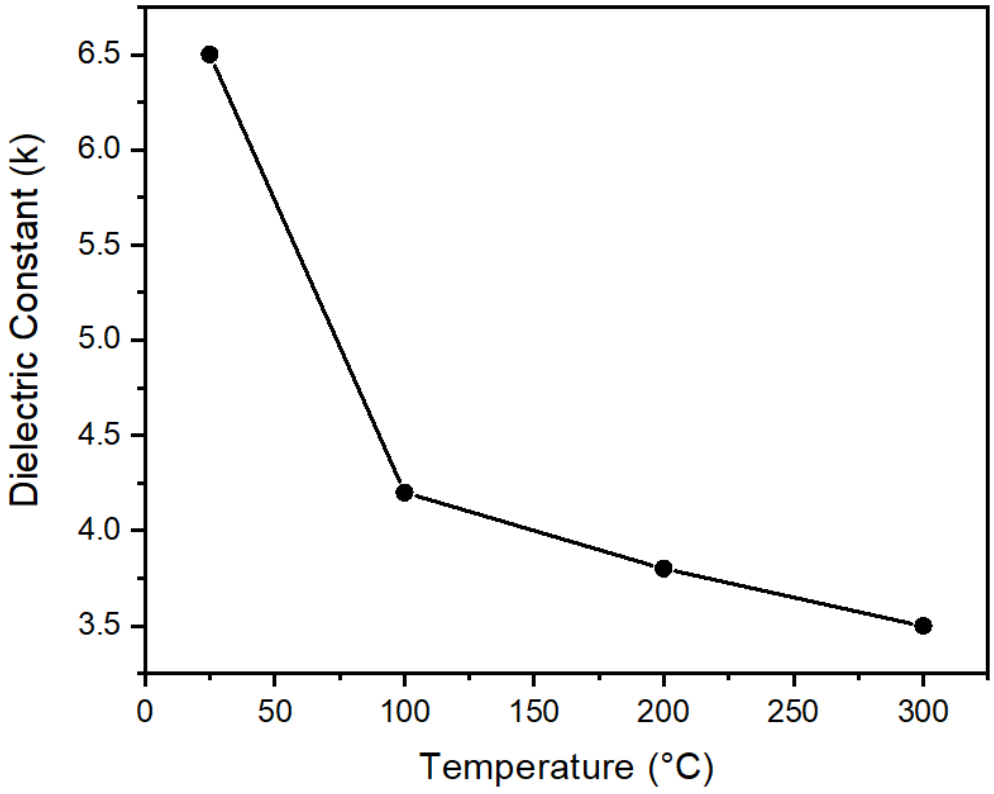

Figure 4.4: Dielectric values of a-BC:H thin films with varying substrate temperature.

Figure 4.5 shows the electrical resistivity trend of RF magnetron sputtered a-BC:H thin films as a function of substrate temperature. The electrical resistivity of a-BC:H thin films varied in magnitude of 10^9 Ω-cm for the film deposited at RT to 10^8 Ω-cm for the film deposited at 300°C. Pure boron carbide films grown in argon ambiance are reported to exhibit resistivity in the order of 10^9 Ω-cm at RT [131]. Amorphous hydrogenated boron carbide thin films investigated in this study demonstrated one order lower resistivity values at deposition temperatures of 100°C,

200°C, and 300°C. As C content was highest in the films deposited at 300°C, it can be established that an increase in C content with substrate temperature resulted in reduced electrical resistivity. An increase in sp^2 carbon content influences changes in carbon hybridization, which in turn affects the number of free electrons in the films and thus influences the resistivity values [132]. Similar trends of decreasing electrical resistivity due to higher C elemental content has been reported in boron carbide films [133].

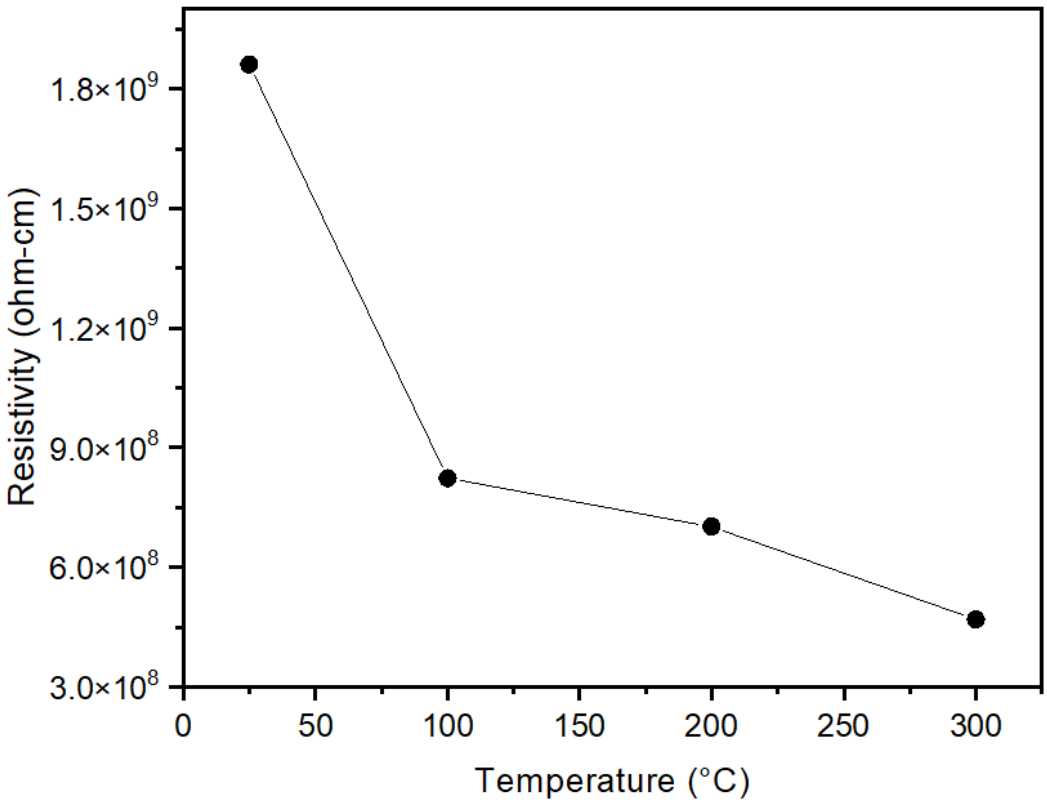

Figure 4.5: Electrical resistivity trend of a-BC:H thin films as a function of substrate temperature.

4.1.3 Optical Characterization

Optical characterization of a-BC:H thin films was performed by measuring transmission values in the visible light spectrum. Figure 4.6 shows the transmission values obtained over a wavelength range of 200 – 800 nm. All the films deposited in this study exhibited transmission values between 75-82% in the visible region, which are highly desired for applications in optical devices. It can be observed that films deposited at substrate temperature higher than RT demonstrated higher transmission values.

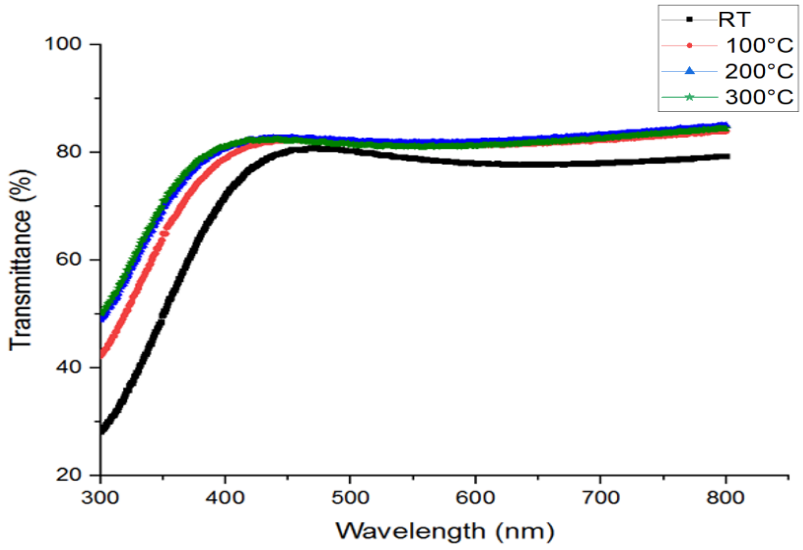

Figure 4.6: Optical transmission values of a-BC:H thin films deposited at varying substrate temperature.

Optical bandgap values of a-BC:H thin films were calculated from the measured transmission (%T) data. Figure 4.7 shows the Tauc plot used to extrapolate Eg. The n value on the y-axis was defined as 2, which is typically a standard value used for amorphous films. The optical bandgap for the films was estimated by extrapolating the linear region of curves to the energy axis.

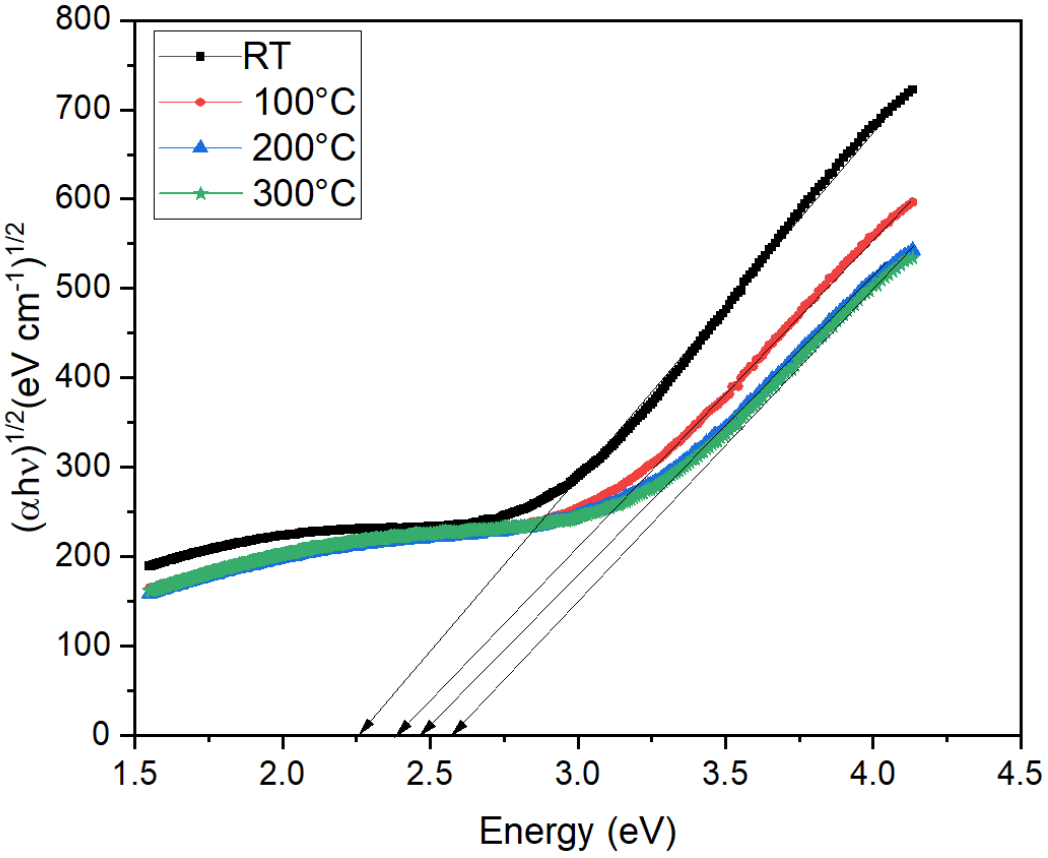

Figure 4.7: Extrapolating the linear region of Tauc plot to obtain bandgap values of a-BC:H thin films deposited at varying substrate temperatures.

Table 4.1 shows the bandgap values obtained from the Tauc plot. The optical bandgap varied slightly from 2.25 eV to 2.6 eV with an increase in substrate temperature. As seen from previous sections, which demonstrated surface characterization, films displayed hydrogen-rich nature with an increase in substrate temperature. This suggests that higher hydrogen content in the films with substrate temperature resulted in higher bandgap values in the thin films. A similar correlation between hydrogen concentration and bandgap values is reported for other dielectric materials such as a-SiC:H [134], a-Si:H [135], and a-C:H [136]. The E_g values obtained for a-BC:H

thin films deposited by RF magnetron sputtering in this study are analogous to E_g values of a-BC:H films synthesized by PECVD [20].

Table 4.1: Optical bandgap values of a-BC:H thin films.

Deposition Temperature (°C)	Optical Bandgap (eV)
RT	2.25
100	2.4
200	2.49
300	2.6

4.2 3% Hydrogenated BCN Thin Films For Mechanical and Photoluminescence Studies

4.2.1 Surface Characterization

4.2.1 (a) Energy Dispersive Spectroscopy

The elemental composition of BCN:H thin films deposited in this study were examined using EDS. EDS confirmed the presence of boron, carbon, nitrogen, and oxygen in the films. Film composition significantly depends on the deposition conditions, as shown in Figure 4.8 a-b. Referring to figure 4.8 (a), an initial increase in the hydrogen gas flow ratio caused a slight reduction in elemental boron content in the film. The boron content reduced from 10 at a gas flow ratio of 0 to 6 at a gas flow ratio of 0.6. However, further increase in gas flow ratio increased the boron content in the films dramatically to 15% at a gas flow ratio of 0.8 and 33.4% at a ratio of 1.

Similarly, the nitrogen composition in thin films also displayed drastic changes with varying gas. For film deposited at gas flow ratio of 0, the nitrogen content in the films is highest at 35%. As expected, the nitrogen content is highest when only reactive nitrogen sputtering was used to deposit film. An increase in hydrogen gas subsequently reduced the nitrogen content to ~15% for gas flow ratios of 0.2, 0.4, 0.6, and 1, except $H_2Ar/(H_2Ar + N_2)$ ratio of 0.8, where nitrogen composition was higher at 25%. This value is still lower than the nitrogen content reported in pure BCN film for gas ratio $H_2Ar/(H_2Ar + N_2) = 0$, as anticipated. It is interesting to observe that the carbon composition in films deposited at different gas flow ratios did not show significant variation. EDS recorded high oxygen content in the films. Reduction in oxygen content as gas flow $H_2Ar/(H_2Ar + N_2) = 1$ is compensated by a corresponding increase in boron content. The presence of oxygen may be associated with the post-processing of the samples in atmospheric conditions. There is evidence of BCN films deposited in the presence of hydrogen gas reporting a large amount of oxygen content in the films due to low porosity [55].

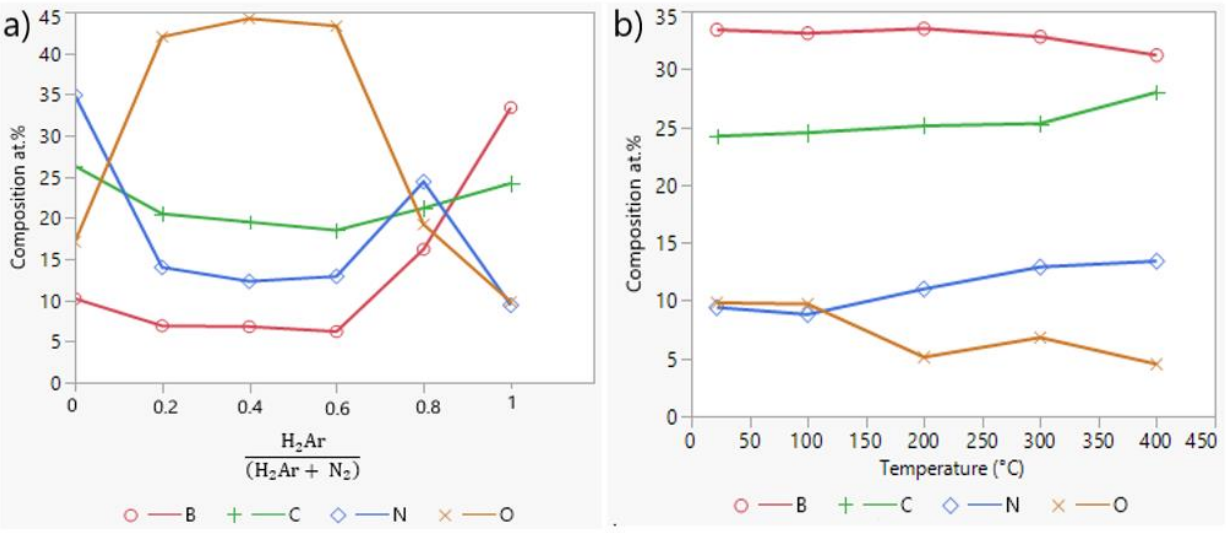

Figure 4.8: EDS elemental composition data for films deposited with (a) varying hydrogen gas flow ratios and (b) varying substrate temperature.

Figure 4.8 (b) shows the elemental composition of films deposited at constant gas flow $H_2Ar/(H_2Ar + N_2)$ ratio of 1 and different substrate temperatures. Thin-film elemental composition displayed a very different relationship with substrate temperature. An increase in temperature did not alter the boron content up to 300°C. At deposition temperature of 400°C, the boron content was observed to marginally reduce from 34% to 31%. On the contrary, carbon and nitrogen displayed an exact opposite behavior with temperature. Carbon content gradually increased from RT to 300°C and displayed a sudden rise to 29% at 400°C. Likewise, nitrogen content also gradually increased from 10% at RT to 15% at 400°C. It can be noted that oxygen content remained relatively low when BCN films were deposited at higher substrate temperatures. EDS measurements reported in figure 4.8 a-b did not account for hydrogen concentration in the films.

4.2.1 (b) Fourier Transform Infrared Spectroscopy

The chemical bonding and presence of hydrogen in the films were evaluated from FTIR analysis. Films deposited as a function of varying gas flow ratios demonstrated high oxygen content. As a result, further clarification on functional groups was performed. Figure 4.9 shows the FTIR transmittance spectra of as-deposited films with varying gas flow $H_2Ar/(H_2Ar + N_2)$ ratios of 0 to 1 corresponding to films A-F, respectively. Film A corresponds to $H_2Ar/(H_2Ar + N_2)=0$, film B corresponds to $H_2Ar/(H_2Ar + N_2)= 0.2$ and so on. Refer to Table 3.1 for additional clarification.

Transmittance peaks were mainly observed at 2360, 2170, 2100, and 750 cm^{-1}. The peak at 2360 cm^{-1} is attributed to C=O bonding in the films [137]. Thus, it can be concluded that the oxygen content observed in EDS is corroborated in FTIR, and oxygen in the films seems to bond with carbon atoms.

The peak observed at 2170 cm^{-1} is associated with C≡N and B-H structure in the films. This peak is very distinct for Film A, which is the pure BCN film. With increase in hydrogen gas ratio, it can be observed that the peak at 2170 cm^{-1} gradually decreases for films B to E, and tends to cease for film F. Disappearance of this peak indicates phase transitions in the film with varying gas ratio and is consistent with previous reports [74]. The broad peak at 2100 cm^{-1} is attributed to the presence of C-N in the films [62]. Although film A exhibited a clear and sharp C-N peak, the peak intensity was observed to reduce with the hydrogen gas ratio. Based on this interpretation, it may be implied that pure BCN film primarily demonstrates strong C-N bonding, which undergoes changes with varying gas ratios. The narrow absorption peak just below 200 cm^{-1} is possibly due to the presence of residual CO_2 gas in the FTIR spectrometer. The broad band stretching from 500-1000 cm^{-1} with a clear peak at 750 cm^{-1} is assigned to out-of-plane sp^2 bonded B-N-B bending mode [35, 138]. FTIR transmittance spectra did not show any evidence of N-H and O-H bonding in the films.

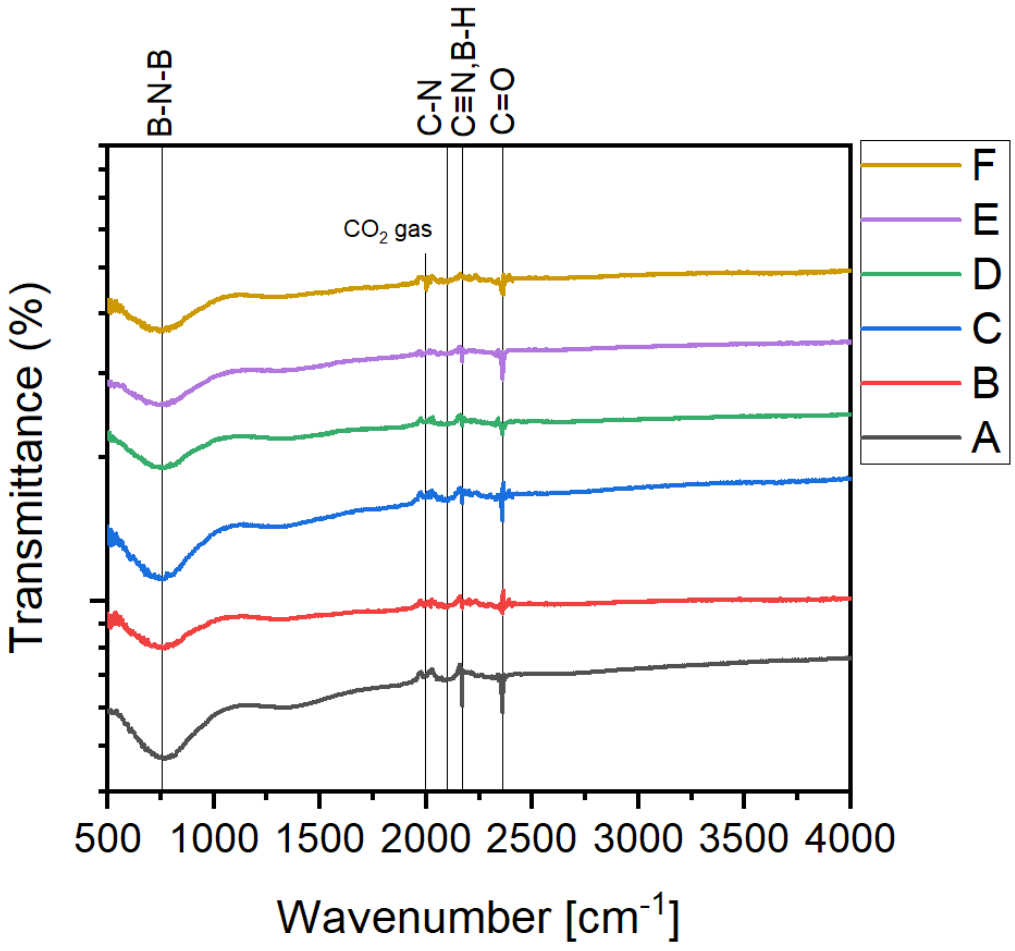

Figure 4.9: FTIR transmittance spectra of BCN:H thin films deposited at varying gas flow ratios.

4.2.2 Mechanical Properties- Hardness and Young's Modulus

The influence of hydrogen gas and substrate temperature on mechanical properties of BCN thin films was investigated using nanoindentation studies. Figure 4.10 a-b shows the trend in mechanical properties with varying gas flow ratios and substrate temperatures, respectively. Young's modulus for pure BCN film was 134 GPa. An increase in $H_2Ar/(H_2Ar + N_2)$ ratio from 0 to 0.2 increased Young's modulus to 140 GPa. However, further increase in hydrogen gas flow

reduced Young's modulus to 126 GPa. For gas ratios higher than 0.6, Young's modulus showed a slightly increasing trend. Overall, Young's modulus was observed to show a reducing trend with hydrogen gas. Changes in hybridization when H atoms bond with B/C/N can be regarded as a reason for the reduction in Young's modulus [139, 140]. As a function of temperature, Young's modulus followed an increasing trend beyond 200°C by exhibiting values from 125 GPa to 140 GPa. The highest value of 140 GPa was recorded for BCN:H film deposited at 400°C.

Hardness values of BCN:H thin films decreased for gas ratios of 0, 0.2, and 0.4 from 15 GPa to 12 GPa to 6 GPa, respectively. BCN:H films deposited at gas ratio of 0.6 exhibited the lowest hardness of 6 GPa in this study. It is interesting to observe that the hardness value increased from 6 GPa to 18 GPa for higher gas ratios of 0.8 and 1. This increase in hardness is stemmed due to the phase transitions in the films with varying gas ratios, as revealed in FTIR above. BCN:H thin films exhibited excellent hardness values as a function of substrate deposition temperature. Hardness values increased linearly from 18 GPa for the film deposited at RT to 23 GPa for the film deposited at 400°C. It is noteworthy that enhancement in hardness values achieved for films deposited with variation in substrate deposition temperature (22 GPa at 400°C) is superior to maximum hardness achieved for films deposited by varying gas (18 GPa for gas ratio 1). Films deposited at higher substrate temperature acquired higher carbon and nitrogen content, as seen from EDS. Thus, enhancement in hardness can be attributed to characteristic "hard" C-N phases in the films [141]. Although literature reports hydrogenation of low dielectric materials deteriorates the mechanical strength due to increased porosity, BCN:H films deposited in this

study exhibited distinguished mechanical properties. At higher temperatures, the films exhibited excellent hardness as well as Young's modulus.

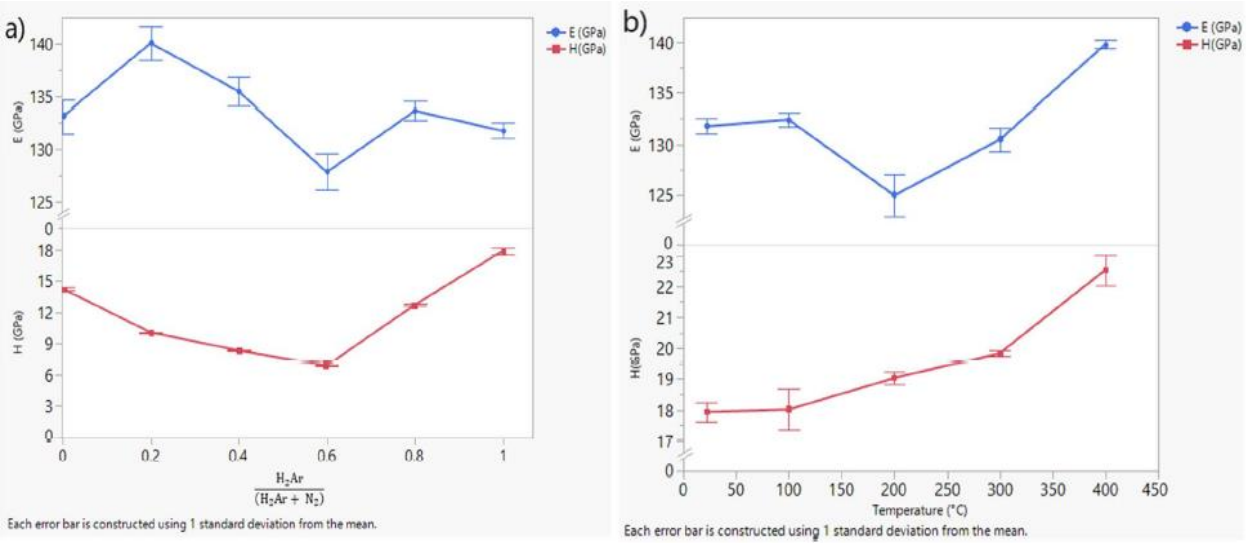

Figure 4.10: Young's modulus (E) and hardness (H) of BCN:H thin films deposited at varying (a) gas flow ratios of hydrogen to nitrogen and (b) substrate deposition temperature.

4.2.3 Photoluminescence Study

BCN:H thin films were examined at a single excitation wavelength of 365 nm for photoluminescence (PL) studies. Figure 4.11 shows PL spectra obtained for films deposited with varying gas ratios. All films exhibited two distinct PL peaks. Film A, which is pure BCN film (no hydrogen gas) displayed two low-intensity peaks at 490 nm (2.53 eV) and 591 nm (2.1 eV). BCN-based phosphors synthesized using different techniques have reported similar peaks in the past [86, 142, 143]. Films B, C, D, F, which are deposited at higher hydrogen gas ratios, demonstrated peak shifts to 499 nm and 602 nm along with sharper peak intensity. Film E ($H_2Ar/(H_2Ar + N_2)$ =

0.8) showcased the highest peak intensity compared to other films and a wider peak shift to 515 nm and 621 nm. The variation in deposition gas flow ratio impacted the film composition, which helped attain tunable films with PL peak shifts from 490 nm to 515 nm (green shift) and from 591 nm to 621 nm (red shift).

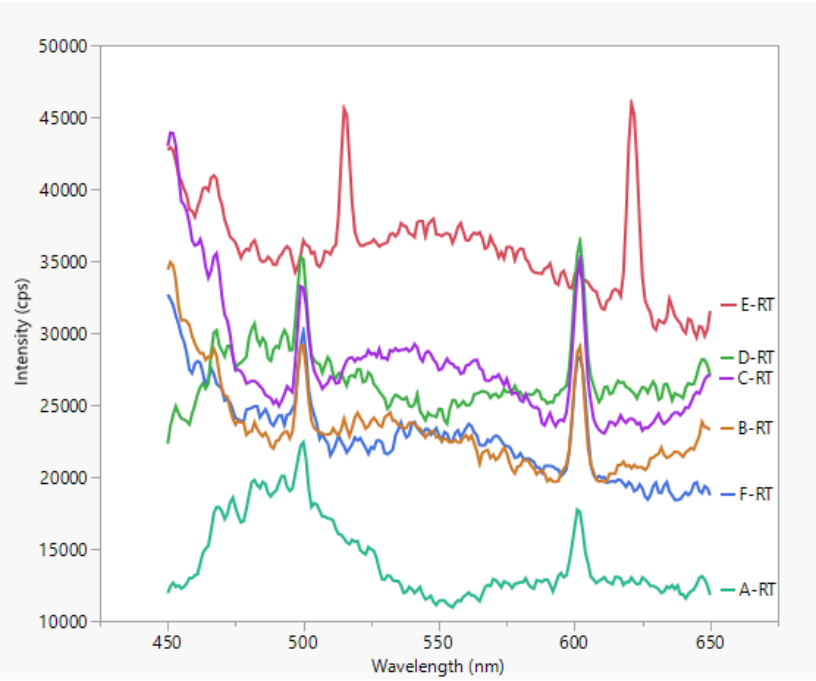

Figure 4.11: PL spectra of BCN:H thin films deposited with hydrogen-argon to nitrogen gas ratios of 0 to 1.

Figure 4.12 shows PL properties of BCN:H thin films deposited at different substrate deposition temperatures. Clear evidence of PL peak shifting to longer wavelengths was observed with temperature. Reference film F deposited at RT displayed two distinctive peaks at 490 nm and 591 nm. For the film G deposited at 100°C, the peaks shifted to 501 nm and 603 nm. Further increase in temperature caused the peaks to shift to 521 nm, and 627 nm for film H deposited at 200°C,

and 544 nm and 655 nm for the film deposited at 300 °C. As carbon content increased with temperature in the EDS analysis, this causes a reduction in bandgap, which explains the PL peak shifts to longer wavelengths [144]. Recently, BCN-based phosphor with a red emission peak up to 630 nm was reported [143]. However, BCN:H films in this study exhibited a sharp red emission peak up to 655 nm for the first time. The facile deposition technique and unique PL properties observed in this study make BCN:H thin films a candidate material for potential LEDs, optoelectronics, and bioimaging applications.

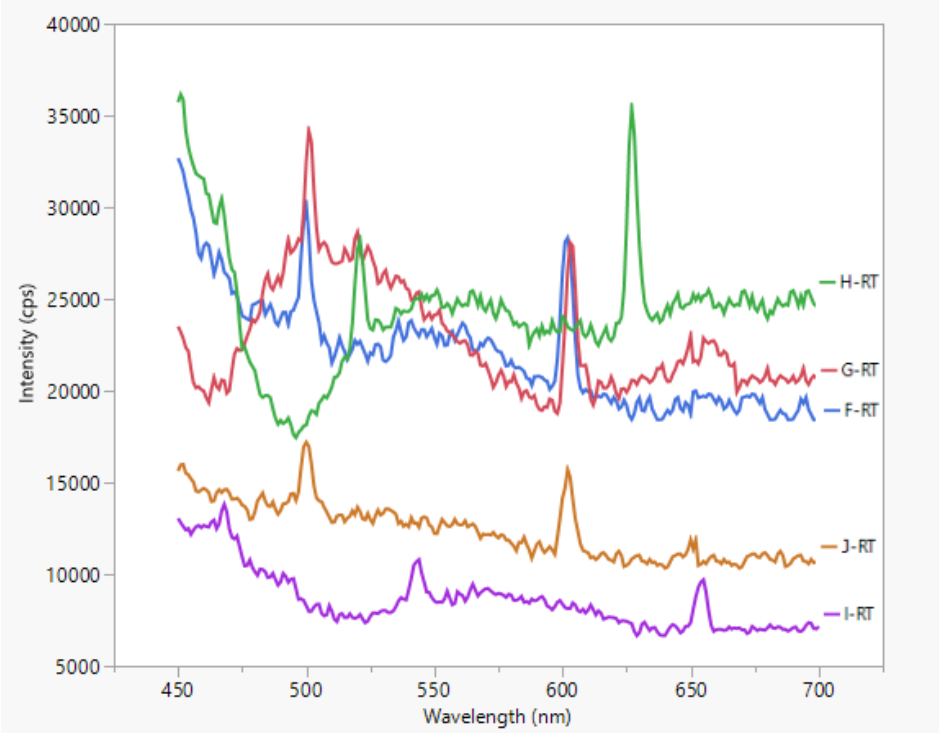

Figure 4.12: PL spectra of BCN:H thin films deposited at varying substrate temperature from room temperature to 400°C.

Another interesting observation was obtained from the PL spectra. Table 4.2 shows that the PL intensity tends to increase with hydrogen gas flow in the deposited films. Enhancement in PL peak intensity due to hydrogen gas is primarily due to the saturation of non-radiative recombination sites in the materials, such as dangling bonds [145]. Films A, B, C, and D, E exhibited ~10,000 units higher PL peak intensity. As these films were deposited at a higher hydrogen gas ratio, the PL peak intensity enhancement implies hydrogen gas sensing by BCN:H thin films. With the current demand for clean energy alternatives for a clean future, hydrogen gas will be critical to developing sustainable energy sources. Utmost importance must be given to detect hydrogen leaks to avoid hazards. Unlike commercially used hydrogen gas sensing materials such as ZnO, NiO, SnO_2, Fe_2O_3, BCN can operate at room temperature, possess good mechanical properties, and can withstand harsh temperatures for extreme environments [146].

Table 4.2: PL peak details for films deposited at varying hydrogen gas flow and substrate temperature displaying peak shifts and different peak intensities.

Film	$H_2Ar/(H_2Ar + N_2$	Deposition Temperature (°C)	PL Peak 1 (nm)	Peak 1 Intensity	PL Peak 2 (nm)	Peak 2 Intensity	Bandgap 1 (eV)	Bandgap 2 (eV)
A	0	RT	490	19063	591	12521	2.53	2.1
B	0.2	RT	500	29163	602	29058	2.48	2.06
C	0.4	RT	499	33249	602	35114	2.48	2.06
D	0.6	RT	499	35260	602	36366	2.48	2.06
E	0.8	RT	515	45594	621	45965	2.41	1.99
F	1.0	RT	499	29155	602	28336	2.48	2.06
G	1.0	100	501	34166	603	28070	2.47	2.05
H	1.0	200	521	28248	627	35441	2.38	1.98
I	1.0	300	544	10802	655	9701	2.38	1.89
J	1.0	400	501	17569	602	16899	2.47	2.06

BCN:H thin films deposited by dual sputtering in this study exhibited a rare phenomenon of negative thermal quenching (NTQ) for the first time. Figure 4.13 shows the photoluminescence spectra of BCN:H thin films measured at RT and 77 K using the spectrofluorometer. Films B, C, D, and E exhibited the NTQ phenomenon. These films contain both hydrogen and nitrogen elemental concentrations. Film A or the pure BCN thin film did not show evidence of NTQ. Thermal quenching (TQ) observed in conventional semiconductors is related to decreased luminescence intensity with an increase in temperature. This mechanism originates due to the temperature-induced increase in the non-radiative recombination probability of PL emission. However, certain semiconductors showcase an opposite behavior of increasing luminescence intensity with temperature, termed at NTQ. The NTQ phenomenon is commonly observed in materials like ZnO, ZnS, and GaAs [147, 148]. The model proposed by Shibata et al. explains the TQ and NTQ phenomenon in semiconductors [149]. Consider a material with only two states- initial state and final state. If the energy separation between these two states is larger than the system temperature, then the thermal excitation of electrons from the final to the initial state is considered to be negligible. Nevertheless, materials can obtain multiple states between the initial and final states. For material with multiple states, the energy separation between states is comparable to the system temperature, and hence the thermal excitation between the states is not negligible. As a result, an increase in temperature corresponds to an increase in luminescence intensity.

Since only the films containing both hydrogen and nitrogen doping exhibited NTQ, this emission can be attributed to radiation recombination through states related to H and N atoms. In the B-

C-N ternary triangle, two-dimensional carbon and graphene have been reported to exhibit NTQ phenomenon [150]. BCN:H thin films deposited in this study demonstrating NTQ phenomenon are promising for selective and tunable optical emitters in the visible region, making them candidate materials for biomarkers and optical thermometry applications.

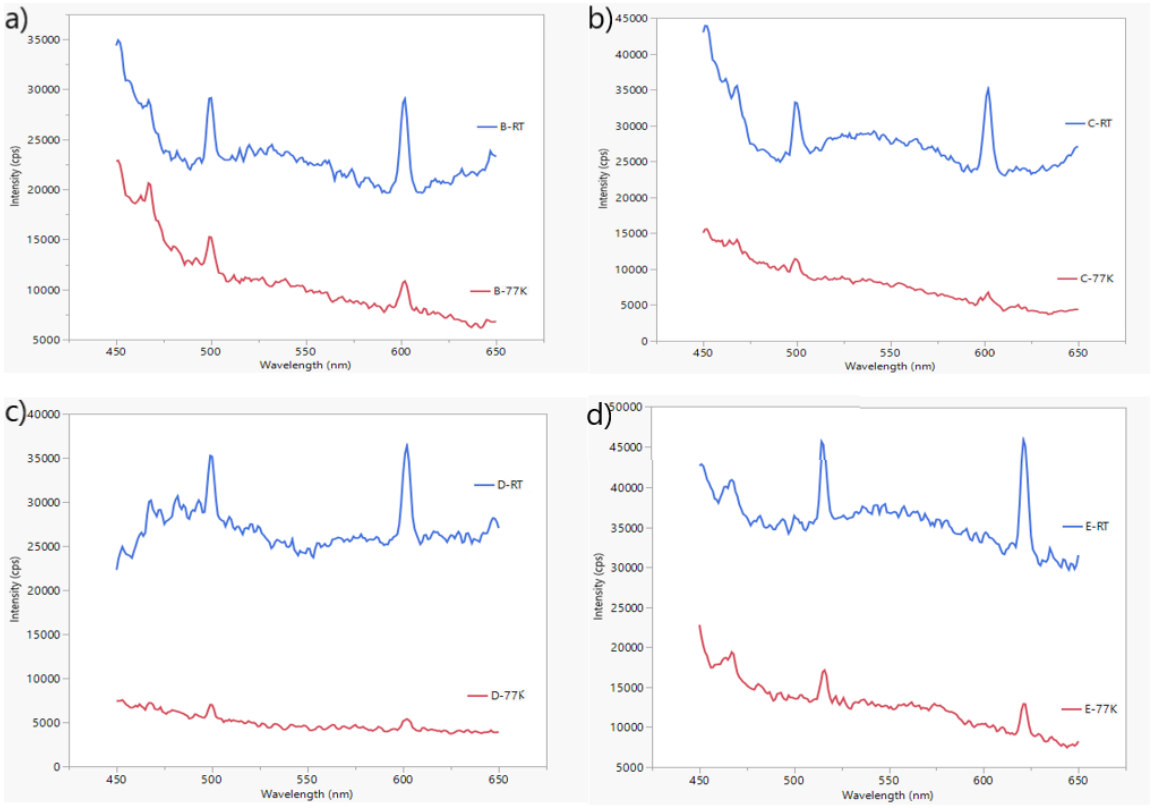

Figure 4.13: PL spectra of (a) film B, (b) film C, (c) film D, and (d) film E exhibiting the rare phenomenon of negative thermal quenching.

4.3 99.99% Hydrogenated BCN Thin Films

4.3.1 Surface Characterization

4.3.1 (a) X-ray Photoelectron Spectroscopy

Surface characterization was performed on BCN and BCN:H thin films deposited on dual side polished Si wafers. The thickness of the films deposited in this study ranged between 1500 – 2500 Å. XPS studies were performed to analyze the elemental composition and chemical bonding of the deposited BCN thin films. Table 4.3 shows the elemental composition of film achieved using XPS.

Table 4.3: Elemental composition of B, C and N atoms in the films with different hydrogen gas flow.

Film	% B	% C	% N
BCN	29	34	33
BCN:H10	30	34	30
BCN:H20	31	35	29
BCN:H30	28	40	27
BCN:H40	28	42	25
BCN:H50	32	44	18

Pure BCN thin films displayed B atomic concentration of 29%, C atomic concentration of 34%, and N atomic concentration of 33%. This film was deposited using dual-target sputtering in the presence of N_2 and Ar. The elemental carbon concentration increased with hydrogen gas flow. This increase was compensated by the reduction of nitrogen content. This elemental composition behavior corroborates with the gas flow used, as an increase in hydrogen gas was achieved by

reducing the nitrogen gas in the deposition chamber. Boron content remained relatively constant with hydrogen process gas variation. Figure 4.14, 4.15 and 4.16 shows the XPS narrow scan spectra of B1s, C1s and N1s, respectively for films deposited with varying H_2/N_2 gas ratios.

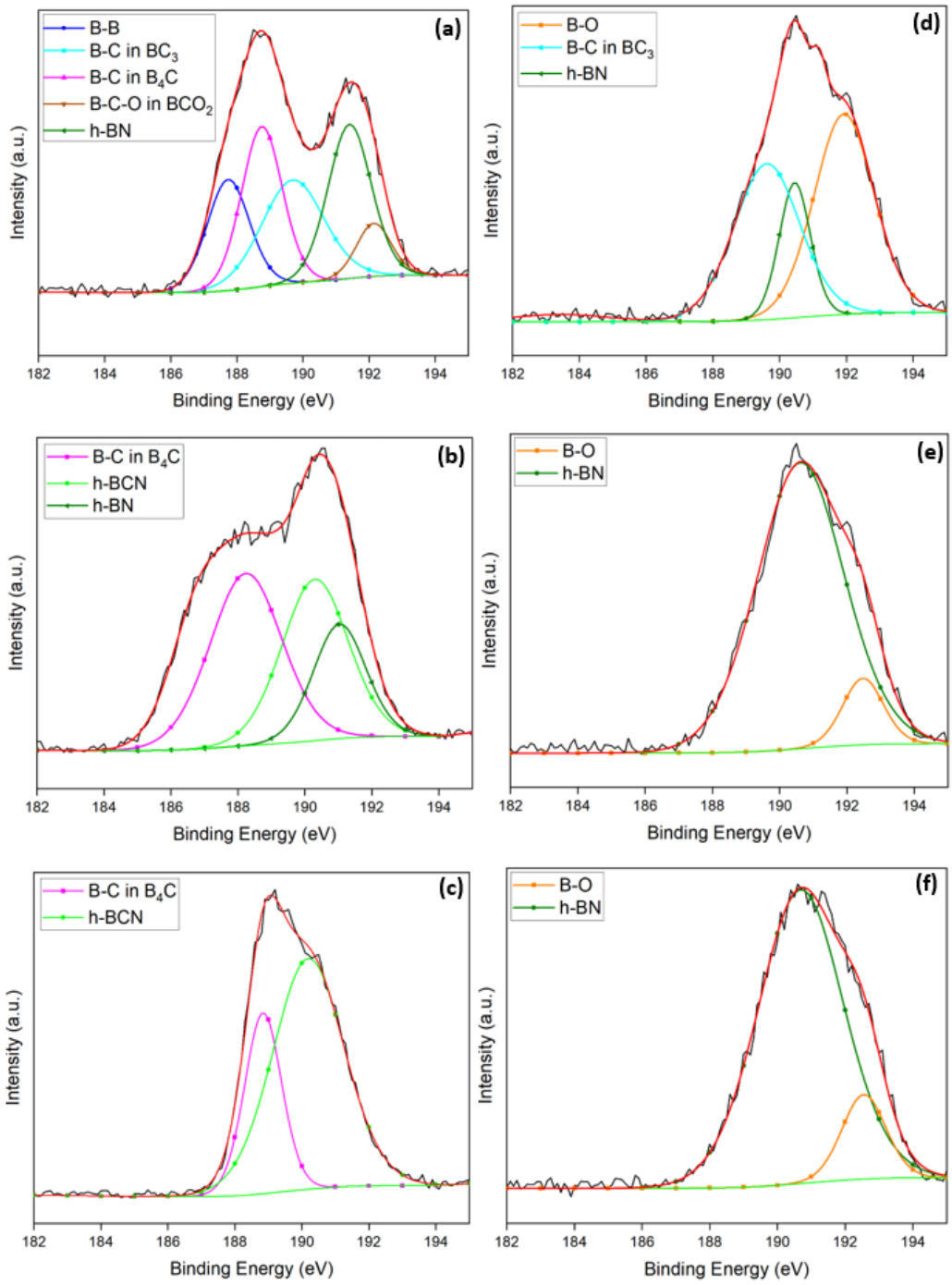

Figure 4.14: XPS spectra of B1s scans for (a) BCN, (b) BCN:H10, (c) BCN:H20, (d) BCN:H30, (e) BCN:H40, and (f) BCN:H50.

The B1s, C1s and N1s spectra are broad and asymmetric, thus suggesting that there is more than one type of bonding scheme present between the elements in the thin films. The B1s spectra shown in figure 4.14 were deconvoluted into multiple peaks located at 187.7 eV, 188.7 eV, 189.6 eV, 190 eV, 190.6 eV, and 192 eV. The peak at 187.7 eV is attributed to B-B bonds in the films [151]. The lower energy peaks located at 188.7 eV are attributed to B-C bonding in the B_4C structure [152, 153]. A prominent shoulder peak at ~189.6 eV indicated the contribution of sp^2 B-C hybridization in BC_3 structure frequently reported in the literature [30]. B-N bonds in hexagonal boron nitride were represented by peak centered at 190 eV [154]. The h-BCN peak position is commonly reported to fluctuate between 188 – 191.5 eV due to film elemental composition changes [155]. As a result, the peak located at 190.6 eV was attributed to h-BCN bonding. As boron is oxidation sensitive element, typically oxide-related species in the B1s spectra are observed at ~192 eV. Hence, the peaks centered at 192.1 eV implied the formation of B-C-O bonding in the BCO_2 structure [156]. The peaks appearing at ~192.5 eV are attributed to the B-O bonds [156]. The XPS results confirmed that B atoms chemically bond with C and N atoms resulting in the B-C-N hybridization of films.

Figure 4.15 shows the C1s spectra for BCN and BCN:H thin films. The C1s spectra were deconvoluted into multiple peaks located at 282.5 eV, 282.8 eV, 284 eV, 285.7 eV, 286.8 eV, 287 eV and 288 eV. The dominant peak centered at ~282.8 and ~284 eV originates due to contributions from C-B and C-C/C-H bonds, respectively [61, 157, 158]. It can be observed that the C-C/C-H peak shifted to a higher energy level from 284 eV and 285 eV as the film composition changed from BCN to BCN:H. The C1s peak shift to higher energy levels is due to the higher

concentration of C as seen from XPS elemental composition analysis and more contribution from the C-H bonds. With the introduction of hydrogen in the BCN network, the C-C/C-H peak exhibited narrow intensity for BCN:H10 and BCN:H20 films, as shown in figure 4.15 b-c. However, with increase in hydrogen gas flow, the C-C/C-H peak intensity increased gradually for BCN:H30, BCN:H40 and BCN:H50 thin films. BCN:H50 exhibited the sharpest intensity of C-C/C-H peak as shown in figure 4.15 f, thus implying a larger number of C-C/C-H bond formation in the films with higher hydrogen gas flow. An apparent shoulder peak at 282.5 eV is attributed to C-B bonds consistently reported for B_4C thin films in the literature [138, 159]. Distinctive peaks fitted at 285.7, 286.8 and 287 eV are identified as C-N, sp^2 trigonal C-N, and sp^3 tetrahedral C-N bonds, respectively [26, 159, 160]. Some oxidation contamination was observed at a binding energy of 288 eV, which is associated with C=O bonds [152].

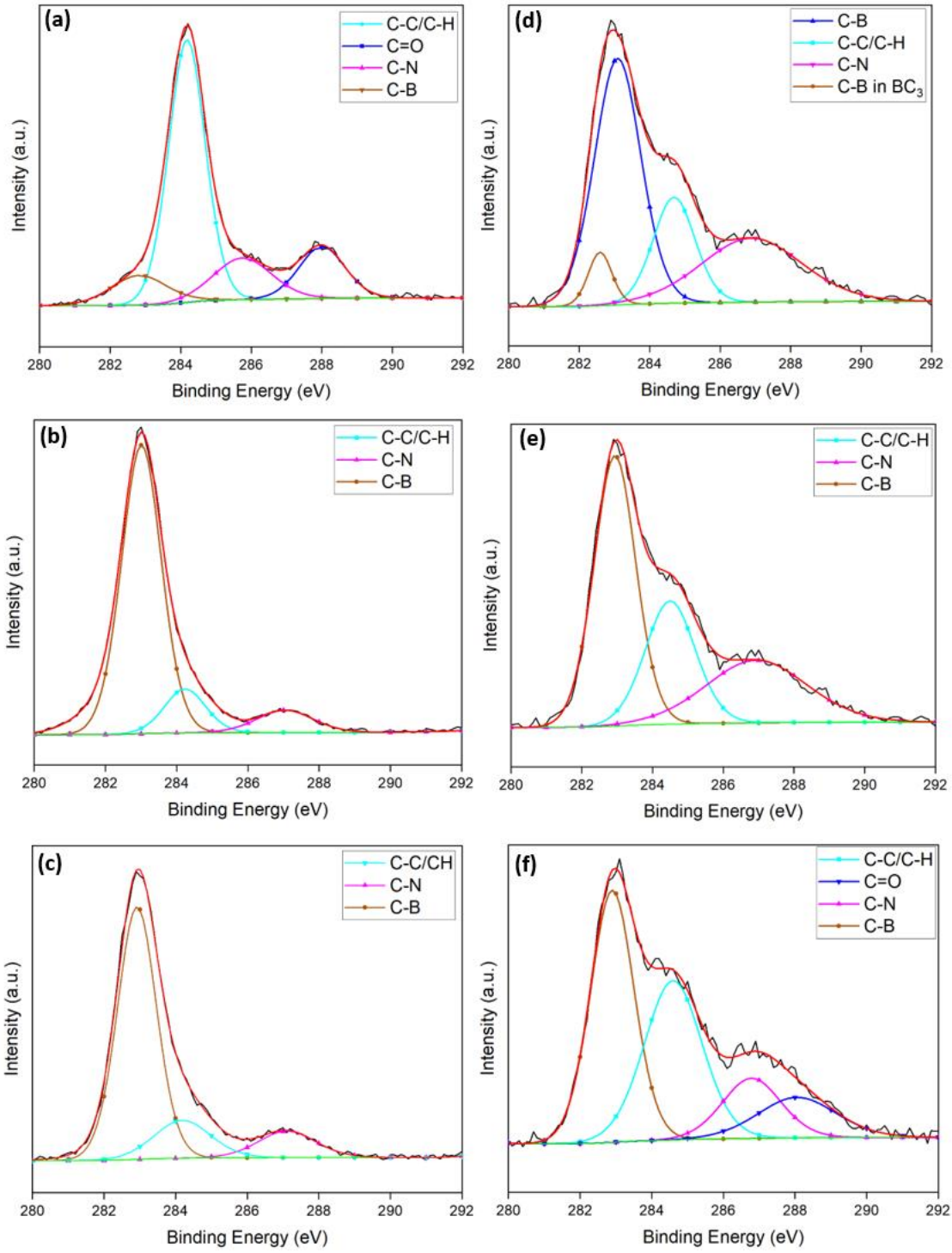

Figure 4.15: XPS spectra of C1s scans for (a) BCN, (b) BCN:H10, (c) BCN:H20, (d) BCN:H30, (e) BCN:H40, and (f) BCN:H50.

The N1s spectra shown in figure 4.16 confirmed the interpretation of chemical bonding observed in B1s and C1s spectra of BCN and BCN:H thin films. The N1s spectra were deconvoluted into peaks centered at 396.4, 397.9 – 398.05, 398.3, and 399.7 eV. The deconvoluted peak located at 393.4 eV is associated with the N-B bonds. Due to the difference in peak positions with varying elemental composition, the peaK around 397.9 – 398.05 eV is typical characteristic of sp^3 N-C binding energy [161]. The peak observed at 398.3 eV is attributed to sp^2 N-B bonding as per reports in the literature [61]. Finally, the peak at 399.7 eV observed only for BCN and BCN:H thin films in figure 4.16 a-b is associated with $N\text{-}C_3$ bonding [61]. This peak tends to disappear for BCN:H20, BCN:H30, BCN:H40 and BCN:H50. It can be concluded that the carbon elements which were binding with nitrogen now readily form hydrocarbons as the nitrogen in the film is replaced by hydrogen.

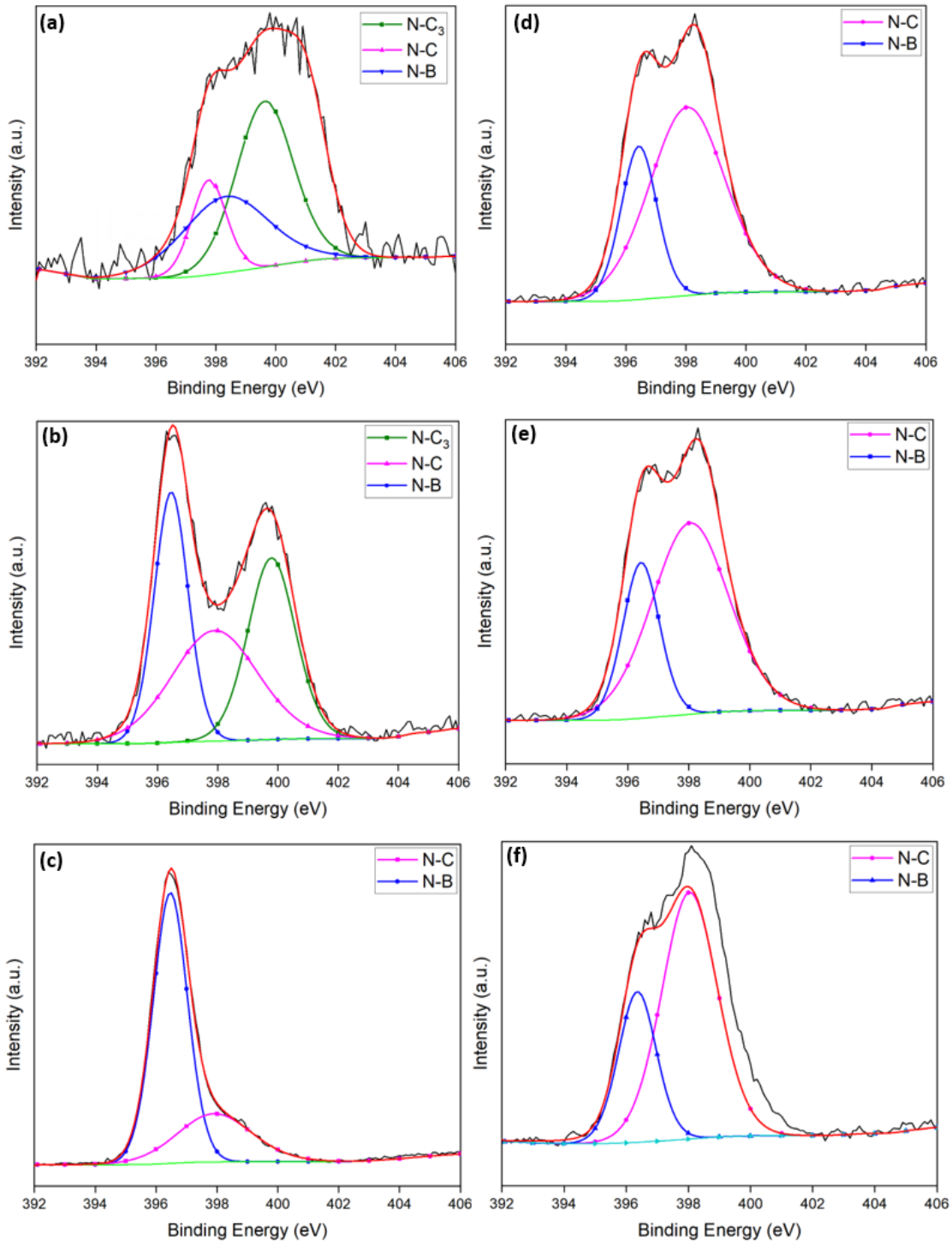

Figure 4.16: XPS spectra of N1s scans for (a) BCN, (b) BCN:H10, (c) BCN:H20, (d) BCN:H30, (e) BCN:H40, and (f) BCN:H50.

4.3.1 (b) Fourier Transform Infrared Spectroscopy

FTIR transmittance was performed at room temperature to recognize the functional groups present in the films and confirm hydrogen doping. Background correction from the reference substrate of dual side polished Si was performed on all spectra. Figure 4.17 shows the FTIR transmittance spectra of BCN, BCN:H20 and BCN:H50 thin films. The transmittance spectra of only these three films are displayed to observe the peaks and its intensity variation. The peak observed at 1380 cm^{-1} is attributed to an in-plane sp^2 B-N stretching bond [35, 162]. The peak at 2950 cm^{-1} originates due to the C-H stretching vibrations in the films [163]. As expected, pure BCN film did not exhibit a peak at 2950 cm^{-1}, whereas the hydrogen doped films of BCN:H20 and BCN:H50 displayed a distinctive peak belonging to C-H bonding. Thus, it can be concluded that hydrogen gas in the deposition chamber was successfully doped in the thin films. The hydrogen tends to bond only with carbon elements in the thin films. There was no evidence of B-H and N-H bonds.

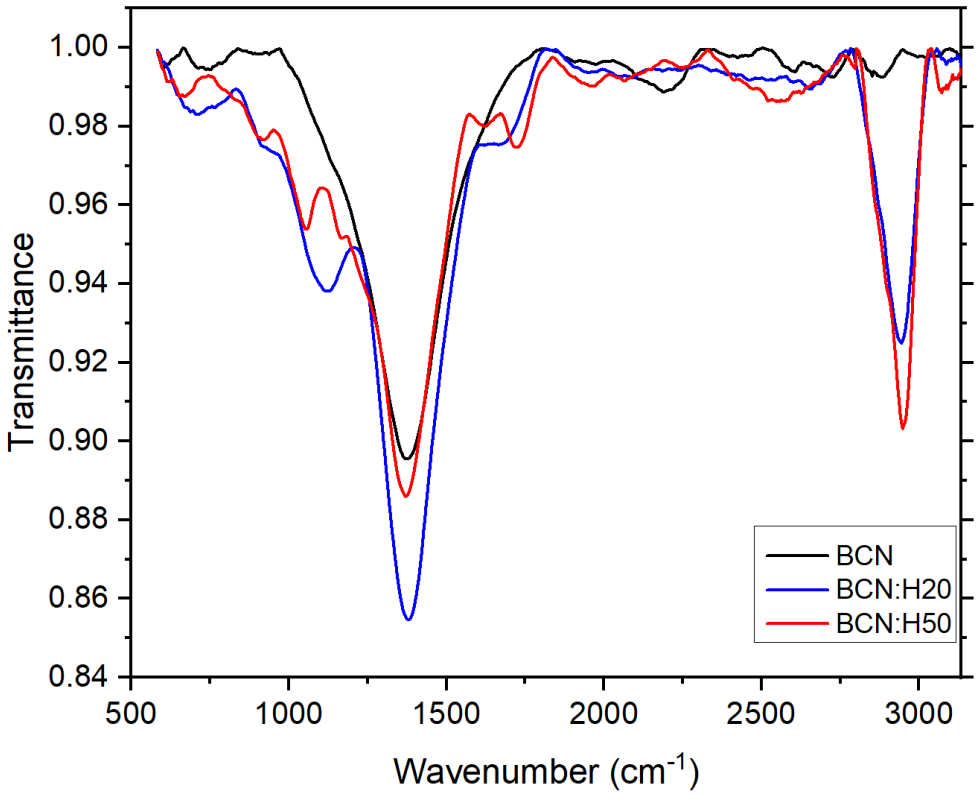

Figure 4.17: FTIR transmittance spectra of BCN and BCN:H thin films.

The absorption coefficient was plotted for the C-H peak from the FTIR transmittance spectra to quantify the hydrogen concentration in the films. The absorption coefficient (α) was calculated in the range of 2500-3200 cm^{-1} using:

$$\alpha = \frac{\ln(\frac{1}{T})}{d}$$

where T is the % transmittance, and d is the thickness of the film. Figure 4.18 shows the absorption coefficient of BCN and all BCN:H thin films deposited in this study.

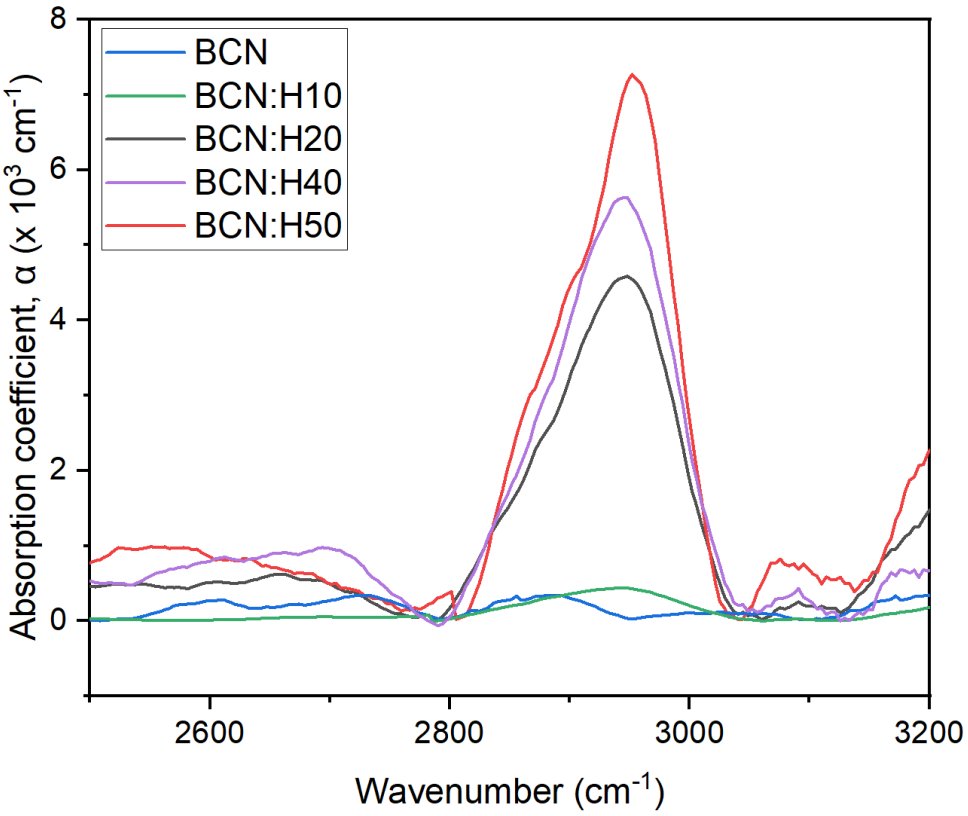

Figure 4.18: The absorption coefficient of C-H band for BCN and BCN:H thin films.

The concentration of H bonded with C was determined by integrating the absorption coefficient peak of C-H bond. Figure 4.19 shows the integrated absorption coefficient of C-H bonds in the films. It can be observed that BCN film showed no peak, and hence the lowest area under the curve. BCN:H10 displays a small area under the peak due to less hydrogen gas used during deposition. The total area under the curve increased by a factor of 9, with an increase in hydrogen gas from 10% to 20%.

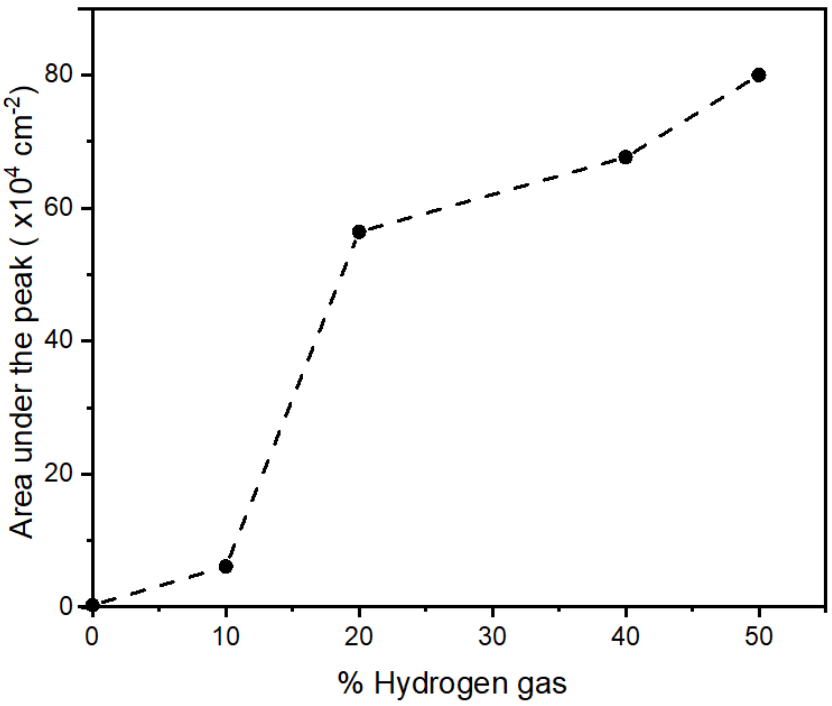

Figure 4.19: Area under the C-H peak corresponding to the concentration of C-H bonds in the films obtained by integrating the absorption coefficient.

With increasing H_2 concentration in the gas mixture, the integrated area of the IR absorption peak associated with C-H bonding increased. BCN:H50 demonstrated the sharpest absorbance peak intensity and largest area under the curve, thus implying a larger number of C-H formations. Hence, it can be concluded that with the increase in hydrogen gas flow, the number of C-H bonds in the film increased.

4.3.2 Electrical Properties

The dielectric constant (k) of BCN and BCN:H thin films were calculated as a function of the hydrogen gas incorporated during sputtering. Figure 4.20 shows the dielectric constant trend of

the deposited films. It can be observed that the dielectric constant followed a linearly decreasing trend with an increase in percentage hydrogen gas during sputtering. The dielectric constant of pure BCN films was 6.2. The k value reduced from 6.2 for pure BCN film with no hydrogen doping to 2 for BCN:H50. This reduction in the k value was associated with non-polar C-C and C-H bond formations, as confirmed from XPS and FTIR analysis. XPS verified that the C-C/C-H peak increased with a higher percentage of hydrogen gas. FTIR analysis corroborated this result by displaying a larger area under the absorption curve with an increasing percentage of hydrogen gas. Thus, a higher percentage of hydrogen gas resulted in a larger number of C-C and C-H bond formations in the deposited films.

The presence of non-polar bonds reduces the number of electric dipoles formed in the dielectric materials, thus reducing the polarization in the presence of an electric field [128, 164]. The dielectric constant of a material is a physical measure of electric polarization. Reducing polarization by means of non-polar bonds can thus reduce the dielectric value of films. A similar trend of decrease in the k value of dielectric thin film due to an increase in non-polar C-H bonds for BCN films deposited was reported by the PECVD technique [123, 165, 166]. The lowest dielectric constant value of 1.9 was recorded for BCN:H thin films synthesized using PECVD [29]. The lowest k value of 2 obtained in this study by RF magnetron sputtering is very close to k=1.9 achieved by PECVD. Additionally, RF magnetron sputtering does not demand toxic precursors and high-temperature synthesis required for the CVD technique.

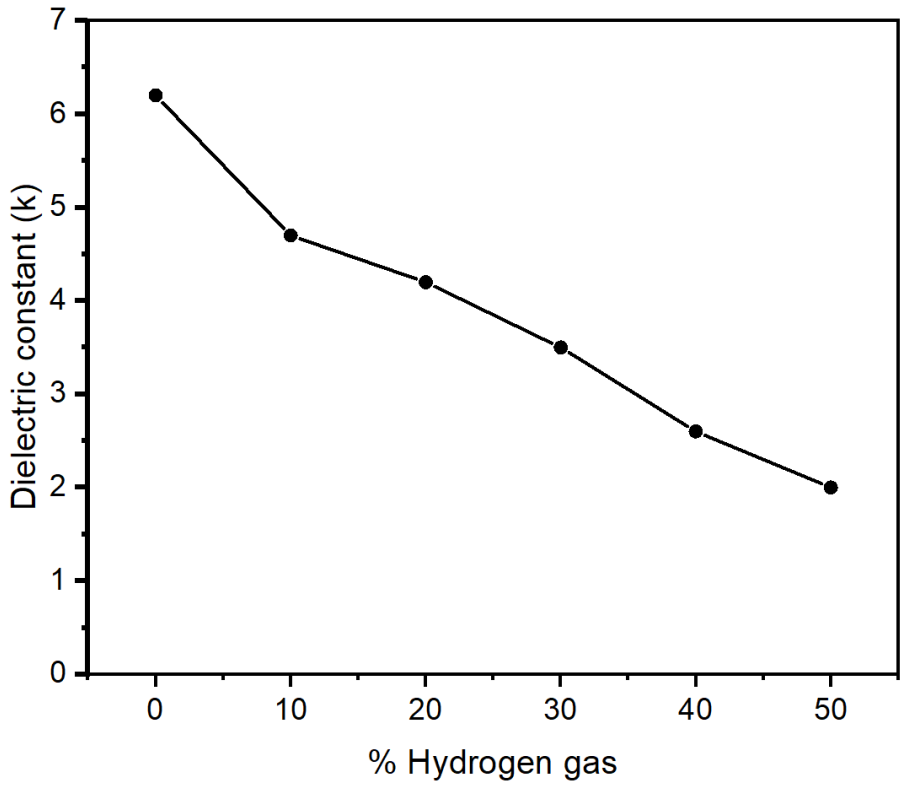

Figure 4.20: The dielectric constant of BCN and BCN:H thin films with varying hydrogen gas flow.

The electrical resistivity of BCN and BCN:H thin films was extracted from the I-V characteristics of the MIM device. Figure 4.21 shows the electrical resistivity trends of BCN and BCN:H thin films with varying percentages of hydrogen gas. Pure BCN film with no hydrogen doping displayed a maximum resistivity of 4.2×10^{11} ohm-cm. With hydrogen introduction in the sputtering chamber, the resistivity dropped to slightly lower values of 1.1×10^{11} ohm-cm. The films did not display strong dependence of resistivity on the percentage hydrogen gas flow. A similar trend was reported for BCN films with k=2.2 and $\rho = 10^{9}$-10^{11} ohm-cm deposited using PECVD [66, 167].

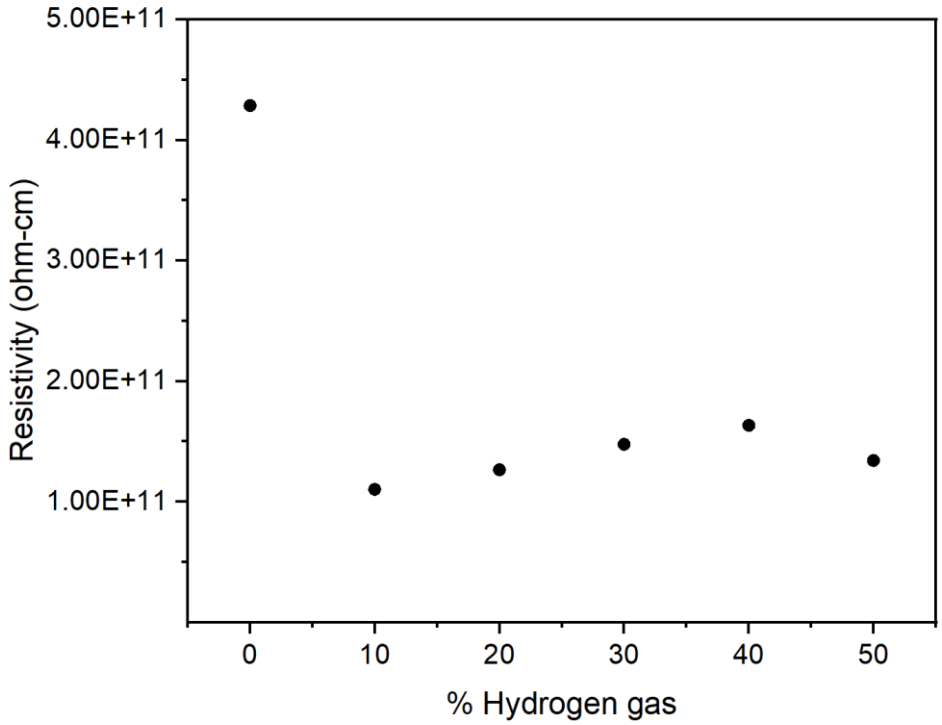

Figure 4.21: Electrical resistivity trend of BCN and BCN:H thin films.

4.3.3 Optical Properties

Optical transmission measurement was done on all BCN and BCN:H thin films deposited on the glass substrates. The optical transmission spectra measured in the wavelength range of 350-800 nm are shown in figure 4.22. High transmission (>88%) was observed for all films. BCN film deposited in the absence of hydrogen gas displayed transmission in the range of 88-94%. However, films deposited in the presence of hydrogen gas displayed a higher optical transmission value of 97-99%. This observation of an increase in transmission with the increase in hydrogen content is in accordance with other research studies on BCN:H [123] and similar dielectric materials such as SiC:H [168].

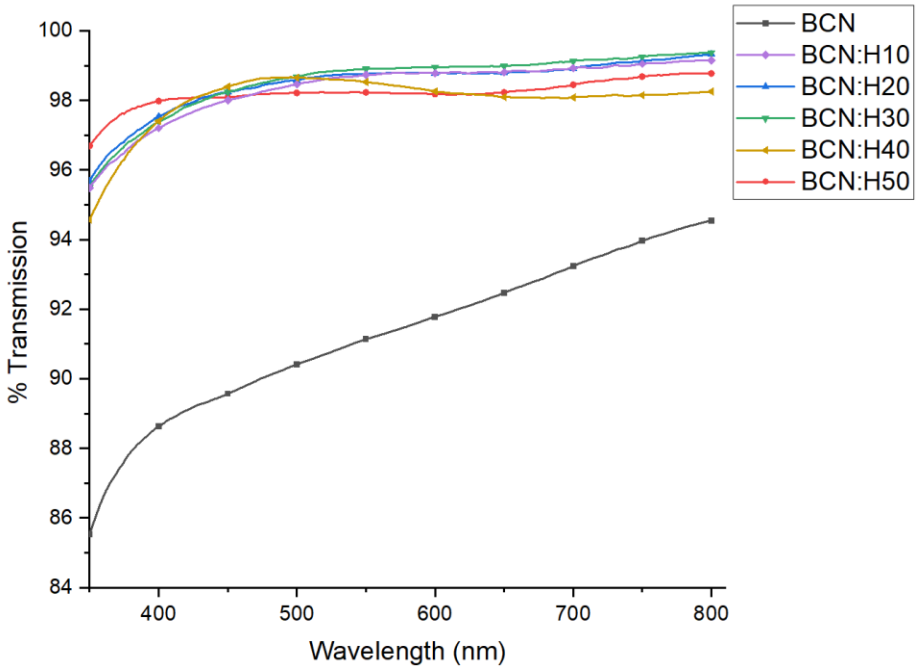

Figure 4.22: Optical transmission of BCN and BCN:H thin films measured on glass substrates.

4.4 BCN Nano-Coatings for Bacterial Inhibition

4.4.1 Surface Characterization of Nano-Coatings

The surface morphology of BCN and TiO_2 nano-coatings was evaluated using FESEM. Figure 4.23 a-c shows the surface images of U-C, TiO_2-C, and BCN-C. U-C demonstrated a smooth surface morphology. TiO_2-C displayed only slight protrusions but overall a smooth morphology. Compared to U-C and TiO_2-C, the BCN-C surface displayed significant nano protrusions. Owing to the differences between the two catheter surfaces, AFM was performed to evaluate the surface roughness of U-C and BCN-C. Figure 4.23 d-e shows the AFM scans of U-C and BCN-C conducted on the catheter surfaces. The surface roughness of U-C and BCN-C was recorded to be 41.7 nm

and 90.7 nm respectively using AFM. BCN-C displayed 15-fold higher peak gradient difference compared to U-C as recorded from separate 10μm^2 surface area scans on the catheters.

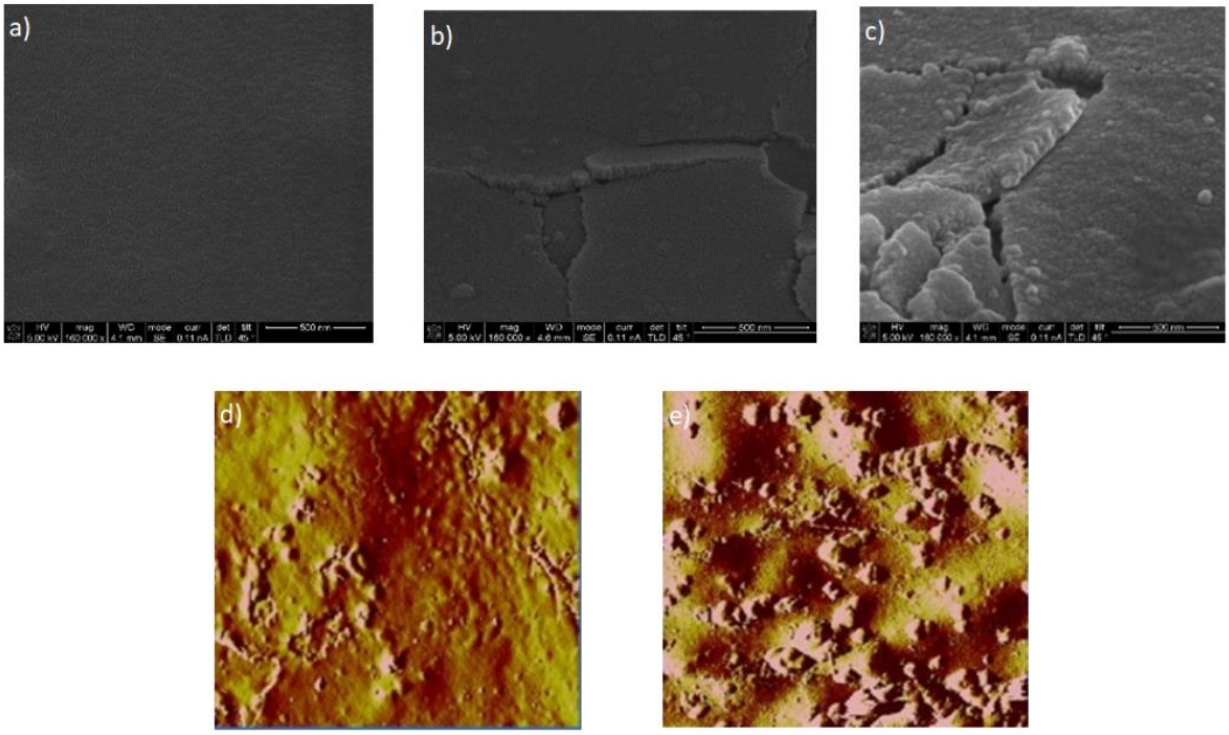

Figure 4.23: FESEM surface images showing smooth morphological features on (a) U-C, (b) TiO_2-C, and nano-protrusions on (c) BCN-C. AFM surface topology of (d) U-C and (e) BCN-C.

4.4.2 Inhibitory Effects of BCN Nano Coated Catheters on Bacterial Growth

Bacterial colony-forming units (CFUs) were manually counted for both E.coli and B.cereus after 24 hours of incubation. Table 4.4 shows the CFUs of E.coli bacterial for U-C, TiO_2-C, and BCN-C. The results of three individual experiments are displayed in the table. The uncoated catheters demonstrated the highest number of bacterial CFUs, as expected, which leads to CLABSIs among

patients. TiO_2-C demonstrated slightly lower CFUs compared to U-C, however, this difference was not significant. This implies that TiO_2-C does not inhibit E.coli bacterial growth on catheters. It can be seen that the average CFUs of U-C was 29.7, which reduced to 24 for TiO_2-C, and 5.6 for BCN-C. BCN-C demonstrated a substantial reduction in E.coli CFU's thus establishing the anti-bacterial activity of BCN nano-coatings. While TiO_2-C was only able to inhibit bacterial colonies by 19.19%, BCN-C displayed immense E.coli inhibitory effects up to 81.14%.

Table 4.4: Number of colony forming units of E.coli bacteria on U-C, TiO_2-C, and BCN-C.

Trial	Number of CFUs			Average % Decrease in CFU	
	U-C	TiO_2-C	BCN-C	TiO_2-C	BCN-C
1	29	24	3	19.19	81.14
2	26	20	4		
3	34	28	10		
Average	29.7	24.0	5.6		

Table 4.5 shows the CFUs of B.cereus bacterial colonies recorded on U-C, TiO_2-C, and BCN-C after incubation. Results are displayed as triplicates for the three individual experiments performed. The average number of B.cereus CFUs was 104.3 for U-C, which reduced to 84.3 for TiO_2-C and only 3 for BCN-C. TiO_2-C demonstrated only 19.17% decrease in bacterial colonies of B.cereus, similar to E.coli. BCN-C exhibited an excellent 97.12% decrease in B.cereus bacterial colonization.

This outstanding reduction in the bacterial activity of E.coli and B.cereus on BCN-C is attributed to the surface distinctive surface roughness of BCN-C. When a surface is observed under magnification, it appears as a series of peaks and valleys with varying heights and spacing. Height

variation between the peaks and valleys determines the surface roughness of the material. It is commonly accepted that nano rough surfaces tend to have a lower probability of bacterial adhesion as compared to smoother surfaces [169]. A similar trend between bacterial adhesion and surface roughness of the nano-coating has been reported in the literature [170-174].

Table 4.5: Number of colony forming units of B.cereus on U-C, TiO_2-C and BCN-C.

Trial	Number of CFUs			Average % decrease in CFUs	
	U-C	TiO_2-C	BCN-C	TiO_2-C	BCN-C
1	96	67	1	19.17	97.12
2	101	88	2		
3	116	98	6		
Average	104.3	84.3	3.0		

Figures 4.24 a-c show the bacterial colonies of E.coli after the catheter surfaces were rolled onto nutrient agar plate. Figures 4.24 d-f show the bacterial colonies of B.cereus after the catheter surfaces were rolled onto the surface of the blood agar plate. The average number of CFUs formed on U-C, TiO_2-C, and BCN-C were examined for statistical significance, as shown in Figure 4.24 g-h. One-tailed t-test analysis was used to determine the p-value. The lower the p-value, the higher is the significance of the data achieved. BCN-C successfully reduced bacterial CFUs formed by E.coli with p-value of 0.0008, thus confirming statistical significance. Similarly, BCN-C displayed an excellent reduction in bacterial CFUs for B.cereus with a highly significant p-value of 0.00004.

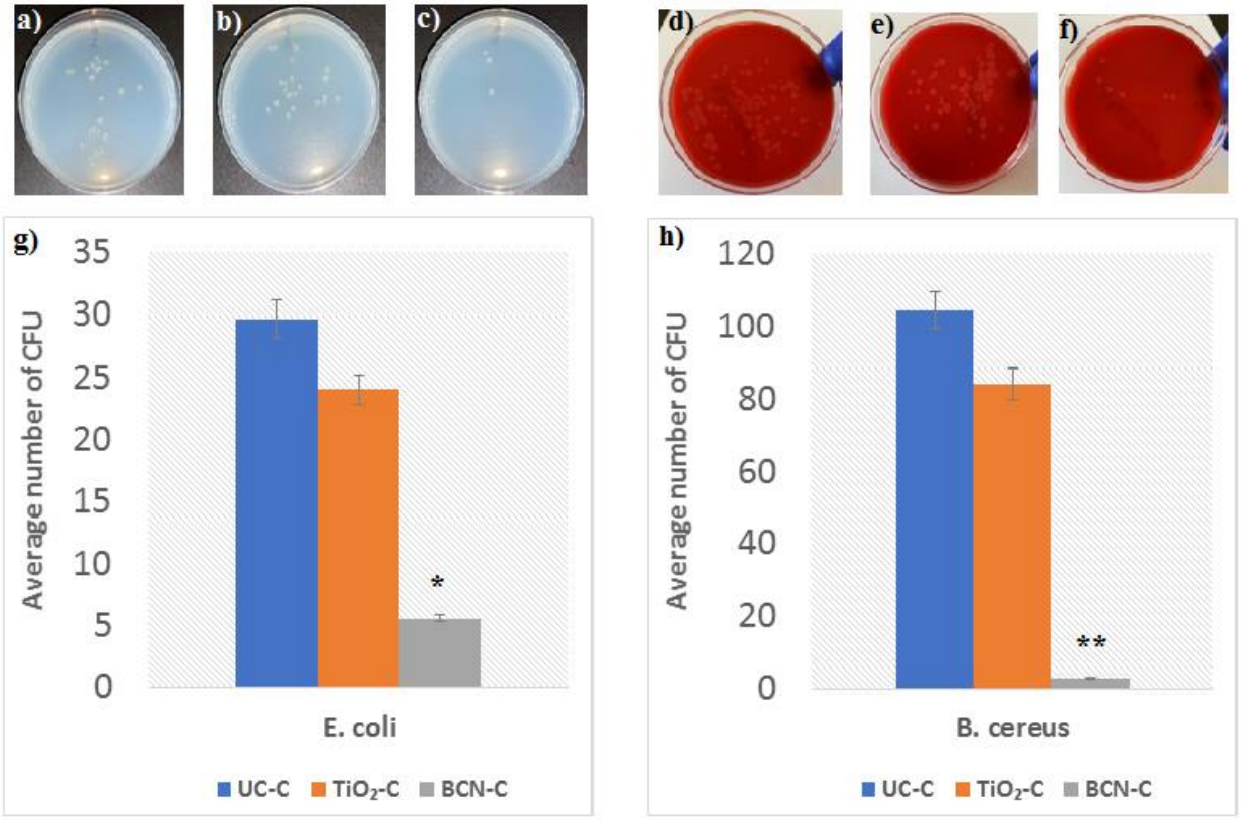

Figure 4.24: Microbial activity recorded for (a) U-C, (b) TiO2-C, and (c) BCN-C after rolling the catheters onto the surface of nutrient agar plate for E.coli. Microbial activity recorded for (d) U-C, (e) TiO2-C, and (f) BCN-C after rolling the catheters onto the surface of blood agar plate for B.cereus. Bar graph demonstration of bacterial inhibition property of (g) E.coli and (h) B.cereus for all catheters. * Represents a statistically significant difference of $p<0.05$. ** represents $p<0.01$.

4.4.3 Analysis of Biofilm Formation

To understand the mechanism of strong bacterial inhibition property demonstrated by BCN-C, biofilm formation was quantified using absorbance spectrophotometry. Table 4.6 shows the optical density values recorded for the crystal violet-stained biofilms formed by E.coli and B.cereus. The average OD of E.coli stained biofilms for three experimental measurements reduced from 0.4851 for U-C to 0.1837 for BCN-C. The average OD of B.cereus stained biofilms reduced from 0.5880 for U-C to 0.1439 for BCN-C. Thus, BCN-C evidently reduced the biofilm formation by 62.13% for E.coli and 75.52% for B.cereus. The surface roughness property of BCN nano-coatings impacts the surface topography, which results in biofilm inhibition [100]. BCN-C surface topographic features are in the nanometric range, which is much smaller than the microbial cell size. As a result, there is a significant decrease in the contact area between the bacterial cell and the nanocoated surface. This may determine the activation of bacterial adhesion genes and genes that secrete extracellular matrix, thereby impacting cell attachment and subsequent biofilm formation on BCN-C. Multiple studies have reported that surface topography plays a crucial role in bacterial adhesion and subsequent biofilm formation [170, 175, 176]. These results indicate the antibiofilm activity of BCN nano-coatings. Antibiofilm and bacterial inhibitory effect of BCN-C reduced colonization rate of CVCs and could potentially reduce the incidences of CLABSIs. This will be beneficial towards reduction in the use of antibiotics and deter the development of antibiotic-resistant organisms. Excellent bacterial inhibition property of BCN nano-coatings should be further explored for other medical device associated infections.

Table 4.6: Optical density (OD) of E.coli and B.cereus of U-C and BCN-C.

Trial	OD of E. coli stained catheters		% decrease in E. coli OD	OD of B. cereus stained catheters		% decrease in B. cereus OD
	U-C	BCN-C		U-C	BCN-C	
1	0.4868	0.1839	62.13	0.6398	0.1451	75.52
2	0.5006	0.1613		0.5308	0.1271	
3	0.4680	0.2070		0.5964	0.1589	
Average	0.4851	0.1837		0.5880	0.1439	

CHAPTER FIVE: CONCLUSION

Dissertation Remarks

Advancing towards the search for new dielectric materials, hydrogenation was performed on the materials in the boron-carbon-nitrogen triangle elements. Boron carbide and boron carbon nitride are popular for their low dielectric values. Hydrogenation was performed on BC and BCN thin films to study the investigation of hydrogen gas flow and other process parameters on electrical, optical, mechanical, photoluminescence properties of thin films. BC and BCN films were deposited in presence of H_2, N_2, and argon gas at different substrate temperatures using RF magnetron sputtering of B_4C and BN targets.

Amorphous BC:H films were grown using RF magnetron sputtering of B_4C target in presence of 3% H_2Ar gas at different substrate temperatures. These films incorporated higher elemental C content with substrate temperature. XPS revealed an increase in sp^2 bonded C content in the films with increasing substrate temperature. The increase in C content was accompanied by a corresponding decrease in the B/C ratio. REELS analysis confirmed the presence of hydrogen in the films. These carbon enriched films of a-BC:H exhibited reduced dielectric constant values of 3.5 and electrical resistivity in the order of 10^8 ohm-cm. Hydrogenation reduced the k-value of BC thin films by 56%. Optical transmission were achieved between 75-82% and optical bandgap between 2.25 and 2.6 eV by varying substrate temperature. Amorphous BC:H thin films deposited by RF magnetron sputtering are promising as insulating materials for low dielectric applications.

As hydrogenation of boron carbide showed promising electrical results, next hydrogenation of BCN thin films and its impact on mechanical properties and photoluminescence studies was investigated. BCN:H thin films were successfully deposited using dual-target RF magnetron sputtering from B_4C and BN. The mechanical properties such as hardness and Young's modulus were investigated using nanoindentation measurements. Photoluminescence studies were performed at RT and 77 K. The hydrogen/argon to nitrogen gas ratio was varied during deposition while the substrate temperature was maintained constant at room temperature to obtain films with wide elemental composition. The influence of substrate temperature was also studied by varying deposition substrate temperature at a constant gas flow ratio. The films demonstrated distinct properties with the deposition conditions. The boron content in the films increased with a higher hydrogen/argon gas ratio. The maximum boron was recorded as 35% at a gas ratio of 1. The carbon content varied only slightly with change in the gas ratio. The nitrogen content displayed an overall decreasing trend, except for the increase in the N content to 25% at gas ratio of 0.8. The films demonstrated a different elemental composition with variations in substrate temperature. Carbon and nitrogen content increased at higher substrate temperatures. Higher substrate temperature produced boron-rich BCN:H thin films. Oxygen contamination was less than 10%. The presence of B-N-B, C-N, C≡N, B–H, and C=O bonds were revealed from the FTIR transmittance spectrum.

The Young's modulus of the films displayed a decreasing trend with gas ratio variation. The Young's modulus reduced from 140 GPa for the film deposited at gas ratio of 0.2 to 126 GPa for the film deposited at gas ratio of 0.6. The reduction in Young's modulus was attributed to the

phase transitions from sp^2 to sp^3 when H atoms are bonded with B/C/N atoms. As a function of substrate temperature, Young's modulus showed an overall increasing trend from 132 GPa for the film deposited at RT to 140 GPa for the film deposited at 400 °C.

The BCN:H thin films exhibited an interesting hardness trend with variation in hydrogen/argon to nitrogen gas flow ratios and substrate temperatures. The BCN:H thin films exhibited decreasing hardness values for gas ratios of 0, 0.2, and 0.4, with the lowest hardness recorded at 6 GPa. However, for the film deposited at gas ratio of 1, the films demonstrated an increased hardness of 18 GPa. This increase in hardness values was attributed to phase transitions in the films as observed in the FTIR transmittance spectra. The hardness of BCN:H thin films increased from 18 GPa for the film deposited at RT to 22 GPa for the film deposited at 400 °C.

The PL peaks of BCN:H thin films can be tuned based on the varying gas flow ratio and substrate deposition temperatures during RF magnetron sputtering. BCN and BCN:H films exhibited two sharp PL peaks. Increasing the hydrogen gas flow ratio helped attain tunable films with PL peaks varying from 490 nm to 515 nm (green shift) and 591 nm to 621 nm (red shift). With an increase in the substrate temperature, the PL peaks shifted to longer wavelengths. BCN:H thin film deposited at RT exhibited a peak at 490 nm and 591 nm. As the substrate temperature increased, the peaks shifted to 521 nm and 627 nm for the film G deposited at 100 °C, 521 nm and 627 nm for the film H deposited at 200 °C, 544 nm and 655 nm for the film I deposited at 300 °C. The origin of PL peak shift to longer wavelength was associated with higher C content in the films, which causes a reduction in the bandgap. BCN-based phosphors up to 655 nm sharp red emission

were reported for the first time through this study. PL peak intensity increased with higher hydrogen gas ratio in the deposited BNC:H thin films by ~10,000 units. This increment in the PL peak intensity with hydrogen gas shows potential for hydrogen sensing application of BCN:H thin films.

Hydrogenation of BCN thin films also produced a rare phenomenon of NTQ. The occurrence of this phenomenon was related to the radiation recombination of localized states related to H and N bonding in the BCN:H thin films. BCN:H films emitting bright and stable red, green and blue (RGB) luminescence under the single excitation of 365 nm wavelength can be potentially applicable in LEDs, optoelectronics, bioimaging, and optical thermometry devices.

As 3% hydrogenation reduced the dielectric constant of BCN films by 56%, the impact of 99.99% hydrogen gas on BCN thin films was analyzed on electrical and optical properties. Hydrogenated BCN thin films were deposited using dual-target RF magnetron sputtering for potential low-k dielectric applications. The H_2/N_2 gas ratio was varied while maintaining constant Ar gas flow for all depositions to achieve a wide range of hydrogen doping. The films demonstrated varying elemental composition with process gas flow. All films exhibited B-C-N atomic hybridization observed in XPS studies. The carbon elemental composition increased with a corresponding decrease in nitrogen as a function of hydrogen gas flow. The number of non-polar C-H bonds was found to increase with hydrogen process gas flow during deposition. A 67.74% reduction in k-value was achieved from 6.2 to 2 due to non-polar C-C and C-H bonds which reduced polarization in thin films. A dielectric constant as low as 2 has been achieved for the first time for BCN:H thin

films deposited using RF magnetron sputtering technique. BCN:H thin films demonstrated high electrical resistivity of 10^{11} ohm-cm. The BCN:H thin films with low dielectric constant (k=2) and high resistivity (10^{11} ohm-cm) are promising candidates as insulating materials for low-k dielectric applications.

BCN nano-coatings were investigated for the first time for their bacterial inhibition property on central venous catheters. BCN nano-coatings were synthesized using RF magnetron sputtering from B_4C target in the presence of nitrogen/argon gas. BCN-C reduced the bacterial CFU's by 81.14% for E.coli and 97.12% for B.cereus. TiO_2-C was also investigated for comparison purposes, and it reduced bacterial CFU's by only 19% for both E.coli and B.cereus. BCN nanocoatings suppressed the biofilm formation for E.coli by 62.13% and B.cereus by 75.52%. The excellent bacterial inhibition and antibiofilm property of was attributed to the surface roughness of BCN nanocoated central venous catheters.

Future Prospects

Hydrogenation of BC and BCN thin films have displayed a reduction in the k value by 56% and 67%, respectively. The influence of 3% hydrogen gas and 99.99% hydrogen gas on BCN thin films was investigated. The incorporation of 99.99% hydrogen gas has shown promising results in the electrical properties of BCN thin films. Higher gas flow (> 10 sccm) of 99.99% hydrogen gas flow to the deposition chamber should be explored further. Some of the other crucial properties which can be studied include mechanical properties and photoluminescence studies. 3% hydrogenation of BCN exhibited tunable photoluminescence properties with process deposition parameters.

BCN-based phosphors have been synthesized using various techniques such as solid-state reaction, molten salt growth, and microwave method, to name a few. Due to the wide range of excitation and emission spectra, BCN and BCN:H have great potential in white LEDs, DNA labeling, optoelectronic devices, and biological imaging applications. However, BCN and BCN:H based phosphors deposited by RF magnetron sputtering remain much less explored and hence require further investigation.

Hydrogenated BCN is emerging as a potential low-dielectric candidate material displaying a low k value of 2. Many materials researched in the past showed low-k dielectric values but poor mechanical properties. However, BCN is well known for its high hardness and Young's modulus values and low dielectric constant and hence is a promising candidate for ILDs. Integrating the film into the semiconductor device manufacturing process is one of the crucial challenges. Post deposition patterning by etching of BCN and hydrogenated BCN materials to architect the desired patterns as a viable interlayer material in the semiconductor devices needs to be explored. There are very few studies on the etching of BCN and BCN:H thin films. Detailed etching experiments need to be investigated to find the feasibility of using BCN as ILD in semiconductor devices.

BCN nanomaterials are popular for their strong adsorption properties. Literature also reports the great hydrogen uptake capacity of BCN, making them prominent as a clean energy alternative material. The hydrogen uptake capacity of BCN deposited with RF magnetron sputtering must be investigated by allowing the thin films to soak the hydrogen gas in the deposition chamber.

Detailed investigations on adsorptive properties need to be pursued for future clean energy demands.

BCN nano-coatings inhibiting bacterial growth and biofilm formation were reported for the first time in this dissertation. These studies were performed on central venous catheters. These unique surface properties of BCN nano-coatings for bacterial inhibition should be explored further to reduce other medical device-associated infections. Multilayers of BCN and other anti-bacterial coatings such as Ag can be explored for coatings on medical devices.

REFERENCES

[1] Arden WM. The international technology roadmap for semiconductors—perspectives and challenges for the next 15 years. Current Opinion in Solid State and Materials Science. 2002;6:371-7.

[2] Mocella MT. Fluorinated compounds for advanced IC interconnect applications: a survey of chemistries and processes. Journal of fluorine chemistry. 2003;122:87-92.

[3] King SW, Simka H, Herr D, Akinaga H, Garner M. Research Updates: The three M's (materials, metrology, and modeling) together pave the path to future nanoelectronic technologies. APL Materials. 2013;1:040701.

[4] Muraka SP, Eizenberg M, Sinha AK. Interlayer dielectrics for semiconductor technologies: Elsevier; 2003.

[5] Prakash A. Deposition and characterization studies of boron carbon nitride (BCN) thin films prepared by dual target sputtering. 2016.

[6] Zhao B, Brongo M. Integration of Low Dielectric Constant Materials in Advanced Aluminum and Copper Interconnects. MRS Online Proceedings Library. 1999;564:485-97.

[7] Maex K, Baklanov M, Shamiryan D, Lacopi F, Brongersma S, Yanovitskaya ZS. Low dielectric constant materials for microelectronics. Journal of Applied Physics. 2003;93:8793-841.

[8] Frenkel J. On pre-breakdown phenomena in insulators and electronic semi-conductors. Physical Review. 1938;54:647.

[9] Fowler RH, Nordheim L. Electron emission in intense electric fields. Proceedings of the Royal Society of London Series A, Containing Papers of a Mathematical and Physical Character. 1928;119:173-81.

[10] Mattox D, Bunshah R. Deposition technologies for films and coatings. Noyes, New York. 1982.

[11] Lee HS, Lee AS, Baek K-Y, Hwang SS. Low dielectric materials for microelectronics. Dielectric Material. 2012:59.

[12] Moore TM, Hartfield CD, Anthony JM, Ahlburn BT, Ho PS, Miller MR. Mechanical characterization of low-K dielectric materials. AIP Conference Proceedings: American Institute of Physics; 2001. p. 431-9.

[13] Vasilopoulou M, Tsevas S, Douvas A, Argitis P, Davazoglou D, Kouvatsos D. Characterization of various low-k dielectrics for possible use in applications at temperatures below 160° C. Journal of Physics: Conference Series: IOP Publishing; 2005. p. 054.

[14] Andideh E, Lerner M, Palmrose G, El-Mansy S, Scherban T, Xu G, Blaine J. Compositional effects on electrical and mechanical properties in carbon-doped oxide dielectric films: Application of Fourier-transform infrared spectroscopy. Journal of Vacuum Science & Technology B: Microelectronics and Nanometer Structures Processing, Measurement, and Phenomena. 2004;22:196-201.

[15] Andricacos PC, Uzoh C, Dukovic JO, Horkans J, Deligianni H. Damascene copper electroplating for chip interconnections. IBM Journal of Research and Development. 1998;42:567-74.

[16] Hu C, Gignac L, Malhotra S, Rosenberg R, Boettcher S. Mechanisms for very long electromigration lifetime in dual-damascene Cu interconnections. Applied Physics Letters. 2001;78:904-6.

[17] Antonelli G, Jiang G, Shaviv R, Mountsier T, Dixit G, Park K, Karim I, Wu W, Shobha H, Spooner T. Synergistic combinations of dielectrics and metallization process technology to achieve 22 nm interconnect performance targets. Microelectronic engineering. 2012;92:9-14.

[18] Grill A, Gates SM, Ryan TE, Nguyen SV, Priyadarshini D. Progress in the development and understanding of advanced low k and ultralow k dielectrics for very large-scale integrated interconnects—State of the art. Applied Physics Reviews. 2014;1:011306.

[19] Todi VO, Shantheyanda BP, Todi RM, Sundaram KB, Coffey K. Optical characterization of BCN films deposited at various N2/Ar gas flow ratios by RF magnetron sputtering. Materials Science and Engineering: B. 2011;176:878-82.

[20] Nordell BJ, Karki S, Nguyen TD, Rulis P, Caruso A, Purohit SS, Li H, King SW, Dutta D, Gidley D. The influence of hydrogen on the chemical, mechanical, optical/electronic, and electrical transport properties of amorphous hydrogenated boron carbide. Journal of Applied Physics. 2015;118:035703.

[21] Jiménez I, Torres R, Caretti I, Gago R, Albella JM. A review of monolithic and multilayer coatings within the boron–carbon–nitrogen system by ion-beam-assisted deposition. Journal of Materials Research. 2012;27:743-64.

[22] Zhang X. Doping and electrical properties of cubic boron nitride thin films: A critical review. Thin Solid Films. 2013;544:2-12.

[23] Sezer AO, Brand J. Chemical vapor deposition of boron carbide. Materials Science and Engineering: B. 2001;79:191-202.

[24] Thevenot F. Boron carbide—a comprehensive review. Journal of the European Ceramic society. 1990;6:205-25.

[25] Nehate S, Saikumar A, Prakash A, Sundaram K. A review of boron carbon nitride thin films and progress in nanomaterials. Materials Today Advances. 2020;8:100106.

[26] Ying Z, Yu D, Ling H, Xu N, Lu Y, Sun J, Wu J. Synthesis of BCN thin films by nitrogen ion beam assisted pulsed laser deposition from a B4C target. Diamond and related materials. 2007;16:1579-85.

[27] Kawaguchi M. B/C/N materials based on the graphite network. Advanced Materials. 1997;9:615-25.

[28] Li Y, Gao W, Wang F, Zhao D, Zhang Y, Yin H. Self-ordered orientation of crystalline hexagonal boron nitride nanodomains embedded in boron carbonitride films for band gap engineering. Coatings. 2019;9:185.

[29] Umeda S, Yuki T, Sugiyama T, Sugino T. Boron carbon nitride film with low dielectric constant as passivation film for high speed electronic devices. Diamond and related materials. 2004;13:1135-8.

[30] Wang C, Xiao J, Shen Q, Zhang L. Bonding structure and mechanical properties of BCN thin films synthesized by pulsed laser deposition at different laser fluences. Thin Solid Films. 2016;603:323-7.

[31] Prakash A, Sundaram KB. Studies on electrical properties of RF sputtered deposited boron carbon nitride thin films. ECS Journal of Solid State Science and Technology. 2015;4:N25.

[32] Hirte T, Feuerfeil R, Perez-Solorzano V, Wagner T, Scherge M. Influence of composition on the wear properties of boron carbonitride (BCN) coatings deposited by high power impulse magnetron sputtering. Surface and Coatings Technology. 2015;284:94-100.

[33] Wu Z, Wang Y, Li S, Wang X, Xu Z, Zhou F. Mechanical and tribological properties of BCN coatings sliding against different wood balls. Science and Engineering of Composite Materials. 2019;26:402-11.

[34] Xu S, Ma X, Wen H, Tang G, Li C. Effect of annealing on the mechanical and scratch properties of BCN films obtained by magnetron sputtering deposition. Applied surface science. 2014;313:823-7.

[35] Prakash A, Nehate SD, Sundaram KB. Boron carbon nitride based metal-insulator-metal UV detectors for harsh environment applications. Optics letters. 2016;41:4249-52.

[36] Caicedo J, Caicedo H, Aperador W. TiN [BCN/BN] n/c-BN system improves the surface properties of machining tools used in industrial applications. The International Journal of Advanced Manufacturing Technology. 2015;77:819-30.

[37] Li Y, Jia X, Shi W, Leng S, Ma H-a, Sun S, Wang F, Chen N, Long Y. The preparation of new "BCN" diamond under higher pressure and higher temperature. International Journal of Refractory Metals and Hard Materials. 2014;43:147-9.

[38] Deng X, Kousaka H, Tokoroyama T, Umehara N. Deposition and tribological behaviors of ternary BCN coatings at elevated temperatures. Surface and Coatings Technology. 2014;259:2-6.

[39] Freire Jr F, Reigada D, Prioli R. Boron Carbide and Boron–Carbon Nitride Films Deposited by DC-Magnetron Sputtering: Structural Characterization and Nanotribological Properties. physica status solidi (a). 2001;187:1-12.

[40] Mannan MA, Noguchi H, Kida T, Nagano M, Hirao N, Baba Y. Chemical bonding states and local structures of the oriented hexagonal BCN films synthesized by microwave plasma CVD. Materials science in semiconductor processing. 2008;11:100-5.

[41] Baake O, Hoffmann PS, Klein A, Pollakowski B, Beckhoff B, Kosinova ML, Fainer NI, Sulyaeva VS, Trunova VA, Ensinger W. Speciation of BC x N y films grown by PECVD with trimethylborazine precursor. Analytical and bioanalytical chemistry. 2009;395:1901-9.

[42] Kosolapova TY, Makarenko G, Serebryakova T, Prilutskii E, Khorpyakov O, Chernysheva O. Nature of boron carbonitride I. Conditions of preparation of boron carbonitride. Soviet Powder Metallurgy and Metal Ceramics. 1971;10:22-6.

[43] Zhuang C, Zhao J, Jia F, Guan C, Wu Z, Bai Y, Jiang X. Tuning bond contents in B–C–N films via temperature and bias voltage within RF magnetron sputtering. Surface and Coatings Technology. 2009;204:713-7.

[44] Nakao S, Sonoda T, Tsugawa K, Choi J, Kato T. Effects of nitrogen gas ratio on composition and microstructure of BCN films prepared by RF magnetron sputtering. Vacuum. 2009;84:642-7.

[45] Ulrich S, Theel T, Schwan J, Ehrhardt H. Magnetron-sputtered superhard materials. Surface and coatings Technology. 1997;97:45-59.

[46] Linss V, Hermann I, Schwarzer N, Kreissig U, Richter F. Mechanical properties of thin films in the ternary triangle B–C–N. Surface and Coatings Technology. 2003;163:220-6.

[47] Morant C, Prieto P, Bareno J, Sanz J, Elizalde E. Hard BCxNy thin films grown by dual ion beam sputtering. Thin Solid Films. 2006;515:207-11.

[48] Čapek J, Batková Š, Haviar S, Houška J, Čerstvý R, Zeman P. Effect of annealing on structure and properties of Ta–O–N films prepared by high power impulse magnetron sputtering. Ceramics International. 2019;45:9454-61.

[49] Perrone A, Caricato A, Luches A, Dinescu M, Ghica C, Sandu V, Andrei A. Boron carbonitride films deposited by pulsed laser ablation. Applied surface science. 1998;133:239-42.

[50] Teodorescu V, Luches A, Dinu R, Zocco A, Ciobanu M, Martino M, Sandu V, Dinescu M. Influence of the substrate temperature on BCN films deposited by sequential pulsed laser deposition. Applied Physics A. 1999;69:S667-S70.

[51] Xiao J, Wang C, Shen Q, Zhang L. Influence of nitrogen pressure on bonding structure and mechanical properties of pulsed laser deposited BCN thin films. Surface and Coatings Technology. 2015;276:141-4.

[52] Caretti I, Jimenez I, Albella J. BCN films with controlled composition obtained by the interaction between molecular beams of B and C with nitrogen ion beams. Diamond and related materials. 2003;12:1079-83.

[53] Yasui H, Hirose Y, Awazu K, Iwaki M. The properties of BCN films formed by ion beam assisted deposition. Colloids and Surfaces B: Biointerfaces. 2000;19:291-5.

[54] Baake O, Hoffmann P, Klein A, Pollakowski B, Beckhoff B, Ensinger W, Kosinova M, Fainer N, Sulyaeva V, Trunova V. Chemical character of BCxNy layers grown by CVD with trimethylamine borane. X-Ray Spectrometry: An International Journal. 2009;38:68-73.

[55] Kida T, Shigezumi K, Mannan MA, Akiyama M, Baba Y, Nagano M. Synthesis of boron carbonitride (BCN) films by plasma-enhanced chemical vapor deposition using trimethylamine borane as a molecular precursor. Vacuum. 2009;83:1143-6.

[56] Kosinova M, Rumyantsev YM, Fainer N, Maximovski E, Kuznetsov F. The structure study of boron carbonitride films obtained by use of trimethylamine borane complex. Nuclear

Instruments and Methods in Physics Research Section A: Accelerators, Spectrometers, Detectors and Associated Equipment. 2001;470:253-7.

[57] Tay RY, Li H, Tsang SH, Zhu M, Loeblein M, Jing L, Leong FN, Teo EHT. Trimethylamine borane: A new single-source precursor for monolayer h-BN single crystals and h-BCN thin films. Chemistry of Materials. 2016;28:2180-90.

[58] Baake O, Hoffmann PS, Kosinova ML, Klein A, Pollakowski B, Beckhoff B, Fainer NI, Trunova VA, Ensinger W. Analytical characterization of BC x N y films generated by LPCVD with triethylamine borane. Analytical and bioanalytical chemistry. 2010;398:1077-84.

[59] Badzian A, Appenheimer S, Niemyski T, Olkusnik E. Graphite--boron nitride solid solutions by chemical vapor deposition. Proceedings of the third international conference on chemical vapor deposition1972.

[60] Oliveira M, Conde O. Synthesis and properties of BxCyNz coatings. Journal of Materials Research. 2001;16:734-43.

[61] Ling H, Wu J, Sun J, Shi W, Ying Z, Li F. Electron cyclotron resonance plasma-assisted pulsed laser deposition of boron carbon nitride films. Diamond and related materials. 2002;11:1623-8.

[62] Prakash A, Sundaram KB, Campiglia AD. Photoluminescence studies on BCN thin films synthesized by RF magnetron sputtering. Materials Letters. 2016;183:355-8.

[63] Zhang T, Zhang J, Wen G, Zhong B, Xia L, Huang X, Zhao H, Wang H, Qin L. Ultra-light h-BCN architectures derived from new organic monomers with tunable electromagnetic wave absorption. Carbon. 2018;136:345-58.

[64] Gago R, Jimenez I, Agullo-Rueda F, Albella J, Czigany Z, Hultman L. Transition from amorphous boron carbide to hexagonal boron carbon nitride thin films induced by nitrogen ion assistance. Journal of applied physics. 2002;92:5177-82.

[65] Yuki T, Umeda S, Sugino T. Electrical and optical characteristics of boron carbon nitride films synthesized by plasma-assisted chemical vapor deposition. Diamond and related materials. 2004;13:1130-4.

[66] Sulyaeva VS, Kosinova ML, Rumyantsev YM, Kuznetsov FA, Kesler VG, Kirienko VV. Optical and electrical characteristics of plasma enhanced chemical vapor deposition boron carbonitride thin films derived from N-trimethylborazine precursor. Thin Solid Films. 2014;558:112-7.

[67] Lousa A, Martinez E, Esteve J, Pascual E. Micromechanical and Microtribological Properties of BCN Thin Films Near the B4C Composition Deposited by rf Magnetron Sputtering. Thin Solid Films. 1999;355:356.

[68] Byon E, Kim J-K, Lee S, Hah J-H, Sugimoto K. Mechanical properties of B□ C□ N films deposited by dual cesium ion beam sputtering system. Surface and Coatings Technology. 2003;169:340-3.

[69] Chen X, Wang Z, Ma S, Ji V, Chu PK. Microstructure and tribological properties of ternary BCN thin films with different carbon contents. Diamond and related materials. 2010;19:1225-9.

[70] Castillo H, Arango P, Vélez J, Restrepo-Parra E, Soto G, De la Cruz W. Synthesis and characterization of cubic BC2N grown by reactive laser ablation. Surface and Coatings Technology. 2010;204:4051-6.

[71] Liu X, Ma G, Sun G, Duan Y, Liu S. Effect of deposition and annealing temperature on mechanical properties of TaN film. Applied surface science. 2011;258:1033-7.

[72] Patsalas P, Charitidis C, Logothetidis S. The effect of substrate temperature and biasing on the mechanical properties and structure of sputtered titanium nitride thin films. Surface and Coatings Technology. 2000;125:335-40.

[73] Zhou F, Adachi K, Kato K. Influence of deposition parameters on surface roughness and mechanical properties of boron carbon nitride coatings synthesized by ion beam assisted deposition. Thin Solid Films. 2006;497:210-7.

[74] Prakash A, Todi V, Sundaram KB, Ross L, Xu G, French M, Henry P, King SW. Investigation of the dielectric and mechanical properties for magnetron sputtered BCN thin films. ECS Journal of Solid State Science and Technology. 2014;4:N3122.

[75] Bi K, Liu J, Dai QX. Effect of Target Power and Bias on Adhesive Force of BCN Films. Advanced Materials Research: Trans Tech Publ; 2011. p. 2148-51.

[76] Gago R, Jiménez I, Garcıa I, Albella J. Growth and characterisation of boron–carbon–nitrogen coatings obtained by ion beam assisted evaporation. Vacuum. 2002;64:199-204.

[77] Kulisch W. Deposition of Diamond-Like Superhard Materials in the B/C/N System. physica status solidi (a). 2000;177:63-79.

[78] Aoki H, Watanabe D, Moriyama R, Mazumder M, Komatsu N, Kimura C, Sugino T. Influence of moisture on BCN (low-K) film for interconnection reliability. Diamond and related materials. 2008;17:628-32.

[79] Watanabe M, Itoh S, Mizushima K, Sasaki T. Electrical properties of BC2N thin films prepared by chemical vapor deposition. Journal of applied physics. 1995;78:2880-2.

[80] Weber A, Bringmann U, Nikulski R, Klages C-P. Growth of cubic boron nitride and boron-carbon-nitrogen coatings using N-trimethylborazine in an electron cyclotron resonance plasma process. Diamond and related materials. 1993;2:201-6.

[81] Konno H, Ito T, Ushiro M, Fushimi K, Azumi K. High capacitance B/C/N composites for capacitor electrodes synthesized by a simple method. Journal of Power Sources. 2010;195:1739-46.

[82] Yu J, Wang E. Turbostratic boron carbonitride film and its field-emitting behavior. Applied physics letters. 1999;74:2948-50.

[83] Pramoda K, Moses K, Maitra U, Rao C. Superior performance of a MoS2-RGO composite and a Borocarbonitride in the electrochemical detection of dopamine, uric acid and adenine. Electroanalysis. 2015;27:1892-8.

[84] Watanabe M, Itoh S, Sasaki T, Mizushima K. Visible-light-emitting layered B C 2 N semiconductor. Physical review letters. 1996;77:187.

[85] Gupta A, Sakthivel T, Seal S. Recent development in 2D materials beyond graphene. Progress in Materials Science. 2015;73:44-126.

[86] Wang W-N, Ogi T, Kaihatsu Y, Iskandar F, Okuyama K. Novel rare-earth-free tunable-color-emitting BCNO phosphors. Journal of Materials Chemistry. 2011;21:5183-9.

[87] Yamamoto K, Ito H, Kujime S. Nano-multilayered CrN/BCN coating for anti-wear and low friction applications. Surface and Coatings Technology. 2007;201:5244-8.

[88] Rao C, Gopalakrishnan K. Borocarbonitrides, B x C y N z: Synthesis, Characterization, and Properties with Potential Applications. ACS applied materials & interfaces. 2017;9:19478-94.

[89] Qin L, Yu J, Kuang S, Xiao C, Bai X. Few-atomic-layered boron carbonitride nanosheets prepared by chemical vapor deposition. Nanoscale. 2012;4:120-3.

[90] Wu T, Shen H, Sun L, Cheng B, Liu B, Shen J. Nitrogen and boron doped monolayer graphene by chemical vapor deposition using polystyrene, urea and boric acid. New Journal of Chemistry. 2012;36:1385-91.

[91] Lei W, Portehault D, Dimova R, Antonietti M. Boron carbon nitride nanostructures from salt melts: tunable water-soluble phosphors. Journal of the American Chemical Society. 2011;133:7121-7.

[92] Hou F, Li Y, Gao Y, Hu S, Wu B, Bao H, Wang H, Jiang B. Non-metal boron modified carbon nitride tube with enhanced visible light-driven photocatalytic performance. Materials Research Bulletin. 2019;110:18-23.

[93] Loeblein M, Tay RY, Tsang SH, Ng WB, Teo EHT. Configurable Three-Dimensional Boron Nitride–Carbon Architecture and Its Tunable Electronic Behavior with Stable Thermal Performances. Small. 2014;10:2992-9.

[94] Chen D, Hu X, Huang Y, Qian Y, Li D. Facile fabrication of nanoporous BCN with excellent charge/discharge cycle stability for high-performance supercapacitors. Materials Letters. 2019;246:28-31.

[95] Gopalakrishnan K, Moses K, Govindaraj A, Rao C. Supercapacitors based on nitrogen-doped reduced graphene oxide and borocarbonitrides. Solid state communications. 2013;175:43-50.

[96] Yang M, Shi D, Sun X, Li Y, Liang Z, Zhang L, Shao Y, Wu Y, Hao X. Shuttle confinement of lithium polysulfides in borocarbonitride nanotubes with enhanced performance for lithium–sulfur batteries. Journal of Materials Chemistry A. 2020;8:296-304.

[97] Jimenez-Arevalo N, Leardini F, Ferrer IJ, Ares JR, Sanchez C, Saad Abdelnabi MM, Betti MG, Mariani C. Ultrathin Transparent B–C–N Layers Grown on Titanium Substrates with Excellent

Electrocatalytic Activity for the Oxygen Evolution Reaction. ACS Applied Energy Materials. 2020;3:1922-32.

[98] Lei N, Li J, Song Q, Liang Z. Construction of g-C3N4/BCN two-dimensional heterojunction photoanode for enhanced photoelectrochemical water splitting. International Journal of Hydrogen Energy. 2019;44:10498-507.

[99] Shiraishi Y, Chishiro K, Tanaka S, Hirai T. Photocatalytic dinitrogen reduction with water on boron-doped carbon nitride loaded with nickel phosphide particles. Langmuir. 2020;36:734-41.

[100] Naga V, Nehate SD, Saikumar AK, Sundaram KB. Boron Carbon Nitride (BCN) Nano-Coatings of Central Venous Catheters Inhibits Bacterial Colonization. ECS Journal of Solid State Science and Technology. 2020;9:115018.

[101] Suenaga K, Colliex C, Demoncy N, Loiseau A, Pascard H, Willaime F. Synthesis of nanoparticles and nanotubes with well-separated layers of boron nitride and carbon. Science. 1997;278:653-5.

[102] Piazza F, Nocua J, Hidalgo A, De Jesus J, Velazquez R, Weiss B, Morell G. Formation of boron carbonitride nanotubes from in situ grown carbon nanotubes. Diamond and related materials. 2005;14:965-9.

[103] Zhang Y, Gu H, Suenaga K, Iijima S. Heterogeneous growth of B□ C□ N nanotubes by laser ablation. Chemical Physics Letters. 1997;279:264-9.

[104] Mannan MA, Nagano M, Kida T, Hirao N, Baba Y. Characterization of BCN films synthesized by radiofrequency plasma enhanced chemical vapor deposition. Journal of Physics and Chemistry of Solids. 2009;70:20-5.

[105] Sulyaeva V, Rumyantsev YM, Kosinova M, Golubenko A, Fainer N, Kuznetsov F. Plasma enhanced chemical vapour deposition of BCxNy films prepared from N-trimethylborazine: Modelling, synthesis and characterization. Surface and Coatings Technology. 2007;201:9009-14.

[106] Han W-Q, Yu H-G, Liu Z. Convert graphene sheets to boron nitride and boron nitride–carbon sheets via a carbon-substitution reaction. Applied Physics Letters. 2011;98:203112.

[107] Ci L, Song L, Jin C, Jariwala D, Wu D, Li Y, Srivastava A, Wang Z, Storr K, Balicas L. Atomic layers of hybridized boron nitride and graphene domains. Nature materials. 2010;9:430-5.

[108] Li H, Tay RY, Tsang SH, Jing L, Zhu M, Leong FN, Teo EHT. Composition-controlled synthesis and tunable optical properties of ternary boron carbonitride nanotubes. RSC advances. 2017;7:12511-7.

[109] Akinwande D, Huyghebaert C, Wang C-H, Serna MI, Goossens S, Li L-J, Wong H-SP, Koppens FH. Graphene and two-dimensional materials for silicon technology. Nature. 2019;573:507-18.

[110] Karbhal I, Devarapalli RR, Debgupta J, Pillai VK, Ajayan PM, Shelke MV. Facile Green Synthesis of BCN Nanosheets as High-Performance Electrode Material for Electrochemical Energy Storage. Chemistry–A European Journal. 2016;22:7134-40.

[111] Xue Y, Yu D, Dai L, Wang R, Li D, Roy A, Lu F, Chen H, Liu Y, Qu J. Three-dimensional B, N-doped graphene foam as a metal-free catalyst for oxygen reduction reaction. Physical Chemistry Chemical Physics. 2013;15:12220-6.

[112] Singh NK, Pramoda K, Gopalakrishnan K, Rao C. Synthesis, characterization, surface properties and energy device characterstics of 2D borocarbonitrides,(BN) x C 1− x, covalently cross-linked with sheets of other 2D materials. RSC advances. 2018;8:17237-53.

[113] Lei W, Qin S, Liu D, Portehault D, Liu Z, Chen Y. Large scale boron carbon nitride nanosheets with enhanced lithium storage capabilities. Chemical communications. 2013;49:352-4.

[114] Tabassum H, Zou R, Mahmood A, Liang Z, Wang Q, Zhang H, Gao S, Qu C, Guo W, Guo S. A universal strategy for hollow metal oxide nanoparticles encapsulated into B/N Co-doped graphitic nanotubes as high-performance lithium-ion battery anodes. Advanced Materials. 2018;30:1705441.

[115] Nair SV, Baranwal G, Chatterjee M, Sachu A, Vasudevan AK, Bose C, Banerji A, Biswas R. Antimicrobial activity of plumbagin, a naturally occurring naphthoquinone from Plumbago rosea, against Staphylococcus aureus and Candida albicans. International Journal of Medical Microbiology. 2016;306:237-48.

[116] Slobbe L, El Barzouhi A, Boersma E, Rijnders BJ. Comparison of the roll plate method to the sonication method to diagnose catheter colonization and bacteremia in patients with long-

term tunnelled catheters: a randomized prospective study. Journal of clinical microbiology. 2009;47:885-8.

[117] Liu X, Chen X, Singh DJ, Stern RA, Wu J, Petitgirard S, Bina CR, Jacobsen SD. Boron–oxygen complex yields n-type surface layer in semiconducting diamond. Proceedings of the National Academy of Sciences. 2019;116:7703-11.

[118] Laidani N, Anderle M, Canteri R, Elia L, Luches A, Martino M, Micheli V, Speranza G. Structural and compositional study of B–C–N films produced by laser ablation of B4C targets in N2 atmosphere. Applied surface science. 2000;157:135-44.

[119] Ago H, Kugler T, Cacialli F, Salaneck WR, Shaffer MS, Windle AH, Friend RH. Work functions and surface functional groups of multiwall carbon nanotubes. The Journal of Physical Chemistry B. 1999;103:8116-21.

[120] Chowdhury FA, Hossain MA, Uchida K, Tamura T, Sugawa K, Mochida T, Otsuki J, Mohiuddin T, Boby MA, Alam MS. Graphene oxide/carbon nanoparticle thin film based IR detector: Surface properties and device characterization. AIP Advances. 2015;5:107228.

[121] Matsoso BJ, Ranganathan K, Mutuma BK, Lerotholi T, Jones G, Coville NJ. Synthesis and characterization of boron carbon oxynitride films with tunable composition using methane, boric acid and ammonia. New Journal of Chemistry. 2017;41:9497-504.

[122] Castillo H, Restrepo-Parra E, Vélez J, De la Cruz W. Substrate temperature influence on boron carbide coatings grown by the PLD technique. Surface and Coatings Technology. 2011;205:3607-12.

[123] Nehate SD, Saikumar AK, Sundaram KB. Influence of Substrate Temperature on Electrical and Optical Properties of Hydrogenated Boron Carbide Thin Films Deposited by RF Sputtering. Coatings. 2021;11:196.

[124] Frenklach M, Spear KE. Growth mechanism of vapor-deposited diamond. Journal of Materials Research. 1988;3:133-40.

[125] Morimitsu LA, Ospina RO, Carmona JG, Parra ER, Arango PA. Deposition and computational analysis of WC thin films grown by PAPVD. Revista Mexicana de Física. 2013;59:106-11.

[126] Richter F, Herrmann M, Molnar F, Chudoba T, Schwarzer N, Keunecke M, Bewilogua K, Zhang X, Boyen H-G, Ziemann P. Substrate influence in Young's modulus determination of thin films by indentation methods: Cubic boron nitride as an example. Surface and Coatings Technology. 2006;201:3577-87.

[127] Liu Y, Zhang L, Cheng L, Yang W, Xu Y. Effect of deposition temperature on boron-doped carbon coatings deposited from a BCl3–C3H6–H2 mixture using low pressure chemical vapor deposition. Applied surface science. 2009;255:8761-8.

[128] Shamiryan D, Abell T, Iacopi F, Maex K. Low-k dielectric materials. Materials today. 2004;7:34-9.

[129] Chiang C-C, Wu Z-C, Wu W-H, Chen M-C, Ko C-C, Chen H-P, Jang S-M, Yu C-H, Liang M-S. Physical and barrier properties of plasma enhanced chemical vapor deposition α-SiC: N: H films. Japanese journal of applied physics. 2003;42:4489.

[130] Alimov VK, Bogomolov D, Churaeva M, Gorodetsky A, Kanashenko S, Kanaev A, Rybakov SY, Sharapov V, Zakharov A, Zalavutdinov RK. Characterization of aB/C: H films deposited from different boron containing precursors. Journal of nuclear materials. 1992;196:670-5.

[131] Lee S, Mazurowski J, Ramseyer G, Dowben PA. Characterization of boron carbide thin films fabricated by plasma enhanced chemical vapor deposition from boranes. Journal of applied physics. 1992;72:4925-33.

[132] Balakrishnarajan MM, Pancharatna PD, Hoffmann R. Structure and bonding in boron carbide: The invincibility of imperfections. New Journal of Chemistry. 2007;31:473-85.

[133] Wood C, Emin D. Conduction mechanism in boron carbide. Physical Review B. 1984;29:4582.

[134] Tong GB, Aspanut Z, Muhamad MR, Rahman SA. Optical properties and crystallinity of hydrogenated nanocrystalline silicon (nc-Si: H) thin films deposited by rf-PECVD. Vacuum. 2012;86:1195-202.

[135] Basa D, Abbate G, Ambrosone G, Coscia U, Marino A. Spectroscopic ellipsometry study of hydrogenated amorphous silicon carbon alloy films deposited by plasma enhanced chemical vapor deposition. Journal of Applied Physics. 2010;107:023502.

[136] Casiraghi C, Ferrari A, Robertson J. Raman spectroscopy of hydrogenated amorphous carbons. Physical Review B. 2005;72:085401.

[137] Yang F, Zhao M, Zheng B, Xiao D, Wu L, Guo Y. Influence of pH on the fluorescence properties of graphene quantum dots using ozonation pre-oxide hydrothermal synthesis. Journal of Materials Chemistry. 2012;22:25471-9.

[138] Hasegawa T, Yamamoto K, Kakudate Y. Influence of raw gases on B–C–N films prepared by electron beam excited plasma CVD. Diamond and related materials. 2003;12:1045-8.

[139] Pei Q, Zhang Y, Shenoy V. A molecular dynamics study of the mechanical properties of hydrogen functionalized graphene. Carbon. 2010;48:898-904.

[140] Dethan JF, Swamy V. Tensile properties of hydrogenated hybrid graphene–hexagonal boron nitride nanosheets: a reactive force field study. Molecular Simulation. 2020;46:1220-9.

[141] Wu Z, Li S, Xu Z, Wang Q, Zhou F. Tribological properties of boron carbonitride coatings sliding against different wood (acerbic, beech, and lauan) balls. Advanced Composites Letters. 2019;28:0963693519875737.

[142] Ogi T, Kaihatsu Y, Iskandar F, Wang WN, Okuyama K. Facile synthesis of new full-color-emitting BCNO phosphors with high quantum efficiency. Advanced Materials. 2008;20:3235-8.

[143] Zhang X, Yan S, Cheng Y, Gao K, Lu Z, Meng F, Lin J, Xu X, Zhao J, Tang C. Spectral properties of BCNO phosphor with wide range of excitation and emission. Materials Letters. 2013;102:102-5.

[144] Moses K, Shirodkar SN, Waghmare UV, Rao C. Composition-dependent photoluminescence and electronic structure of 2-dimensional borocarbonitrides, BC XN (x= 1, 5). Materials Research Express. 2014;1:025603.

[145] Marchon B, Gui J, Grannen K, Rauch GC, Ager JW, Silva S, Robertson J. Photoluminescence and Raman spectroscopy in hydrogenated carbon films. IEEE transactions on magnetics. 1997;33:3148-50.

[146] Dai J, Ogbeide O, Macadam N, Sun Q, Yu W, Li Y, Su B-L, Hasan T, Huang X, Huang W. Printed gas sensors. Chemical Society Reviews. 2020;49:1756-89.

[147] Watanabe M, Sakai M, Shibata H, Satou C, Satou S, Shibayama T, Tampo H, Yamada A, Matsubara K, Sakurai K. Negative thermal quenching of photoluminescence in ZnO. Physica B: Condensed Matter. 2006;376:711-4.

[148] Nehate SD, Saikumar AK, Fincan M, Santana A, Volinsky AA, Campiglia A, Sundaram KB. Nanoindentation and Photoluminescence Studies of Hydrogenated Boron Carbon Nitride Thin Films. ECS Journal of Solid State Science and Technology. 2021;10:057004.

[149] Shibata H. Negative thermal quenching curves in photoluminescence of solids. Japanese journal of applied physics. 1998;37:550.

[150] Dey T, Mukherjee S, Ghorai A, Das S, Ray SK. Surface state selective tunable emission of graphene quantum dots exhibiting novel thermal quenching characteristics. Carbon. 2018;140:394-403.

[151] Onnink AJ, Apaydin RO, Aarnink AA, de Jong MP, Gravesteijn DJ, Kovalgin AY. Study of the phase nature of boron-and nitrogen-containing films by optical and photoelectron spectroscopy. Journal of Vacuum Science & Technology B, Nanotechnology and Microelectronics: Materials, Processing, Measurement, and Phenomena. 2020;38:044009.

[152] Jacobsohn L, Schulze R, Da Costa MM, Nastasi M. X-ray photoelectron spectroscopy investigation of boron carbide films deposited by sputtering. Surface Science. 2004;572:418-24.

[153] Hashim DP, Narayanan NT, Romo-Herrera JM, Cullen DA, Hahm MG, Lezzi P, Suttle JR, Kelkhoff D, Munoz-Sandoval E, Ganguli S. Covalently bonded three-dimensional carbon nanotube solids via boron induced nanojunctions. Scientific reports. 2012;2:1-8.

[154] Guimon C, Gonbeau D, Pfister-Guillouzo G, Dugne O, Guette A, Naslain R, Lahaye M. XPS study of BN thin films deposited by CVD on SiC plane substrates. Surface and Interface Analysis. 1990;16:440-5.

[155] Mannan MA, Nagano M, Shigezumi K, Kida T, Hirao N, Baba Y. Characterization of boron carbonitride (BCN) thin films deposited by radiofrequency and microwave plasma enhanced chemical vapor deposition. Am J Appl Sci. 2007;5:736-41.

[156] Prakash A, Sundaram KB. Deposition and XPS studies of dual sputtered BCN thin films. Diamond and Related Materials. 2016;64:80-8.

[157] Smith M, Scudiero L, Espinal J, McEwen J-S, Garcia-Perez M. Improving the deconvolution and interpretation of XPS spectra from chars by ab initio calculations. Carbon. 2016;110:155-71.

[158] Wan S, Yu Y, Pu J, Lu Z. Facile fabrication of boron nitride nanosheets–amorphous carbon hybrid film for optoelectronic applications. Rsc Advances. 2015;5:19236-40.

[159] Yang Q, Wang C, Zhang S, Zhang D, Shen Q, Zhang L. Effect of nitrogen pressure on structure and optical properties of pulsed laser deposited BCN thin films. Surface and Coatings Technology. 2010;204:1863-7.

[160] Hellgren N, Guo J, Luo Y, Såthe C, Agui A, Kashtanov S, Nordgren J, Ågren H, Sundgren J-E. Electronic structure of carbon nitride thin films studied by X-ray spectroscopy techniques. Thin Solid Films. 2005;471:19-34.

[161] Trehan R, Lifshitz Y, Rabalais J. Auger and x-ray electron spectroscopy studies of h BN, c BN, and N+ 2 ion irradiation of boron and boron nitride. Journal of Vacuum Science & Technology A: Vacuum, Surfaces, and Films. 1990;8:4026-32.

[162] Yu J, Wang E, Ahn J, Yoon S, Zhang Q, Cui J, Yu M. Turbostratic boron carbonitride films produced by bias-assisted hot filament chemical vapor deposition. Journal of Applied Physics. 2000;87:4022-5.

[163] Xu Y, Li D, Liu M, Niu F, Liu J, Wang E. Enhanced-quantum yield sulfur/nitrogen co-doped fluorescent carbon nanodots produced from biomass Enteromorpha prolifera: synthesis, posttreatment, applications and mechanism study. Scientific reports. 2017;7:1-12.

[164] Nordell BJ, Nguyen TD, Caruso AN, Purohit SS, Oyler NA, Lanford WA, Gidley DW, Gaskins JT, Hopkins PE, Henry P. Carbon-Enriched Amorphous Hydrogenated Boron Carbide Films for Very-Low-k Interlayer Dielectrics. Advanced Electronic Materials. 2017;3:1700116.

[165] Aoki H, Masuzumi T, Hara M, Watanabe D, Kimura C, Sugino T. Effect of the radio-frequency power on the dielectric properties of hydrogen-containing boron carbon nitride films deposited by plasma-assisted chemical vapor deposition using tris (dimethylamino) boron gas. Thin solid films. 2010;518:2102-4.

[166] Aoki H, Masuzumi T, Hara M, Lu Z, Watanebe D, Kimura C, Sugino T. Influence of the methyl group on the dielectric constant of boron carbon nitride films containing it. Diamond and related materials. 2010;19:1437-40.

[167] Bath A, Van der Put P, Schoonman J, Lepley B. Study of boron nitride gate insulators grown by low temperature plasma enhanced chemical vapor deposition on InP. Applied Surface Science. 1989;39:135-40.

[168] Tehrani FS, Goh BT, Muhamad MR, Rahman SA. Pressure dependent structural and optical properties of silicon carbide thin films deposited by hot wire chemical vapor deposition from pure silane and methane gases. Journal of Materials Science: Materials in Electronics. 2013;24:1361-8.

[169] Durmus NG, Erik NT, Kim MK, Thomas JW. Fructose enhanced reduction of bacterial growth on nanorough surfaces. MRS Online Proceedings Library. 2012;1498:73-8.

[170] Feng G, Cheng Y, Wang S-Y, Borca-Tasciuc DA, Worobo RW, Moraru CI. Bacterial attachment and biofilm formation on surfaces are reduced by small-diameter nanoscale pores: how small is small enough? npj Biofilms and Microbiomes. 2015;1:1-9.

[171] Sukhorukova I, Sheveyko A, Kiryukhantsev-Korneev PV, Zhitnyak I, Gloushankova N, Denisenko E, Filippovich SY, Ignatov S, Shtansky D. Toward bioactive yet antibacterial surfaces. Colloids and Surfaces B: Biointerfaces. 2015;135:158-65.

[172] Rajakumar G, Rahuman AA, Roopan SM, Khanna VG, Elango G, Kamaraj C, Zahir AA, Velayutham K. Fungus-mediated biosynthesis and characterization of TiO2 nanoparticles and their activity against pathogenic bacteria. Spectrochimica Acta Part A: Molecular and Biomolecular Spectroscopy. 2012;91:23-9.

[173] Wang L, Hu C, Shao L. The antimicrobial activity of nanoparticles: present situation and prospects for the future. International journal of nanomedicine. 2017;12:1227.

[174] Wu Y, Zitelli JP, TenHuisen KS, Yu X, Libera MR. Differential response of Staphylococci and osteoblasts to varying titanium surface roughness. Biomaterials. 2011;32:951-60.

[175] Hsu LC, Fang J, Borca-Tasciuc DA, Worobo RW, Moraru CI. Effect of micro-and nanoscale topography on the adhesion of bacterial cells to solid surfaces. Applied and environmental microbiology. 2013;79:2703-12.

[176] Friedlander RS, Vlamakis H, Kim P, Khan M, Kolter R, Aizenberg J. Bacterial flagella explore microscale hummocks and hollows to increase adhesion. Proceedings of the National Academy of Sciences. 2013;110:5624-9.